Remote sensing of mountain snow surface temperatures at high temporal resolution using geostationary satellites

Steven James Pestana

A dissertation

submitted in partial fulfillment of the

requirements for the degree of

Doctor of Philosophy

University of Washington

2023

Reading Committee:

Jessica D. Lundquist, Chair

C. Chris Chickadel

Bart Nijssen

David Shean

Program Authorized to Offer Degree:

Civil and Environmental Engineering

University of Washington

Abstract

Remote sensing of mountain snow surface temperatures at high temporal resolution using geostationary satellites

Steven James Pestana

Chair of the Supervisory Committee:
Jessica D. Lundquist
Civil and Environmental Engineering

Remote sensing by geostationary satellites, such as by the NOAA GOES-R series with the Advanced Baseline Imager (ABI), can provide imagery of surface temperatures at high temporal resolutions due to their fixed views of Earth's surface. In mountain headwaters that receive seasonal snow, spatially distributed observations of snow surface temperatures are needed to better constrain estimates of the surface energy balance, predictions of snowmelt, and available water resources. These observations are needed particularly at spatial and temporal resolutions relevant to land surface and hydrology models, a capability that the 5-minute, near-real-time GOES-R observations may be able to fill. The utility of these observations, however, may be limited by their relatively coarse (2+ km) spatial resolution, and the off-nadir view angles of geostationary satellites.

In this dissertation, we found that the off-nadir views, surface roughness at different spatial scales, and changing direction of solar illumination over the course of a day, all impact the surface temperatures observed by GOES-R ABI. In Chapter 2, we demonstrated that off-nadir geostationary satellite imagery must be corrected for the parallax effect in mountainous areas. Even with this correction, the surface temperatures observed by GOES-16 were biased towards those of warmer sunlit south-facing mountain slopes that were facing the satellite. Chapter 3 provides information about the software developed to correct for the parallax effect in GOES-R ABI imagery. In Chapter 4, as part of the NASA SnowEx 2020 field campaign, we found that at the scale of forest stands and individual trees across a snow-covered area, the surface temperatures observed by GOES-R ABI were biased towards that of the warmer tree temperatures in comparison with coincident nadir-looking imagery. This warm bias was greatest at times of day when the sun-satellite phase angle was at its minimum, suggesting a diurnal thermal infrared shadow hiding effect where cold shadows are briefly hidden from view by the warmer trees. Chapter 5 extended this analysis of shadow hiding to the midwave infrared, which in the daytime has both an emitted and reflected solar component. The shadow hiding effect was also found in the midwave infrared imagery, however not just for forested areas but also for snow surfaces with centimeter-scale wind-formed roughness features. This demonstrated that for applications of midwave infrared observations, rather than only treating the surface reflectance of different materials (e.g., snow and vegetation) independently, they must also be considered together as an anisotropic reflector and emitter of midwave infrared radiation.

Acknowledgements

I would like to acknowledge and thank my advisory committee members: Jessica Lundquist, Chris Chickadel, Bart Nijssen, and David Shean; and graduate school faculty representative: Steve Warren. They provided their expertise, guidance, and feedback on this work, from the initial research proposed, to the evolving pathways of investigation and analysis. I especially thank my advisor Jessica Lundquist for her invaluable mentorship and for providing opportunities for professional development in research, teaching, collaboration, leadership, and communication.

Financial support for this research came from NASA FINESST grant 80NSSC20K1610, and NASA grant NNX17AL59G. Thank you to the SINTER, CUAHSI, and SnowEx communities, for providing learning opportunities through community meetings, workshops, and the snow school program. Special thanks to SnowEx science leads Carrie Vuyovich and H.P. Marshall, for their leadership, and efforts to foster supportive environments for students and early-career scientists. Thank you to the University of Washington eScience Institute, Anthony Arendt, Christina Bandaragoda, Nicoleta Cristea, and Scott Henderson, for providing learning opportunities through hackweeks, workshops, and lending their expertise in solving computing problems. I would like to thank our collaborators, Chris Chickadel, Ned Bair, and Jeff Dozier, who enabled unique data collection and whose expert input greatly improved this research. Thank you to Val Chang for helping me teach an online class at the beginning of the pandemic, and to Paulo Alexandre Mello for collaborating on building software tools that greatly helped this research.

I am grateful for all the past and present members of the Mountain Hydrology Research group for their support, including Joe Ammatelli, Hannah Besso, Jori Carter, Nicoleta Cristea,

Ryan Currier, Hannah Hampson, Danny Hogan, Cassie Lumbrazo, Victoria Ly, Calista Moore, Ross Mower, Max Mozer, Justin Pflug, Dylan Reynolds, Eli Schwat, Kehan Yang, and Annie Zaccarin. I am also grateful for my fellow cohort of mountain remote sensing graduate students, including Shashank Bhushan, Michelle Hu, and Friedrich Knuth, and all my office-mates in the "Fishbowl" and "Tree House" for their camaraderie. Thank you to F.D. Thorton & Penelope for their useful contributions and lively discussions. Finally, I want to thank my family and friends, especially my partner Kristina, for their encouragement and support throughout my time in graduate school.

Published Material

At the time of writing, Chapter 2 of this dissertation has been published in a peer reviewed journal. I would like to acknowledge Elsevier, publisher of *Remote Sensing of Environment*, for granting permission to reproduce the article in this dissertation.

The citation for the published article is:

Pestana, S., & Lundquist, J. D. (2022). Evaluating GOES-16 ABI surface brightness temperature observation biases over the central Sierra Nevada of California. Remote Sensing of Environment, 281, 113221. https://doi.org/10.1016/j.rse.2022.113221

Table of Contents

List of Figures

List of Tables

Chapter 1. Introduction

Water provided by seasonal mountain snowmelt supports downstream ecosystems and 1.9 billion people globally (Immerzeel et al., 2020). Accurate observations of the energy fluxes at the snow surface are needed to inform, evaluate, or correct our hydrologic models, though observations in mountain headwaters are sparse or non-existent (Raleigh et al., 2016). The ability to predict changes in these water resources is vitally important, especially in light of global climate change, which is altering the patterns that humans have relied upon and for which our water resources infrastructure is built around (Barnett et al., 2005; Siirila-Woodburn et al., 2021). Observations of the snow surface energy balance, namely the longwave radiative energy balance, are especially important for evaluating model performance or for model assimilation (Dozier & Marks, 1992; Hinkelman et al., 2012; Lapo et al., 2015). The snow surface is the lower boundary of land-atmosphere energy exchanges (Raleigh et al., 2013), and its temperature can reveal changes in snow grain metamorphism, emissivity (Warren, 1982, 2019), albedo (Flanner & Zender, 2006), and is itself modulated by the net radiative, turbulent, and conductive heat fluxes.

While thermal infrared satellite imagery can provide distributed surface temperature observations, these are limited by the tradeoffs between spatial and temporal resolution. Thermal infrared satellite images at spatial resolutions ≤ 100 m are only acquired as frequently as every 3-16 days, whereas coarser spatial resolution 750 – 1000 m observations are available approximately 4 times daily. These observations do not capture the sub-daily variability in surface temperatures, do not necessarily measure the full diurnal temperature range, nor the timing of daily minimum and maximum temperatures. Fortunately, geostationary satellites can provide much higher temporal resolution observations with their fixed view of Earth's surface, though at the loss of spatial resolution. NOAA's GOES-R series, with the Advanced Baseline

Imager (ABI), offers improvements in spatial (500 – 2000 m), spectral (16 bands visible through thermal infrared), and temporal resolution over prior geostationary satellites (Schmit et al., 2017). The two GOES-R satellites used in this work, GOES-16 (in the GOES-East position with views of the Atlantic Ocean) and GOES-17 (in the GOES-West position over the Pacific Ocean) provide observations covering much of the western hemisphere, capturing thermal infrared imagery every 5 minutes, with a nominal spatial resolution of 2 km.

In this dissertation, we have conducted an evaluation of GOES-R thermal infrared imagery as a source of distributed surface temperature observations for mountain snow, and quantified our ability to measure snow surface temperatures with GOES-R in forested mountain terrain. This work was undertaken to inform how GOES-R observations could be used for mountain snow hydrology applications or for mountain air temperature bias corrections, the strengths and weaknesses of using geostationary satellite imagery, and to compare these observations against other sources of thermal infrared remote sensing. We focused on two study regions in the western United States where extensive ground-based and other remote sensing observations provided us with rich datasets for comparison and validation. For Chapter 2 we focused on the central Sierra Nevada in part of the upper watershed of the San Joaquin river and its tributaries the Tuolumne and Merced rivers. Chapter 3 describes a Python software package we developed to work with GOES-R imagery. Chapters 4 and 5 focused on Grand Mesa in western Colorado, in part of the upper watershed of the Colorado River and its tributary, the Gunnison river.

In Chapter 2, we compared GOES-16 thermal infrared images against coincident higher spatial resolution MODIS and ASTER images over a study region in the Sierra Nevada of California. We demonstrated the necessity of correcting for the parallax effect of mountain terrain (orthorectification) in GOES-R imagery for mountain observation applications and

developed a software package to perform these corrections (Pestana et al., 2022). The differences between surface brightness temperatures as seen by GOES-16, MODIS, and ASTER were investigated to understand how the presence of forest cover, rugged mountain terrain, the differential heating of hillslopes by sunlight, and different view angles influenced the temperatures observed (Pestana & Lundquist, 2022). Chapter 3 describes the Python software package developed to orthorectify GOES-R image products.

In Chapter 4 we collected surface temperature observations at multiple spatial and temporal scales – from ground-based, to airborne, and satellite remote sensing – as part of the SnowEx 2020 field campaign at Grand Mesa in western Colorado. We investigated how remote sensing of snow surface temperature from different platforms compared with GOES-16 and -17, and how biases in the thermal infrared (TIR) observations from these geostationary satellites were influenced by varying forest cover across the study area and surface heating by incoming solar radiation at different times of day.

In Chapter 5 we investigated how the reflected component of midwave infrared (MWIR), as observed by GOES-R ABI, is impacted by the sun-satellite phase angle and forest cover over the flat expanse of Grand Mesa. Observations in the MWIR are needed for infrared spectral unmixing applications (Dozier, 1981), however, these methods must incorporate estimates of how incoming solar MWIR is reflected by the land surfaces of interest. We compared prior MWIR reflectance estimates that treated snow and vegetation reflectance independently (Lundquist et al., 2018) to observations of MWIR over a range of solar illumination angles and forest cover fractions.

Chapter 2. Evaluating GOES-16 ABI surface brightness temperature observation biases over the central Sierra Nevada of California

Steven Pestana [1] and Jessica D. Lundquist [1]

[1] Civil and Environmental Engineering, University of Washington, Seattle, WA, USA

Note: This chapter has been published in its current form as an article in *Remote Sensing of Environment* (Pestana & Lundquist, 2022); the only differences are in section, figure, and table numbering. It is used here by permission of Elsevier.

2.1 Abstract

Thermal infrared imagery from NOAA's Geostationary Operational Environmental Satellites (GOES) R-series presents an opportunity to observe mountain surface temperatures at high temporal resolution. These observations are needed to better understand the transient surface energy balance, influenced by near-surface air temperatures and water fluxes ranging from evapotranspiration to snowmelt. From geostationary orbit, the GOES Advanced Baseline Imager (ABI) instrument views the Earth from a fixed longitude above the equator. ABI images therefore have increasingly off-nadir view angles and increasingly larger pixel dimensions the further a point on the Earth's surface is from the sub-satellite point. In thermal infrared imagery from ABI, these 2+ km pixels blur together the different surface temperatures of heterogeneous mountain landscapes. We compared GOES-16 ABI band 14 (11.2 μm) brightness temperatures to 90 m spatial resolution ASTER band 14 (11.3 μm) and 1 km spatial resolution MODIS band 31 (11.03 μm) brightness temperatures and investigated how differences change over space and time for a study region in the central Sierra Nevada of California for the 2017-2020 snow seasons. We demonstrated the necessity of orthorectifying ABI imagery of mountain terrain to correct for the parallax effect in off-nadir imagery. This reduced the mean difference between ABI and ASTER ~11 μm brightness temperatures from 1.6 °C to 1.0 °C and increased the r-squared value between ABI and ASTER thermal infrared brightness temperatures from 0.43 to 0.93. The ABI brightness temperatures were found to more closely match those of forest canopy temperatures than snow surface (with RMS differences of 1.2 °C and 3.0 °C respectively), and those of sunlit slopes as opposed to slopes facing away from the sun (with RMS differences of 1.6 °C and 3.4 °C respectively), in coincident ASTER imagery. This work demonstrates the use

of GOES ABI, and associated challenges, for observing surface temperatures of forested mountain environments with seasonal snow.

2.2 Introduction

Satellite remote sensing in the thermal infrared can provide spatially contiguous maps of surface temperatures across wide areas (Jin & Dickinson, 2010), but only remote sensing from geostationary satellites can provide repeat observations at high temporal resolutions (e.g. 1-30 minutes). NOAA's Geostationary Operational Environmental Satellites (GOES) R-series (GOES-R, -S, and -T) are each outfitted with the Advanced Baseline Imager (ABI), which can make repeat observations every 5 minutes.

High temporal resolution remote sensing observations are needed especially for mountains where in situ observations are scarce (Raleigh et al., 2013). In this complex terrain, important transient events such as changes in air temperature lapse rates (Lundquist & Cayan, 2007; Minder et al., 2010; Mizukami et al., 2014; Pepin et al., 2019), the melting and re-freezing of snow (Essery et al., 2013; Niu et al., 2011), the diurnal cycles of near-surface air temperature (Shamir & Georgakakos, 2014; Williamson et al., 2017), and early wildfire hotspot detection (Koltunov et al., 2016) can only be resolved by remote sensing at high temporal resolutions. High temporal resolution thermal infrared observations could help detect, and through assimilation, correct, biases in the diurnal temperature ranges (DTR) of land surface models, which especially struggle in mountain regions (Lapo et al., 2015; Massey et al., 2016; Pavelsky et al., 2011; Pepin et al., 2016; Xiang et al., 2017; Zink et al., 2018).

However, over the heterogeneous land surface of mountains, consisting of spatially varying forest, soil, rock, ice, and snow, the use of thermal infrared imagery from geostationary satellites for observing surface temperatures at fine spatial scales is complicated by its coarse spatial

resolution (e.g. 2+ km GOES ABI) and the large range in view angles (from 0° at nadir to 70°+ off-nadir). Comparisons of the two ABI imagers on GOES-16 and -17 over the continental United States show land surface temperature differences of 5 °C or greater over the heterogenous land surfaces of mountain terrain and less than 5 °C over more homogenous and flat terrain (Chen et al., 2021). The magnitude of and explanations for differences between GOES-16 ABI and nadir-looking satellite imagers over snow and forest-covered mountain terrain have not yet been investigated.

Whereas low Earth orbiting satellites can provide nadir-looking thermal infrared imagery at kilometer-scales (e.g., 1000 m MODIS IR, 750 m VIIRS IR) to hillslope scales (e.g., 90 m ASTER IR, 100 m Landsat TIRS, 70 m ECOSTRESS), the time between repeat observations range from several hours (MODIS and VIIRS), to days (ECOSTRESS), or weeks (ASTER and Landsat TIRS). Even the approximately twice daily MODIS and VIIRS observations of the mid-latitudes do not capture the full diurnal temperature range with their fixed overpass times, nor the high temporal resolution details that could show rapid changes in surface temperatures such as warming from morning sunlight or early signs of wildfire.

GOES ABI images have spatially variable view angles that are increasingly off-nadir further from the sub-satellite point that lies on the equator at the satellite's orbital longitude (Schmit et al., 2017). In addition to coarsening the spatial resolution, these off-nadir view angles give mountaintops an apparent horizontal offset, or parallax, in standard ABI image products (Figure 2.1a). This parallax is a function of the ABI view angle and the land surface elevation. Orthorectification is the process of correcting for the parallax effect of terrain to create an image where the land surface is seen as if from nadir. Previous studies have orthorectified geostationary imagery by matching features to georeferenced Landsat images (Bian et al., 2017) or using

DEMs at the same spatial resolution as geostationary satellite visible band imagery (500m – 1km) with a line-of-sight method (Takeuchi, 2016; Takeuchi & Yasuoka, 2007; Wang et al., 2020). These prior approaches have not taken into account the finer subpixel scale terrain variations, which are especially important for mountain regions where elevation varies significantly within each large pixel.

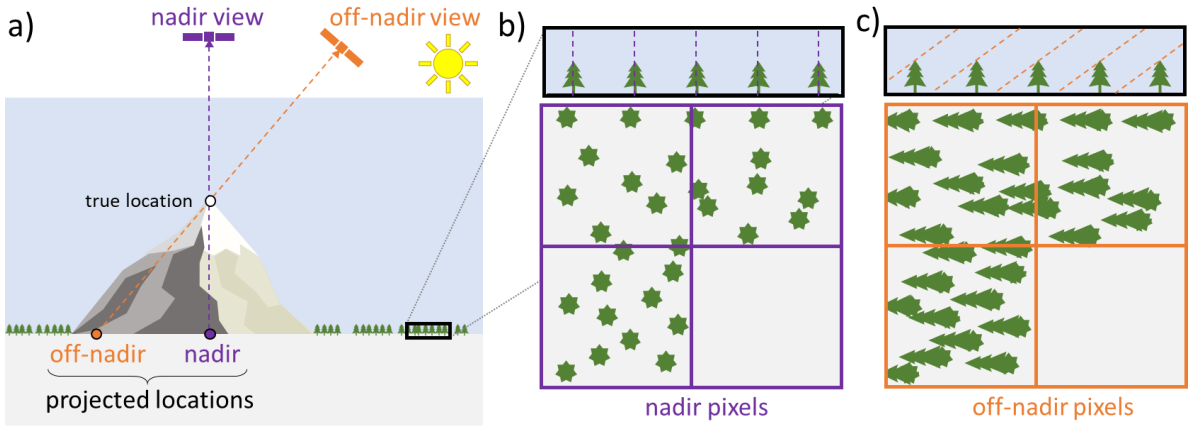

Figure 2.1. Some of the anticipated challenges of using off-nadir satellite observations over forested mountain terrain: the parallax effect causes (a) geolocation misalignment, and apparent lengthening or shortening of shaded or sunlit mountain slopes; at smaller spatial scales the visible gap fraction of a forest (b) in nadir images, is greater than (c) in off-nadir images due to parallax of individual trees. (Illustrated here with a plane-parallel atmosphere for simplicity).

In addition to the parallax effect causing geolocation offsets in GOES ABI images, these off-nadir view angles also mean that ABI sees more of the mountain slopes that face towards the satellite than the mountain slopes facing in other directions. In the extreme case, steep slopes facing away from the satellite could be completely occluded by terrain, meaning that those land surfaces are never seen by ABI. Off-nadir images also view the sides of trees rather than just the treetops as in nadir imagery (Figure 2.1b,c), blocking views into small forest gaps and increasing the apparent fractional vegetated area (f_{veg}) (decreasing the visible gap fraction (VGF)) (H. Liu & Weng, 2008; Nolin, 2010; Xin et al., 2012). Therefore, the temperature recorded by an off-nadir

pixel containing snow and partial forest cover is expected to be biased more towards the temperature of the trees or the sides of trees that face the satellite (Henderson et al., 2003; Otterman et al., 1999; Pestana et al., 2019).

The emitted radiance from a surface depends on its kinetic temperature, emissivity, and varies by wavelength. Where surface temperatures or emissivities vary at fine scales smaller than the spatial resolution of thermal infrared imagery, such as for partially snow covered or forested areas (Williamson et al., 2017), the radiance recorded at each image detector is a mixture of those emitted subpixel radiances. The resulting radiance of a heterogenous pixel can be approximated as the mean of all subpixel radiances weighted by their fractional areas (such as f_{veg}) (Dozier, 1981; Gillespie et al., 1998; Y. Liu et al., 2006). This approximation assumes that each detector senses radiance from only the land surface exactly within its instantaneous field of view (IFOV), and that the detector's sensitivity to radiance is uniform across the entire IFOV. In reality, each detector senses radiance unevenly, described by a point spread (weighting) function, approximated by the IFOV (Cracknell, 1998). In the case of ABI imagery, this approximation is further complicated given that ABI products have been resampled to the ABI Fixed Grid from the raw detector samples. The raw detector samples for ABI IR bands have an IFOV of 38.1 by 34.3 μrad, smaller than the 56 μrad IFOV of the ABI Fixed Grid, but are not currently available as a data product (Kalluri et al., 2018). While this resampling of actual detector samples to pixels in the ABI Fixed Grid allows for precise image-to-image alignment, we expect that the radiance reported by each resampled 2+ km ABI Fixed Grid pixel might not be the true mean radiance of the land surface within its IFOV. To use GOES ABI for mountain land surface observations at high temporal resolution, we first need to understand how the radiances, and surface brightness temperatures, seen by ABI compare with the underlying heterogenous subpixel brightness

temperatures. In this paper, we investigate how surface brightness temperatures from GOES-16 ABI thermal infrared imagery are influenced by coarse spatial resolutions and off-nadir view angles for a study domain in the central Sierra Nevada of California containing complex terrain, snow, and forest cover (Figure 2.2). We use the difference between GOES-16 ABI and nadir-looking ASTER (Abrams, 2000; Y. Liu et al., 2006) thermal infrared brightness temperatures ($\Delta T_{ABI-AST}$) at ~11 μm as a metric to quantify how ABI brightness temperatures deviate from the subpixel mean approximation. We investigate where, when, and why $\Delta T_{ABI-AST}$ varied to specifically address the following questions:

1) How much can $\Delta T_{ABI-AST}$ be reduced by orthorectifying the off-nadir ABI imagery to correct for the parallax effect over mountain terrain?
2) How do topographic or land surface features influence $\Delta T_{ABI-AST}$ when considered in the context of (a) the coarse spatial resolution of GOES-16 ABI and (b) its off-nadir view angle?
3) How does the performance of GOES-16 ABI ($\Delta T_{ABI-AST}$) compare with that of nadir-looking MODIS ($\Delta T_{MOD-AST}$), which is on the same satellite as ASTER?

For the first question, we hypothesized that $\Delta T_{ABI-AST}$ can be reduced by correcting for the parallax effect, which causes geolocation offsets (Figure 2.1a). A subpixel orthorectification method described in Section 2.4.1 is tested to correct for this effect, with results presented in Section 2.5.1. For question two, we hypothesized that $\Delta T_{ABI-AST}$ will correlate with slope and aspect, with smaller magnitude differences for the slopes facing GOES-16. We also hypothesize that $\Delta T_{ABI-AST}$ will correlate with $f_{veg,}$ as the visible gap fraction is reduced in off-nadir views (Dozier et al., 2008; Henderson et al., 2003; H. Liu & Weng, 2008; Pestana et al., 2019) (Figure 2.1c). The correlation coefficients of $\Delta T_{ABI-AST}$ with f_{veg} and topographic indices are investigated

in Section 2.4.3, with results presented in Section 2.5.3. For the last question, we examined MODIS imagery in addition to ASTER and ABI as described in Section 2.4.2, with results presented in Section 2.5.2. We hypothesized that the nadir looking center of 1 km resolution MODIS image swaths will more closely match ASTER surface brightness temperatures across the mountain study region than ABI (Figure 2.1b,c).

2.3 Data: Study Sites and Satellites

2.3.1 Study area and time period

This study focused on a ~1000 km^2 region of the Sierra Nevada crest in California, running roughly southeast to northwest between latitudes 37.57 N and 37.97 N (Figure 2.2) from 1 March 2017 to 30 June 2020. Elevations in the area range from 1900 to 4000 m, with a mean of ~3000 m, and more than half of the area lies between 2700 and 3300 m. The mountain terrain has aspects generally facing south-southwest and north-northeast, with a mean slope of about 17°. The study region contains portions of the headwater basins for the Tuolumne, Merced, and San Joaquin rivers west of the crest, and the Mono Lake and Owens River basins east of the crest. The study area and time period were chosen to focus our analysis of GOES-16 ABI thermal infrared imagery on high elevations that receive seasonal snow so that the main land surfaces contributing to the temperature sensed by a mixed pixel are snow and conifer forests (Lundquist et al., 2018). Snow and conifer needles have similar high emissivities in the thermal infrared, 0.98-0.99 and 0.97-0.98, respectively, such that their thermal infrared brightness temperatures are close to their true kinetic surface temperatures (Howard & Stull, 2013; Warren, 2019). This high-elevation study area in California was also chosen because of the prevalence of clear skies, and therefore cloud-free imagery. At these high elevations and dry atmospheric conditions atmospheric absorption of thermal infrared radiation by water vapor is minimized (Lundquist et

al., 2018). The influences of the atmosphere and surface emissivities on our results are discussed further in Sections 2.6.1 and 2.6.2. The National Land Cover Database (NLCD) 30 m spatial resolution 2016 tree canopy cover (TCC) data product (USDA Forest Service, 2019) for the study area was used to derive a fractional vegetated area map used in later analysis.

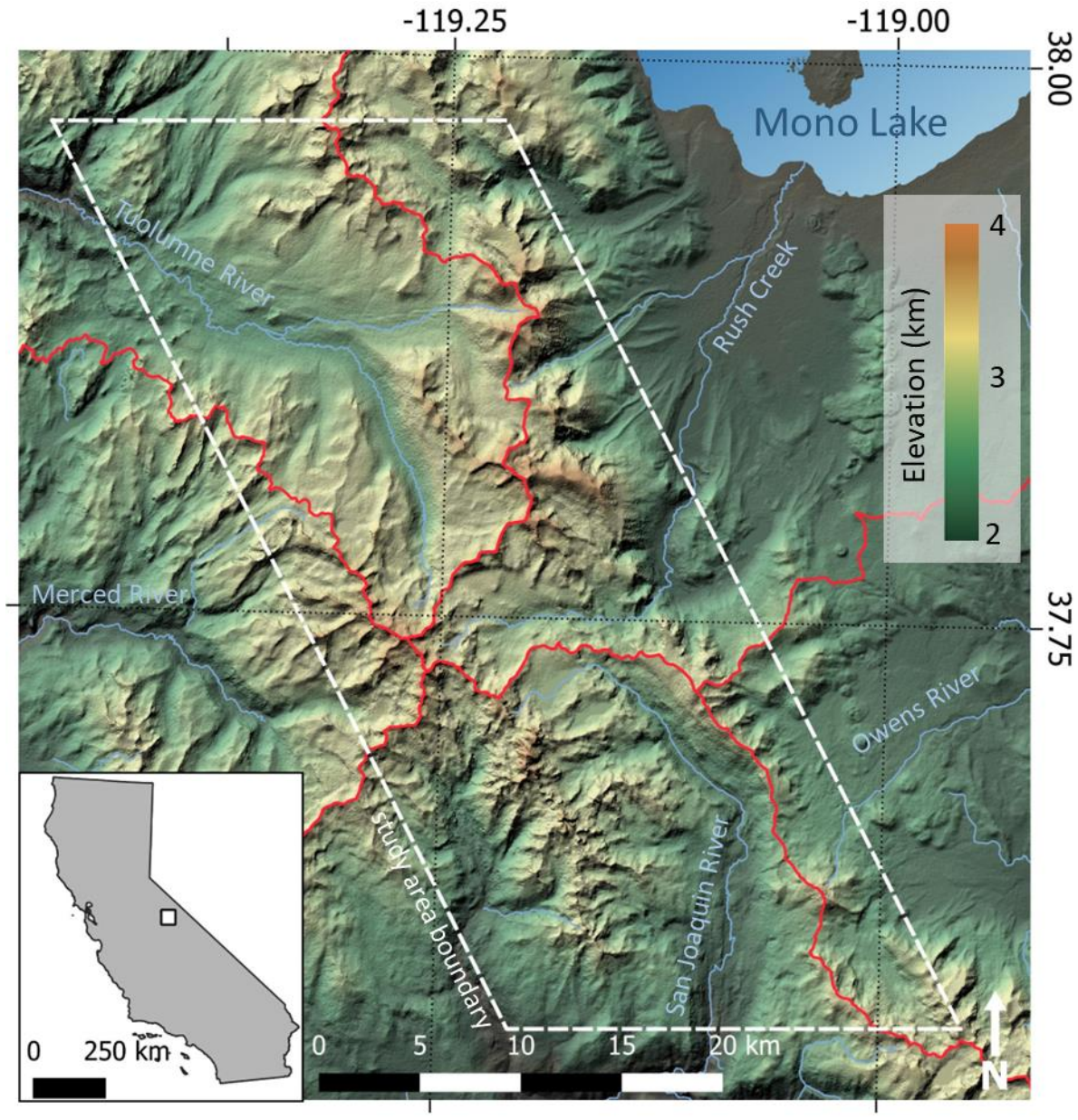

Figure 2.2. Shaded relief map of the study area (dashed outline) along the central Sierra Nevada crest, where mean elevation is 3000 m (elevation data from NASA SRTM, 2013). Watershed boundaries (USGS, 2016) are delineated for the Tuolumne, Merced, San Joaquin rivers on the west, and the Mono and Owens valley basins on the east (red lines).

Table 2.1. Remote sensing and raster datasets used in analysis

Dataset	Product	Band Number	Band center wavelength	Resolution	
				Spatial	Temporal
GOES-16 ABI	ABI L1b RadC	14	11.20 μm	2+ km	5 min
Terra MODIS	MOD021KM	31	11.03 μm	1 km	12 hours
Terra ASTER	AST L1T	14	11.30 μm	90 m	16 days
Fractional snow cover	MODSCAG	-	-	500 m	1 day
Tree canopy cover	NLCD TCC	-	-	30 m	-
Digital elevation model	SRTM GL3 DEM	-	-	90 m	-

2.3.2 GOES-16 Advanced Baseline Imager (ABI)

The NOAA GOES-16 ABI provides a nearly hemispherical view of Earth from geostationary orbit at the -75° longitude GOES-West orbital slot (Schmit et al., 2017). In the default operating mode, ABI images of the visible "Full Disk" or CONUS subset are taken at 10-minute and 5-minute intervals, respectively (Table 2.1). The thermal infrared ABI bands have a nominal (at sub-satellite point) spatial resolution of 2 km, though these increase in size as view angles increase from 0° at the sub-satellite point to >70° towards the visible limb of the Earth (NOAA-NASA, 2019; Yu et al., 2010). ABI image products come in the ABI Fixed Grid coordinate system, where the image dimensions and pixel instantaneous fields of view (IFOV) are represented in elevation (vertical) and scan (horizontal) angles in units of radians (Kalluri et al., 2018). The 2+ km infrared ABI pixels correspond to an IFOV of 56 μrad in the ABI Fixed Grid, having been resampled with a weighting kernel from the values sensed by the detector arrays. The thermal infrared detectors have true vertical and horizontal IFOVs of 38.1 and 34.3

μrad, respectively, and are swept horizontally over 44 μrad to create each sample (Kalluri et al., 2018).

The GOES-16 ABI Level 1b (top of atmosphere) Radiance CONUS product was used to compute brightness temperature in the 11.2 μm band (ABI channel 14) (GOES-R Calibration Working Group & GOES-R Program Office, 2017). We chose this product over the hourly Land Surface Temperature (LST) product (GOES-R. Calibration Working Group & GOES-R Program Office, 2018) for two main reasons. First, the ABI radiance product is available at a temporal resolution of 5 minutes, which allowed us to find an ABI radiance image taken within less than 5 minutes of each MODIS/ASTER image pair (Section 2.3.3). Second, the ABI LST product uses the ABI Cloud Mask product to remove cloudy pixels from the LST images, which, like other multispectral cloud detection methods, often mistook snow-covered mountains for clouds (D. K. Hall & Riggs, 2007; Stillinger et al., 2019; Williamson et al., 2013). All but four of the available ABI LST images within 30 minutes of each MODIS/ASTER observation contained erroneously masked snow pixels, and in five images nearly the entire study area is masked out.

ABI radiance imagery was retrieved from NOAA's GOES repository on Amazon Web Services (AWS) using the goespy Python library (Mello & Pestana, 2022), for observations of the study area coincident with ASTER from 1 March 2017 to 30 June 2020. ABI imagery from before December 2017 were from its "pre-operational" stage when GOES-16 was still at the -89.5° longitude orbital slot. While we did include two of these pre-operational images in our analysis, their unique view angles were taken into account in the orthorectification process and other view angle dependent analyses. The choice to use brightness temperatures instead of LST neglects atmospheric influences. Water vapor in the atmosphere will absorb thermal infrared radiance around 11 microns, such that the observed brightness temperature will be less than

kinetic surface temperature (McMillin, 1975; Yu et al., 2008). However, compared to other influences, this effect is small. The GOES-16 LST product's handling of atmospheric water vapor, emissivity, and its relationship to the brightness temperature data from our domain are discussed further in Sections 2.6.1 and 2.6.2.

2.3.3 Terra ASTER and MODIS

MODIS (Moderate Resolution Imaging Spectroradiometer) and ASTER (Advanced Spaceborne Thermal Emission and Reflection Radiometer) are both onboard the NASA Terra satellite, which passes over our Sierra Nevada study area every day at about 10:50 AM and 10:05 PM local time (UTC-08:00). The wider swath of MODIS allows it to make twice-daily repeat observations of the mid-latitudes at 1 km spatial resolution in the thermal infrared, while the narrow swath of ASTER limits its observations to a 16-day repeat cycle but at 90 m spatial resolution.

The ASTER band 14 (11.30 μm) Level 1T product used in this study provides terrain-corrected radiance values at 90 m spatial resolution, which were downloaded from NASA EarthData (Abrams, 2000; Meyer et al., 2015). These thermal infrared images were used to represent finer spatial scale variabilities across the study area. ASTER images from the snow season months, November to June, were manually inspected for cloud-cover, and 27 images spanning the study period were selected to include in the analysis. MODIS band 31 (11.03 μm) Level 1B Calibrated Radiance (MOD021KM) observations at 1 km spatial resolution that were coincident with the 27 ASTER images were also downloaded from NASA EarthData (MODIS MCST, 2018). Brightness temperatures at ~11 μm were used rather than LST products for both ASTER and MODIS for direct comparison against the GOES-16 ABI ~11 μm brightness temperatures. While the difference in nadir and off-nadir atmospheric path lengths may affect

this comparison, our choice of looking at clear-sky fall, winter, and spring days at our 3000 m elevation study minimizes these effects (Lundquist et al., 2018).

The MODIS snow-covered area and grain size (MODSCAG) snow fraction products (Painter et al., 2009), at 500 m spatial resolution, were downloaded from the NASA JPL Snow Data System website (accessible with a user account from https://snow-data.jpl.nasa.gov/modscag/) to provide daily fractional snow cover maps. Only the portion of each MODIS image that overlapped with ASTER was used, this being the nadir-most pointing portion of the full MODIS swath, avoiding any off-nadir MODIS view angles (Dozier et al., 2008). With MODIS and ASTER onboard the same satellite (as opposed to using some combination of other similar imagers on separate satellites, such as Landsat 8 TIRS, or NOAA-20 VIIRS) we could directly compare overlapping nadir-pointing thermal infrared images, without mismatched timing or different view angles.

2.4 Methods

2.4.1 Orthorectifying GOES-16 ABI Imagery

Solving the parallax problem for a geostationary satellite imager like ABI can be simplified given that, unlike polar-orbiting satellites, the satellite does not change its position relative to the Earth's surface while completing each image scan. In fact, GOES-16 ABI has high geolocation accuracy with errors much smaller than a single ABI pixel (e.g. <1 μrad for the 56 μrad IFOV channel 14 pixels is <36 m for a 2 km pixel), which we considered negligible in comparison to the geolocation error due to terrain parallax (Tan et al., 2018). Standard ABI image products are projected from the ABI Fixed Grid coordinate system (in image scan and elevation angles) to latitude and longitude using this known stationary geometry. This standard projection method, however, uses a smooth ellipsoid model (GRS80) of Earth, ignoring land surface elevation

variations over mountain terrain (NOAA, 2019), which for our study area translates to a geolocation error of more than 5 km. We modified this projection routine to create orthorectified ABI images, taking into account the terrain offset from the GRS 80 ellipsoid using a digital elevation model (DEM). In this orthorectification method, the intersection of line-of-sight vectors (emanating from the imager) and the land surface were computed (Marsetič et al., 2015). These line-of-sight vectors were then used to project each image pixel from ABI Fixed Grid coordinates into WGS84 (World Geodetic System 1984) latitude and longitude. This method has been previously applied to geostationary satellite imagery using DEMs at spatial resolutions near that of the imagery (500 m to 1 km) (Takeuchi, 2016; Takeuchi & Yasuoka, 2007; Wang et al., 2020). However, we used a DEM of higher spatial resolution than the ABI imagery to account for the complex mountain terrain and varying elevations within each ABI pixel. This subpixel orthorectification effectively draped each pixel over a much finer spatial resolution elevation model.

We developed a Python library(see Chapter 3) to orthorectify GOES ABI products at a range of spatial scales, from subpixel to multi-pixel, depending on the spatial resolution of the input DEM (Pestana et al., 2022). The original equations for computing line-of-sight vectors can be found in the GOES-R Series Product Definition and Users' Guide (NOAA, 2019) for projection of ABI images onto a smooth GRS 80 ellipsoid surface. With the addition of an elevation offset applied to the land surface point's Earth-centered distance, we adapted these equations to orthorectify ABI imagery at a subpixel spatial scale, by finding the ABI Fixed Grid coordinates for each grid cell in a DEM. We used a 90 m spatial resolution SRTM GL3 DEM (NASA SRTM, 2013) for the Sierra Nevada study area as our reference DEM. This DEM is at the same spatial resolution as our ASTER thermal infrared imagery, and the DEM's WGS84

EGM96 geoid vertical datum is nearly identical to the GRS 80 ellipsoid datum used for ABI products. For each grid cell in this DEM (with longitude, λ, and latitude, φ), its geocentric latitude (φ_c) (Equation 2.1) was first computed from its latitude, and Earth's polar (r_{pol}), and equatorial (r_{eq}) radii. The Earth-centered distance of each grid cell (r_c) (Equation 2.2) was then computed as the sum of the reference geoid Earth-centered distance (first term in Equation 2.2 which includes r_{pol}, φ_c, and GRS 80 polar eccentricity, e) and land surface elevation relative to the GRS 80 ellipsoid (Z).

$$\varphi_c = atan\left(\frac{r_{pol}^2}{r_{eq}^2} * tan(\varphi)\right) \tag{2.1}$$

$$r_c = \frac{r_{pol}}{\sqrt{1 - e^2 * cos(\varphi_c)^2}} + Z \tag{2.2}$$

Each DEM grid cell's location in satellite-centered coordinates (S_x, S_y, S_z) was then computed using satellite Earth-centered distance (H) and orbital longitude (λ_0), read from the ABI product metadata (Equation 2.3). These satellite-centered coordinates in units of meters (left side of Figure 2.3c) were transformed into scan (x) and elevation (y) angles, in units of radians, within the ABI Fixed Grid image coordinate system (Figure 2.3a) (Equation 2.4).

$$\begin{pmatrix} S_x \\ S_y \\ S_z \end{pmatrix} = \begin{pmatrix} H - r_c * cos(\varphi_c) \\ -r_c * cos(\varphi_c) * sin(\lambda - \lambda_0) \\ r_c * sin(\varphi_c) \end{pmatrix} \tag{2.3}$$

$$\begin{pmatrix} y \\ x \end{pmatrix} = \begin{pmatrix} atan\left(\frac{S_z}{S_x}\right) \\ asin\left(\frac{-S_y}{\sqrt{S_x^2 + S_y^2 + S_z^2}}\right) \end{pmatrix} \tag{2.4}$$

Finally, with each grid cell in the DEM having a set of coordinates in both latitude, longitude, and the ABI Fixed Grid, data values from the GOES ABI L1b Radiance product were

mapped from ABI Fixed Grid coordinates to latitude and longitude coordinates using the spatial coordinates of the DEM as a look up table (Figure 2.3b).

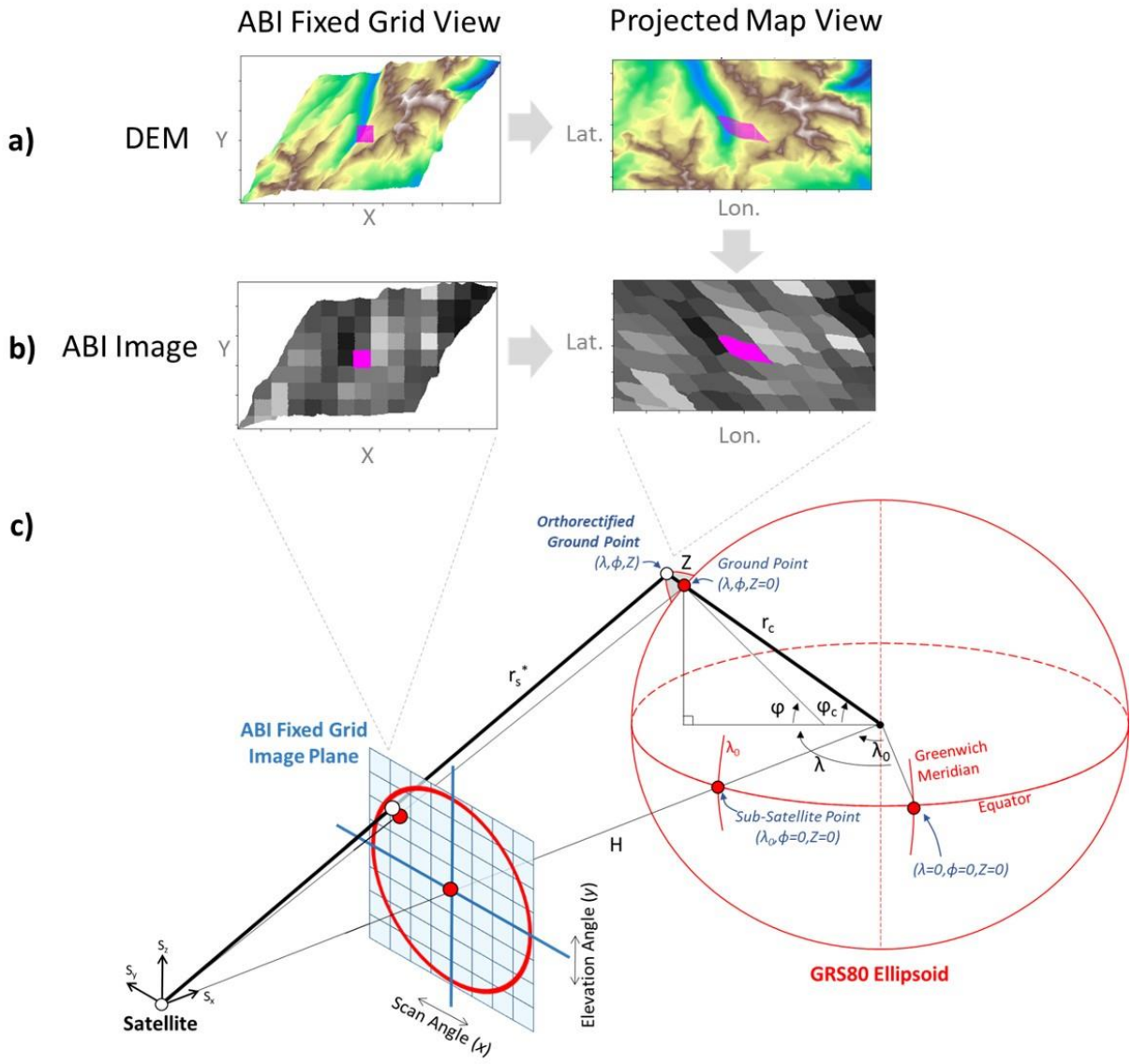

Figure 2.3. Conceptual figure and flowchart for orthorectifying ABI imagery. a) A subpixel spatial resolution DEM is used to define land surface deviations from the GRS80 Ellipsoid to b) map an ABI image from the ABI Fixed Grid into Latitude and Longitude, using c) the known satellite-Earth geometry. See text for explanation of symbols (geometry figure modified from NOAA, 2019).

2.4.2 Computing ΔT metrics

Each ASTER image was matched with its coincident MODIS image, and with the closest ABI CONUS image within 5 minutes of the ASTER observation time. Each coincident image set of ASTER, MODIS, and ABI was then converted from its original digital number or radiance values to radiance in W m^{-2} sr^{-1} μm^{-1} using their published conversion constants (GOES-R Calibration Working Group & GOES-R Program Office, 2017; MODIS MCST, 2018; Thome, 1999), and saved as a single NetCDF file. To compute the brightness temperature difference (ΔT) between a pair of images with different spatial resolutions (Figure 2.4a), the finer resolution imagery was first upscaled to the coarser resolution (Figure 2.4b). This upscaling, or aggregation, was performed by computing the mean radiance from all fine resolution pixels within the footprint of each coarse resolution pixel (Guillevic et al., 2012; Y. Liu et al., 2006). This was followed by converting the set of images from radiance to brightness temperature with the inverse Planck equation and published conversion constants for each dataset (GOES-R Calibration Working Group & GOES-R Program Office, 2017; MODIS MCST, 2018; Thome, 1999), then taking their differences (Figure 2.4c).

2.4.2.1 Evaluating orthorectified ABI imagery

After orthorectifying the ABI images for the study region, the $\Delta T_{ABI\text{-}AST}$ metric was computed between the coincident ASTER and both the original and orthorectified ABI images. The mean, standard deviation, standard error, distribution of both $\Delta T_{ABI\text{-}AST}$ metrics (before and after orthorectification), and the correlation between brightness temperatures were computed for each set of coincident ASTER and ABI images.

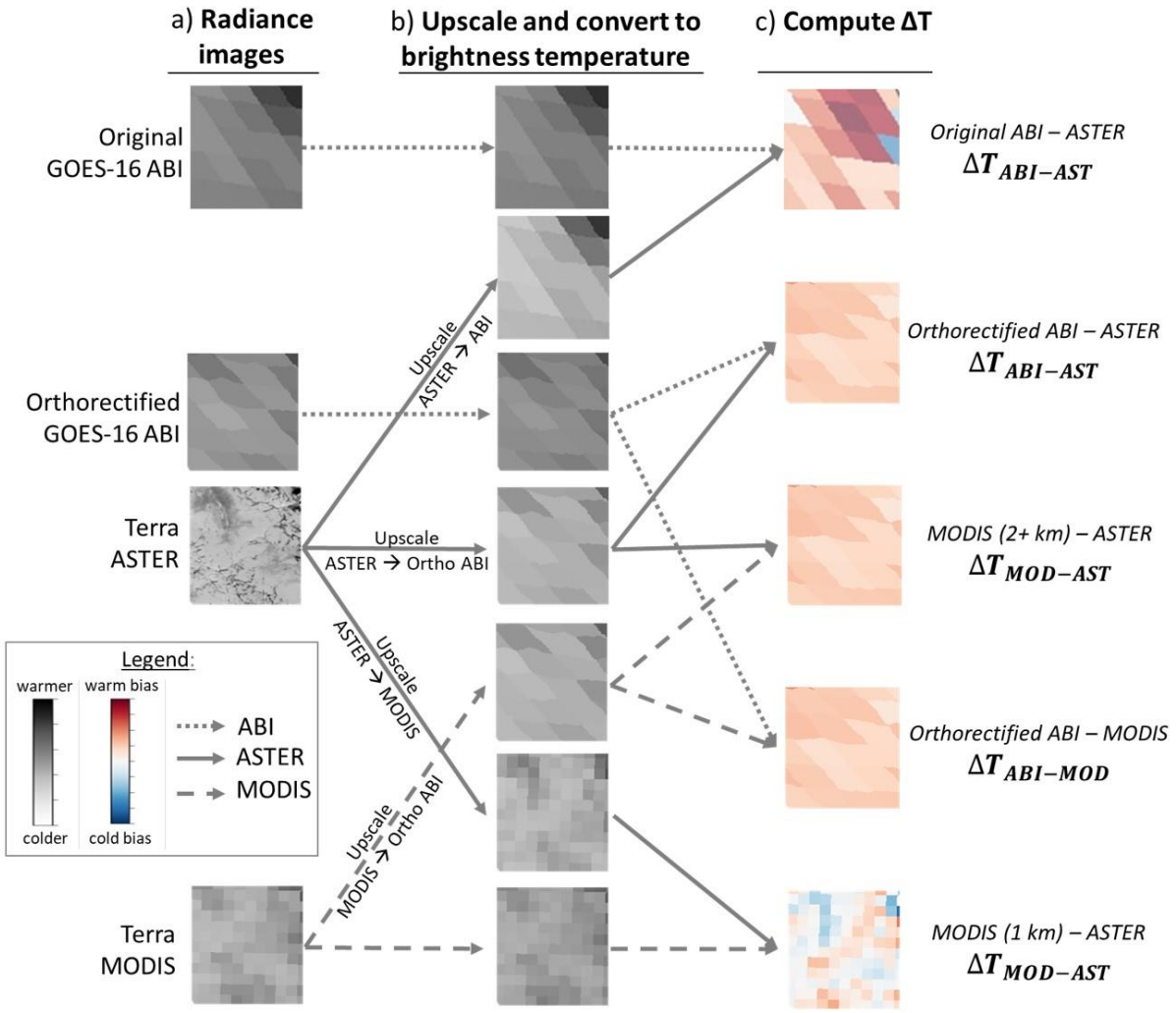

Figure 2.4. Flowchart for computing the various ΔT metrics used to evaluate GOES-16 ABI, starting with a) ABI, ASTER, and MODIS thermal infrared radiance images, then b) upscaling ASTER and MODIS to coarser resolutions, converting all radiance images to brightness temperatures, and finally c) taking the difference between pairs of brightness temperature images. Thumbnail images of ABI, ASTER, and MODIS reprojected to WGS84 are shown for illustration.

2.4.2.2 Coarse spatial resolutions versus off-nadir view angles

While pixels in any remote sensing imagery are subject to blurring during their retrieval due to scan motion and detector point spread functions (Barnes et al., 1998), the pixels in ABI products have additionally been resampled from the actual, finer, detector measurements to fit the ABI Fixed Grid. Therefore, in addition to the off-nadir view angle and coarser pixel sizes, the

radiance reported at each ABI pixel has already been partially mixed with neighboring detector samples, further blurring the images.

The relative contributions of coarse spatial resolutions, including this additional blurring effect, and off-nadir view angles to ΔT were investigated through comparisons of ASTER (nadir, 90 m), MODIS (nadir, 1 km), and ABI (off-nadir, 2+ km) brightness temperature images. First, we computed ΔT metrics between the nadir-looking MODIS and ASTER imagery. For coincident ASTER and MODIS image pairs, $\Delta T_{MOD-AST}$ was computed at both the native MODIS 1 km spatial resolution and at the coarser 2+ km pixel footprints of ABI. Next, $\Delta T_{ABI-MOD}$ was computed as the difference between ABI surface brightness temperature and MODIS upscaled to the ABI pixel footprints. The mean and standard deviation of all these differences, as well as a linear regression fit between each coincident brightness temperature image pair, were computed to assess how spatial resolution, view angle, and sampling characteristics contribute to the surface brightness temperature differences between each satellite imager.

2.4.3 ΔT and land surface properties

2.4.3.1 ΔT, insolation, and topography

To investigate how $\Delta T_{ABI-AST}$ varies as a function of topography, and the direction of incoming sunlight, slope and aspect maps at 90 m spatial resolution were computed from the same SRTM DEM used to orthorectify the ABI images. We then computed the correlation and created scatterplots looking for any potential relationship between $\Delta T_{ABI-AST}$ and each of: elevation, slope, aspect, and the diurnal anisotropic heating (DAH) index (Böhner & Antonić, 2009; Cristea et al., 2017). We further examined how ASTER surface temperatures of different portions of the land surface compared with ABI surface temperatures in the six image pairs from daytime observations. The land surface was classified into five zones defined by the values from

two hillshade maps. The first hillshade map was “illuminated” from the local azimuth and zenith angle of GOES-16, where the satellite view angles were calculated using the goes-ortho Python library (Pestana et al., 2022). The second hillshade map was “illuminated” from the local azimuth and zenith angle of the sun at the time the images were taken, calculated using the pysolar Python library (Stafford, 2021). The hillshade maps receive values between -1 and 1, where a mountain slope perfectly perpendicular to the “illumination” would have a value of 1, slopes parallel would have a value of 0, and any land surface occluded from view (in full “shadow”) would have a value less than 0.

The median value of each hillshade map was used as a threshold value to create discrete classification maps, delineating “satellite-facing” (Figure 2.5a) or “sun-facing” (Figure 2.5b) slopes (hillshade values from the median to 1) from “away-facing” slopes (hillshade values less than the median but greater than 0). An additional class was defined for the land surface occluded by terrain from view of ABI (hillshade values less than 0) (Figure 2.5a). The two classified hillshade maps were combined (Figure 2.5c), resulting in a total of five zones for the different possible combinations of satellite view and solar illumination angles: sun- and satellite-facing, only sun-facing, only satellite-facing, facing away from both, or occluded from the satellite’s view . For each of the six daytime image pairs, the mean and distribution of ASTER surface brightness temperatures within each zone were computed, and a linear regression fit between all daytime zonal means from ASTER and image-wide mean brightness temperatures from ABI.

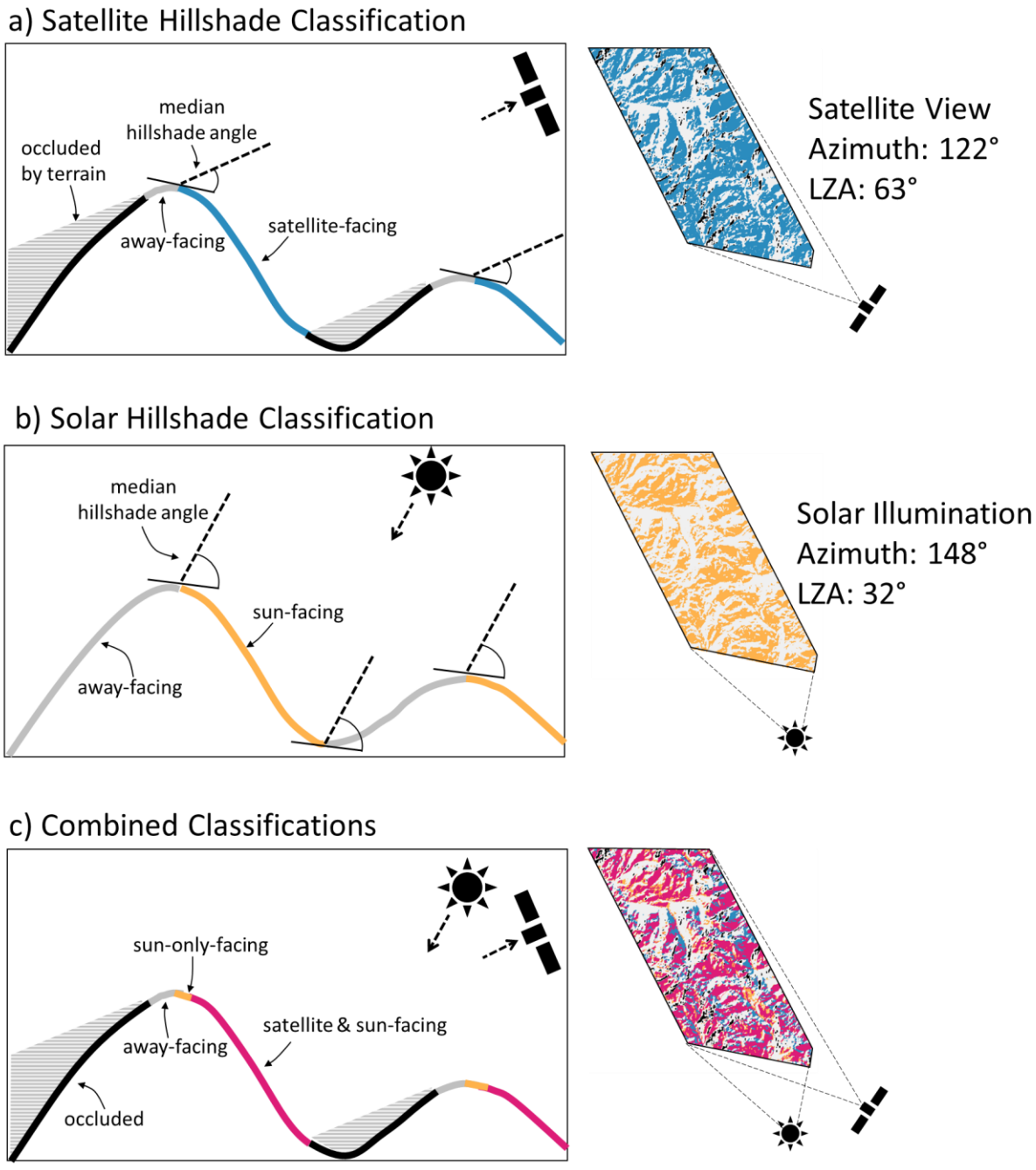

Figure 2.5. Classifying hillshade maps into a) satellite-facing (blue), away-facing (grey), terrain occluded from view (black), b) sun-facing (yellow), and away-facing (grey), and finally c) with the intersection of sun- and satellite-facing terrain colored magenta. Example classified maps with satellite and solar azimuth and local zenith angles (LZA) are shown for April 13, 2020.

2.4.3.2 ΔT, vegetation, and snow cover

The relationships between $\Delta T_{ABI-AST}$, fractional vegetated area (f_{veg}), and fractional visible snow covered area (f_{SCA}) were investigated first at the spatial resolution of the ABI imagery. A constant f_{veg} map was derived from the NLCD TCC product by first converting the 30 m spatial resolution TCC map to a binary forest cover map, where any TCC value greater than zero was considered forested, and TCC values of zero as non-forested. An f_{veg} value within each ABI pixel footprint was then computed as the number of forested 30 m pixels divided by the total number of 30 m pixels it contained. The MODSCAG snow fraction product from the day of each ABI/ASTER image pair was used to derive f_{SCA} maps. For each ABI pixel footprint f_{SCA} was computed as the mean value of all 500 m spatial resolution MODSCAG f_{SCA} grid cells within the footprint. We computed the correlation and tested for any linear relationship between $\Delta T_{ABI-AST}$ and each of f_{SCA}, and f_{veg} on a pixel-by-pixel basis and on aggregate for the entire study area.

Here, f_{veg} and f_{SCA} were treated independently: f_{veg} was derived from a static vegetation map dataset, whereas f_{SCA} was derived from a daily remote sensing product and therefore varied over time. This means that for each ABI pixel, f_{veg} and f_{SCA} did not necessarily sum up to 1. Our use of an f_{veg} map independent of snow cover was intended to represent forested areas regardless of whether the area was snow-covered or not. Using the non-vegetation-corrected snow fraction MODSCAG product allows us to only consider the snow fraction visible from nadir-looking MODIS, such as within forest gaps or intercepted within the forest canopy, rather than including snow hidden beneath the canopy.

We next explored the surface brightness temperatures in the finer spatial resolution ASTER imagery within forested, open, snow-covered, and mostly snow-free portions of the land surface. The 30 m spatial resolution TCC map was converted to a binary forest cover map by assigning any grid cell with TCC > 0 as forest, and TCC = 0 as open. The 500 m resolution MODSCAG

f_{SCA} product from the day of each ABI/ASTER image pair was similarly used to derive a binary snow map, with a threshold defined at 50% f_{SCA}. The mean and standard deviation of ASTER brightness temperatures for the forested, open, f_{SCA}>50%, and f_{SCA}<50% zones were computed and compared with the image-wide mean ABI brightness temperatures, and a linear regression fit between the means of all image pairs.

2.5 Results

2.5.1 Orthorectified GOES-16 ABI imagery

Prior to orthorectifying the ABI images, the mean $\Delta T_{ABI-AST}$ of all images pairs over the study area was 1.6 °C (Figure 2.6a), and a linear fit to these ABI and ASTER brightness temperatures had a slope of 0.68 and r-squared of 0.43 (Figure 2.6b). After orthorectifying the ABI images, the mean difference was reduced to 1.0 °C, (Figure 2.6c), the linear fit slope increased to 0.89, and r-squared increased to 0.93 (Figure 2.6d). Daytime images, which had the highest mean ΔTABI-AST values (> 4.0 °C) originally, showed the largest decrease in mean $\Delta T_{ABI-AST}$ after orthorectifying (a reduction of about 1.0 °C), while this reduction was smaller for nighttime images.

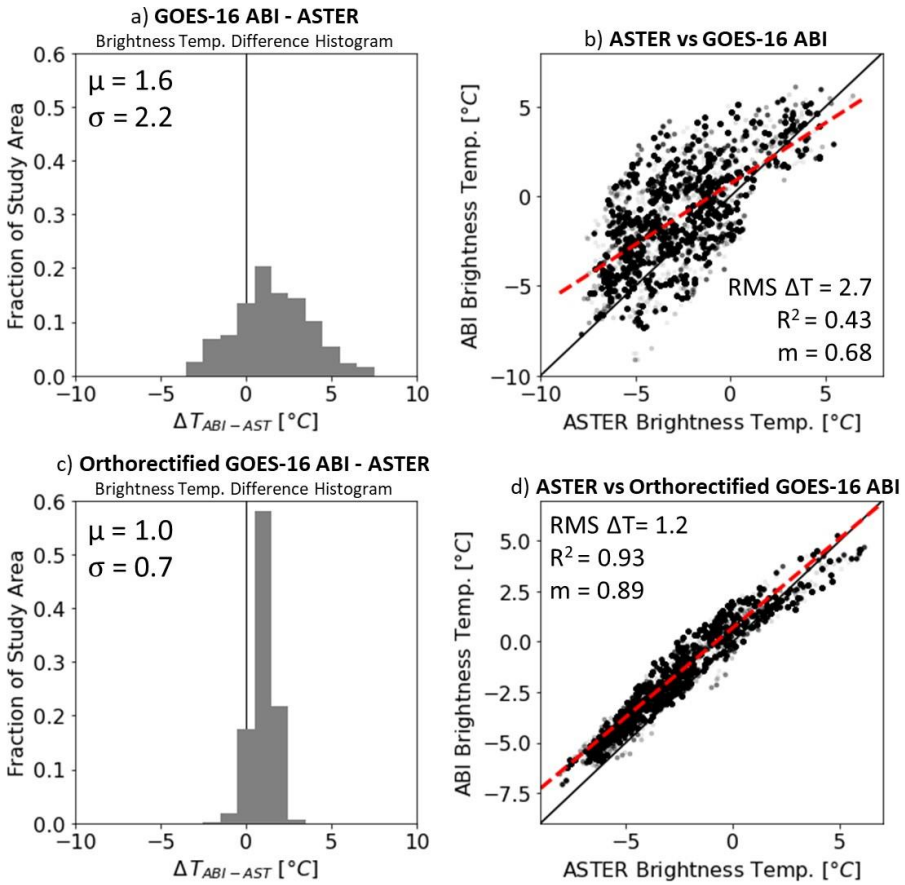

Figure 2.6. Histograms with the mean (μ) and standard deviation (σ) of ΔT a) prior to, and c) after orthorectifying. Scatterplots of surface brightness temperature from ASTER versus ABI with root mean squared (RMS) ΔT, r-squared, and slope (m) values for the regression lines b) prior to, and d) after orthorectifying.

2.5.2 Land surface properties

2.5.2.1 Insolation and topography

The difference in the orthorectified ΔTABI-AST between daytime and nighttime images was most apparent, with mean values of ΔTABI-AST of 2.4 °C in daytime images (Figure 2.7a) and 0.7 °C at night (Figure 2.7b). However, we did not find any significant relationships between $\Delta T_{ABI\text{-}AST}$ and each of elevation, slope, aspect, or DAH. Values of $\Delta T_{ABI\text{-}AST}$ appear nearly uniformly distributed across the full range of each of these topographic variables.

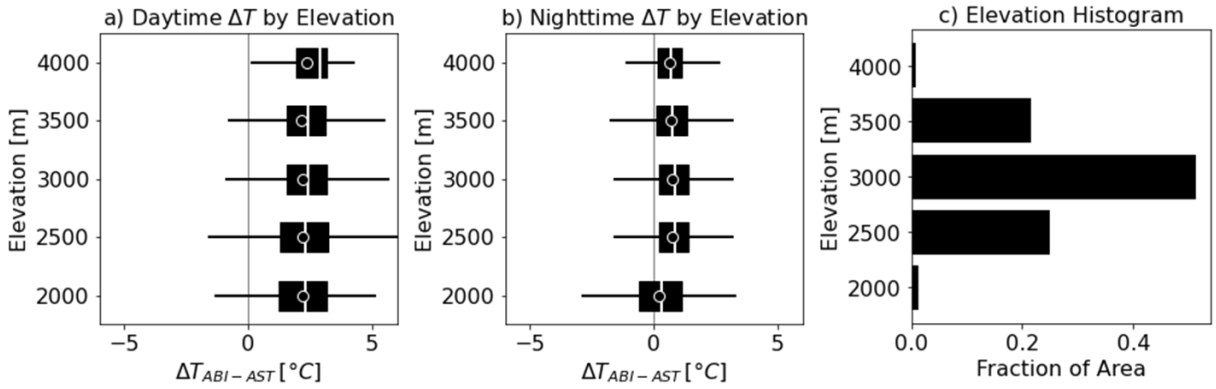

Figure 2.7. Boxplots of orthorectified ΔTABI-AST broken into 500 m elevation bins for a) daytime and b) nighttime imagery showing the warmer bias in ABI brightness temperatures in daytime imagery, but no apparent elevation dependence for $\Delta T_{ABI-AST}$. Boxes represent the inter-quartile range (IQR), white lines the median, white circles the mean, and whiskers are +/- 1.5 IQR. c) Histogram showing the distribution of elevations across the study area binned in 500 m intervals.

GOES-16 ABI views the study area from the southeast, the same general direction of incoming morning sunlight, therefore most of the land surface was classified into either the sun- and satellite-facing zone (>40%) or away-facing zone (>30%). The mean brightness temperature from ASTER imagery of the mountain slopes facing GOES-16 ABI (Figure 2.8a,c) more closely matched the brightness temperatures reported by ABI with RMS differences of 1.6 °C and 2.0 °C respectively. In the daytime observations, most of the mountain slopes facing GOES-16 ABI (Figure 2.8a) were the warmest parts of the land surface as seen by ASTER. The RMS difference between ASTER surface temperatures in the sun- and satellite-facing zone and the ABI image-wide mean was the smallest of all zones, at 1.6 °C, while the away-facing zone had an RMS difference of 3.4 °C. Less than 3% of the land surface was occluded by surrounding terrain from view of GOES-16 ABI (Figure 2.8e); these had the largest RMS difference of 4.7 °C. While only a small percentage of the whole area, the fact that the nadir-looking ASTER could see these coldest slopes while ABI did not could have further contributed to the warm daytime bias of ABI images over this study area. With these occluded areas removed from ASTER, the image-wide

mean brightness increased by less than 0.1 °C on average suggesting that terrain occlusion had a negligible effect on the results. The other two zones, sun-only-facing (Figure 2.8b) and satellite-only facing (Figure 2.8c), each covered no more than 12% of the land surface, and had RMS differences of 2.7 and 2.0 °C, respectively.

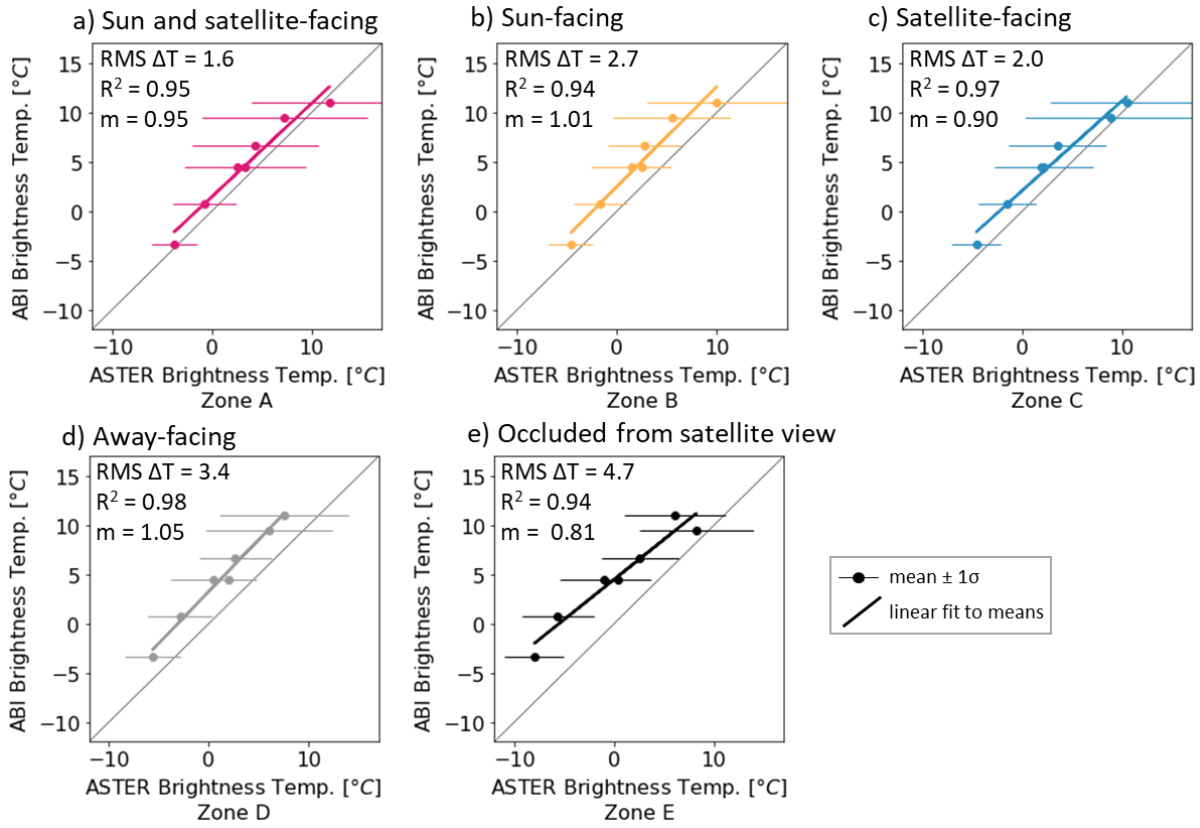

Figure 2.8. Mean (circles) and standard deviations (horizontal bars) of ASTER surface brightness temperature by zone plotted against the image-wide ABI brightness temperature from the seven daytime image pairs (with RMS ΔT, r-squared, and slope (m) for the regression lines). The zones in ASTER imagery are classified by whether the topography is a) both sun- and satellite-facing, b) sun-facing only, c) satellite-facing only, d) facing away from both, or e) completely occluded by the surrounding terrain from view.

The mountain slopes facing GOES-16 (Figure 2.8a,c) have a larger apparent size in ABI images due to the parallax effect (Figure 2.1a), and therefore contribute more to the overall thermal infrared radiance sensed. Since these same slopes are largely sun-facing (Figure 2.8a) and are the warmest parts of the land surface in this morning imagery, we can expect their

temperatures to be overrepresented in off-nadir GOES-16 ABI imagery, suggesting that some of the warm bias seen in the daytime ABI images stems from sunlight warming these slopes.

2.5.2.1 Fractional snow covered area and forests

There were no significant linear relationships between $\Delta T_{ABI\text{-}AST}$, and each of f_{SCA} or f_{veg} at the coarser spatial resolution of ABI. In daytime images, primarily snow-covered areas (f_{SCA} > 50%) had a mean $\Delta T_{ABI\text{-}AST}$ of 2.5 °C, and primarily snow-free areas (f_{SCA} < 50%) had a mean $\Delta T_{ABI\text{-}AST}$ of 1.5 °C, while in nighttime images these areas had very similar ΔTABI-AST values (0.8 and 0.7 °C respectively) (Figure 2.9a). Though the daytime mean ΔTABI-AST values are different between areas with more or less snow cover, ΔTABI-AST varies widely within each area and this was not found to be statistically significant, suggesting that fSCA alone cannot explain the differences between ABI and ASTER surface brightness temperatures. For both day and nighttime images, mean ΔTABI-AST does not differ more than about 0.1 °C between areas with fveg above or below 50% fveg (Figure 2.9b) suggesting that f_{veg} also cannot explain these differences. However, because warmer objects emit more radiance at shorter wavelengths, as described by Wien's displacement law, relationships between $\Delta T_{ABI\text{-}AST}$ and fractional snow covered area could be investigated further using mid-wave IR observations in conjunction with the ~11 um observations used here (Dozier, 1981; Lundquist et al., 2018).

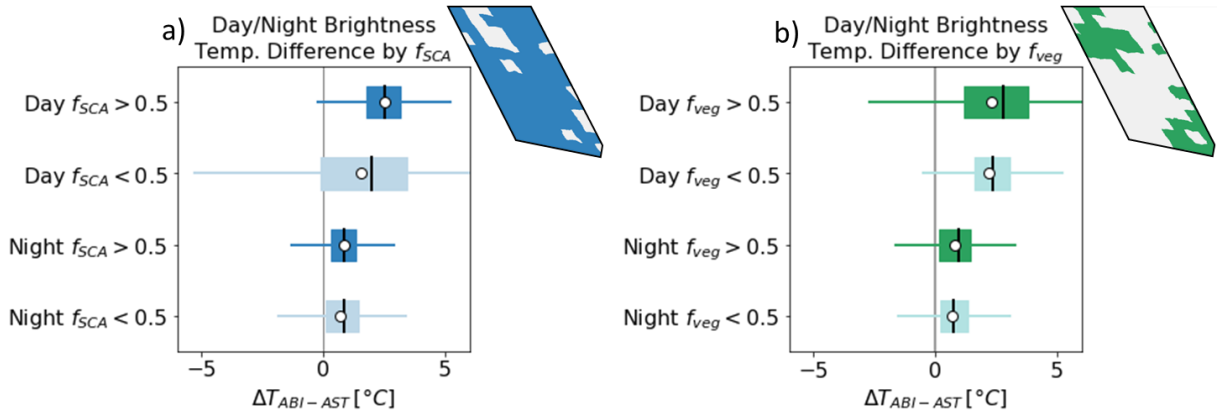

Figure 2.9. Boxplots of ΔTABI-AST binned by day and night for a) fSCA greater or less than 50%, and b) fveg greater or less than 50%. Boxes represent the inter-quartile range (IQR), black lines the median, white circles the mean, and whiskers are +/- 1.5 IQR. Inset images show example maps of a) f_{SCA} and b) f_{veg} aggregated to the 2+ km resolution ABI pixel footprints.

When ASTER images were classified by the binary (500 m spatial resolution) MODSCAG fSCA map (Figure 2.10a), the RMS difference between ASTER brightness temperature in areas with fSCA>50% and ABI brightness temperatures (3.0 °C) was greater than that of areas with fSCA<50% (1.3 °C). ASTER brightness temperatures within forested areas (30 m spatial resolution; TCC>0) had an RMS difference of only 1.2 °C when compared to ABI, versus 2.2 °C for open areas (TCC=0) (Figure 2.10b). That ABI brightness temperatures better match that of forested areas and areas with f_{SCA}<50% further suggests the importance of view angle, and how from off-nadir ABI is seeing a different portion of the land surface, specifically the sides of trees and fewer forest gaps, than ASTER.

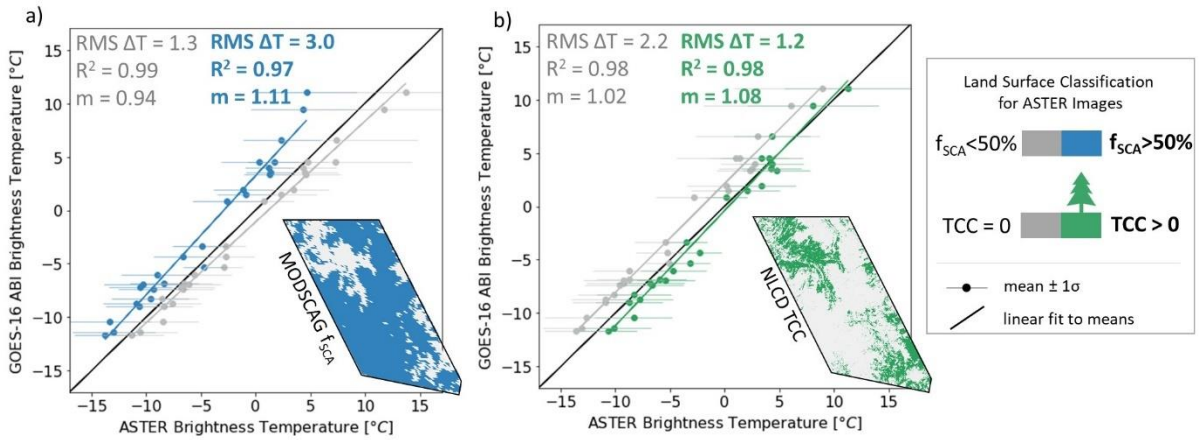

Figure 2.10. Mean (circles) and standard deviations (horizontal bars) of ASTER surface brightness temperature partitioned by a) snow and b) forest cover, against the image-wide ABI brightness temperature (with RMS ΔT, r-squared, and slope (m) for the regression lines). Inset images show example maps of binarized a) 500 m spatial resolution MODSCAG fSCA and b) 30 m spatial resolution NLCD TCC.

The MODSCAG f_{SCA} represents snow cover visible by a nadir-looking imager. However, GOES-16 ABI has a local zenith angle (LZA) of 63° in this study area, and the parallax effect causes gaps in the forest (smaller than about two tree heights) to be obscured by the surrounding trees. ABI can only sense the radiance coming from the sides of those trees rather than from the snow surface within the small forest gaps (Pestana et al., 2019). The mean temperature of the forested portions of each ASTER image more closely matches the temperatures seen by ABI for both day and nighttime image pairs. In daytime images, trees are likely to be equal to, or, for the portion of the tree canopy in sunlight (Martin et al., 1999; Pestana et al., 2019), warmer than local air temperatures, and therefore warmer than snow surface temperatures (Howard & Stull, 2013; Lundquist et al., 2018). In the nadir-looking ASTER images, where the projected areas of individual trees are limited to their crown areas, increasing f_{SCA} values will translate to an overall colder land surface, since snow in forest gaps contributes to the sensed radiance. From the off-nadir view of ABI. those same changes in f_{SCA} are obscured by trees, and the temperatures

sensed are biased towards the temperature of the trees. This effect, combined with the GOES-16 ABI view angle coinciding with the direction of morning sunlight, results in these daytime images overrepresenting the surface brightness temperatures of the warmer sunlit forest canopies compared to a nadir view of the same scene. Though nighttime ABI images have the same view angles, and forest canopies still obscure snow surfaces (Figure 2.1c), without solar heating the canopies cool to more closely match snow surface temperatures (Essery et al., 2008; Lundquist et al., 2018; Webster et al., 2017), reducing the difference between surface brightness temperatures seen from off-nadir and nadir.

2.5.3 Coarsening spatial resolutions versus off-nadir view angles

Comparing the two nadir-looking imagers (MODIS and ASTER), mean ΔTMOD-AST did not differ significantly between being computed at the original 1 km (Figure 2.11a), or the coarsened 2+ km spatial resolutions (Figure 2.11b). Only the spread of ΔTMOD-AST values was different between the two spatial resolutions considered, as the larger magnitude differences seen at 1 km are subdued when blurred more at the coarser 2+ km resolution. Comparing off-nadir ABI and nadir-looking ASTER (scaled to ABI pixel footprints), the mean ΔTABI-AST was biased warm (Figure 2.11c), even after the improvements seen with orthorectifying ABI imagery (Section 2.5.1).

Table 2.2. Results of ΔT comparisons at different spatial resolutions (either 1 km MODIS resolution, or 2+ km ABI), and view geometries (either both imagers nadir, or one imager nadir with ABI off-nadir). For each ΔT metric the mean (μ), standard deviation (σ), standard error (SE) are computed. From a linear fit between each pair of brightness temperatures, the root-mean-squared (RMS), slope (m), and coefficient of determination (r^2) are also computed.

Metric	**Spatial Resolution**	**View**	**μ**	**σ**	**SE**	**RMS ΔT**	**m**	**r^2**
$\Delta T_{MOD-AST}$	1 km	Both nadir	-0.2	1.7	0.005	1.7	0.65	0.64
$\Delta T_{MOD-AST}$	2+ km	Both nadir	0.3	1.2	0.003	1.2	0.77	0.79
$\Delta T_{ABI-AST}$	2+ km	ABI off-nadir	1.0	0.7	0.002	1.2	0.89	0.93
$\Delta T_{ABI-MOD}$	2+ km	ABI off-nadir	1.3	0.9	0.003	1.6	0.97	0.84

This suggests that MODIS may better represent the mean ASTER surface brightness temperatures than ABI, which was biased warm (though both have nearly equal RMS ΔT of 1.2 °C). However, MODIS seems to underestimate the warmest and overestimate the coldest brightness temperatures in the ASTER images more than ABI, even though ABI images are ostensibly blurred more in image preprocessing. Rather than the coarser resolution of ABI, its off-nadir view angle could be having a larger influence on $\Delta T_{ABI-AST}$ and the warm bias seen for this study area and time period. Results from Section 2.5.2 similarly suggest that the differences between ASTER and ABI are attributable to each seeing different parts of the same land surface. Upscaling ASTER brightness temperatures weighted by the cosine of the incident view angle and excluding occluded terrain, however, only improved $\Delta T_{ABI-AST}$ negligibly (decreased by < 0.1 °C).

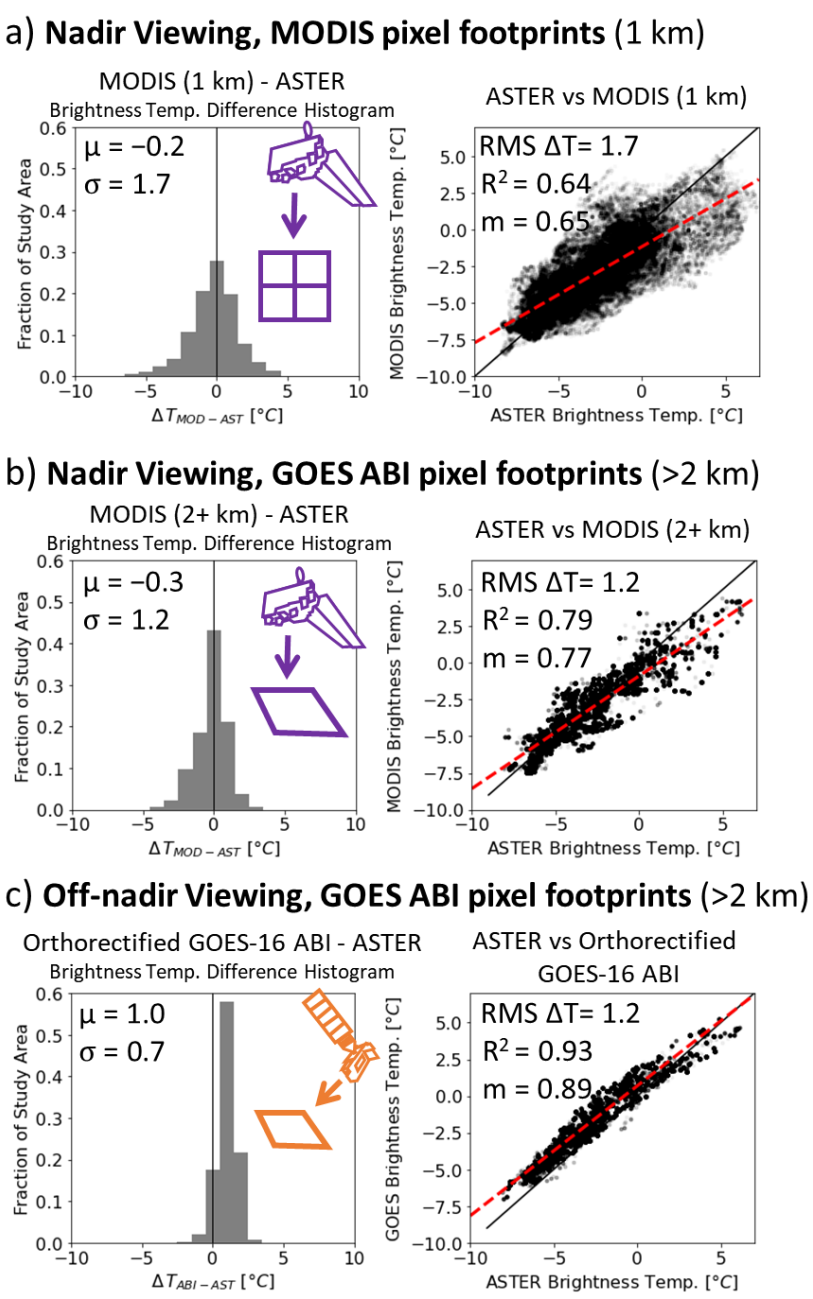

Figure 2.11. Histograms with the mean (μ) and standard deviation (σ) of ΔT, and scatterplots of surface brightness temperatures with RMS ΔT, r-squared, and slope (m) values for the regression lines. Plots show ASTER brightness temperatures with a) the original 1 km spatial resolution MODIS brightness temperatures, b) MODIS brightness temperatures coarsened to 2+ km ABI pixel footprints, and c) orthorectified 2+ km ABI brightness temperatures.

2.6 Discussion

Our results showed that the orthorectified ABI brightness temperatures more closely matched ASTER brightness temperatures (decreased $\Delta T_{ABI-AST}$) than did the original ABI product. This result demonstrates that orthorectifying improved the alignment of the off-nadir GOES-16 ABI and nadir-looking ASTER imagery. Orthorectification will be important for any applications of ABI imagery for land surface observations in mountainous areas, including detecting wildfires and volcanic hotspots (Harris et al., 2001; Koltunov et al., 2016) or estimating evapotranspiration (Anderson et al., 2011). However, even after orthorectification, the 11 μm brightness temperatures observed by GOES-16 ABI were warmer than those observed by ASTER. We found evidence that GOES-16 ABI surface brightness temperatures are biased towards those of the sunlit slopes in daytime imagery, and closer to forest temperatures than snow surface temperatures in both day and nighttime imagery. Consideration of the underlying terrain and land cover will be essential for any applications of ABI imagery, especially in forested mountain areas. Though the differences between MODIS and ASTER ($\Delta T_{MOD-AST}$) were unbiased, MODIS was also subject to blurring and therefore did not represent an exact mean ASTER temperature within each of its pixels. We showed in comparisons against higher spatial resolution ASTER imagery that ABI is approaching the performance of MODIS, with the additional advantage of its much higher temporal resolution. This opens the possibility of extending land surface observation applications currently performed by MODIS and other moderate resolution polar-orbiting satellite imagers to ABI, with the benefits of its improved spatial and temporal resolutions over prior generations of geostationary imagers.

2.6.1 Off-nadir view angles and the atmosphere

The nadir and off-nadir looking satellite imagers used in this study view the land surface though different atmospheric paths, which could lead to differences in the surface brightness temperatures measured due to different amounts of water vapor absorbing thermal infrared radiation along each path. As an example, for a ground point in our study area, GOES-16 ABI has a local zenith angle of approximately 63°, and azimuth angle of 122°. Considering that >99% of water vapor is in the troposphere, the atmospheric path from this ground point through a 15 km thick troposphere will be 33 km for ABI imagery, more than twice that of the nadir-looking ASTER. Presuming similar water vapor concentrations in these paths, the longer path alone would translate to off-nadir images appearing colder than nadir images of the same scene. In geostationary satellite imagers, this is referred to as "limb darkening," as the apparent surface temperature decreases with larger LZAs towards the visible limb of the Earth (Joyce et al., 2001; Sun & Pinker, 2003).

Different water vapor concentrations along the paths would have more influence, particularly if clouds exist along one path but not the other. Prior work has shown that the parallax effect also causes clouds to have an apparent horizontal offset, and this effect has been used to determine cloud top heights from off-nadir or stereo pairs of satellite images (Wylie et al., 1998; Young, 2021) (Wylie et al., 1998; Young, 2021). In the process of testing the orthorectification method, two image pairs that did not improve with orthorectification stood out, each of which had an original mean $\Delta T_{ABI\text{-}AST}$<-5 °C. Further inspection of the ABI, MODIS, and ASTER images from these two dates showed that the large magnitude $\Delta T_{ABI\text{-}AST}$ values come from misalignment of thin cloud cover in the ABI image, which was not apparent in the ASTER images. Imagery from these two dates were excluded from later analyses.

Considering cases without clouds, the ABI atmospheric path exits the top of the troposphere about 29 km southeast of the ground point. If atmospheric water vapor varied horizontally across this 29 km distance, this could influence brightness temperature differences seen between ABI and ASTER. However, for our study area the off-nadir atmospheric path of GOES-16 ABI towards the southeast lies entirely over the central Sierra Nevada. By focusing on a high elevation study area during clear-sky conditions in the cooler snow season months when the atmosphere is drier (Lundquist et al., 2018) we have attempted to minimize these effects. A MODTRAN (Berk et al., 2014) simulation of a mid-latitude winter atmosphere showed that the difference in transmittance between a nadir and 45° off-nadir atmospheric path at 11 μm was 0.03, such that a surface at 0 °C would appear to be -1.7 °C when viewed off-nadir.

Rather than the limb darkening expected in off-nadir thermal infrared images, our results showed that ABI had a warm bias compared to the nadir-looking ASTER, suggesting that any limb darkening effect due to trace water vapor was smaller than the effect of ABI preferentially viewing sunlit slopes. Similarly, had we used an ABI LST product (presuming it didn't mask out the study area as misidentified clouds), its correction for these atmospheric effects would lead to the warm bias we identified appearing even larger.

2.6.2 LST algorithms, view angle and emissivity

The three imagers compared here differ widely in how their Land Surface Temperature (LST) algorithms handle emissivity. The GOES-R LST product uses a monthly emissivity dataset at 0.05 degrees spatial resolution derived from MODIS observations for its split window (SW) method of computing LST (GOES-R. Calibration Working Group & GOES-R Program Office, 2018). The MODIS MOD11_L2 LST product is created using a SW method and land cover information with emissivity from a look up table (Z. Wan, 1999), while the MODIS

MOD21A1 LST&E and ASTER AST08 products solve for emissivity alongside temperature using temperature emissivity separation (TES) methods (Hulley et al., 2012; Thome, 1999).

The remote sensing data used from each of the three satellite imagers were top of atmosphere radiance products. By using the directly observed top of atmosphere radiance products for bands centered around ~11 μm, we avoided introducing additional differences into our analysis from different emissivity datasets. Our comparisons between the three thermal infrared imagers did not consider surface emissivity, but instead compared brightness temperatures computed from spectral radiance through the Planck function. Rather than assume any particular surface emissivities, this only assumed that the effective emissivity (Li & Wang, 1999) seen from each satellite sensor is the same, regardless of view angle or differences in the spectral response functions (SRF) of each sensor. While different view angles will have different apparent fractional vegetated area (the inverse of visible gap fraction), because snow and conifer trees have similar emissivities, the effective emissivity of a mixed pixel would remain nearly the same whether more snow or trees are visible. This, however, would not hold true for mixed pixels containing drought-stressed or burned trees, exposed soil, or rocks which have more angular emissivity variation. The emissivity of green vegetation alone has little variation due to view angle (Salisbury & D´Aria, 1992), but snow emissivity does change with large view angles (Warren, 1982). Around 11 μm, snow emissivity at view angles of 0° (nadir) to 45° is > 0.98 for medium-grained snow (Dozier & Warren, 1982; Hori et al., 2013), and at view angles around 60° can be as low as 0.95 for coarse-grained snow (Hori et al., 2006; Warren, 2019). Therefore a coarse-grained snow surface at 0 °C would appear to be about -2.9 °C when viewed from a 60° LZA. GOES-16 ABI has a LZA of about 63° in this study area, though this angle will also vary with the slope and aspect of terrain at the subpixel level such that, slopes facing GOES-16 will

have much smaller LZAs, and slopes facing away will have larger LZAs. We would expect the reduced emissivity of snow at these larger zenith angles to translate to colder apparent snow surface temperatures, but as in the case of limb-darkening discussed above, we instead observed a warm bias. Therefore, it's likely that any effect of reduced emissivity at off-nadir view angles is less than the effect of viewing warmer portions of the land surface (trees and sunlit mountain slopes).

2.6.3 ABI Fixed Grid resampling

There is additional uncertainty in what radiance, and therefore brightness temperatures, each ABI Fixed Grid pixel represents given that it has been resampled from a window of detector samples (Kalluri et al., 2018). While this could be a source of disagreement between ASTER and ABI, we might expect this to contribute a randomly distributed or unbiased error rather than the biased ΔT observed. Similarly, we treated ABI pixel footprints as discrete zones when aggregating maps of f_{veg} (from 30 m TCC) and f_{SCA} (from 500 m MODSCAG). However, the fractional snow and vegetated areas computed for each discrete ABI pixel footprint is not necessarily the fractional area corresponding to the radiances actually sensed by the detectors because of the resampling to the ABI Fixed Grid. Though our subpixel orthorectification was performed on the ABI Fixed Grid pixels, ideally this process could be done with the original Level 0 detector samples (of slightly finer spatial resolution) as part of the "navigation" step of the Ground Processing Algorithm (NOAA-NASA, 2019). The orthorectified and navigated samples could then be resampled to the ABI Fixed Grid for delivery as Level 1b products, a step currently proposed for future GeoNEX products (Wang et al., 2020).

2.7 Conclusions

Images of mountain terrain from GOES-16 ABI require a terrain correction, or orthorectification, to properly align them with nadir-looking satellite images. Ostensibly this applies to mountain imagery from all geostationary imagers (EUMETSAT Meteosat SEVIRI, JAXA Himawari-8 AHI, and CMA Feng-Yun 4A) to align their products with other imagery or maps. We demonstrated this by orthorectifying GOES-16 ABI at a subpixel spatial resolution to improve its agreement with nadir-looking ASTER, reducing the mean difference from 1.6 °C to 1.0 °C and improving the r-squared value between ABI and ASTER thermal infrared brightness temperatures from 0.43 to 0.93. This will be especially important for merging or gap-filling with pairs of GOES-East and -West or Himawari-8 and Feng-Yun 4 imagery, or for downscaling or sensor fusion models using geostationary satellite imagery over mountains rather than flat terrain (Chen et al., 2021; Desai et al., 2021).

Our analysis of the relative effects of spatial resolution and view angle on the difference between ABI, MODIS, and ASTER surface brightness temperatures showed that by coarsening spatial resolutions alone (coarsening MODIS to ABI spatial resolution) these differences remained unbiased. This suggests that the warm bias seen in ABI images compared to ASTER is a function of its off-nadir view angle and the different portion of the land surface imaged (e.g., sunlit mountain slopes, gaps within forests).

Wherever there is mountain terrain requiring orthorectification, there is likely to be underlying heterogeneous land surfaces within each pixel. Therefore, interpreting ABI observations of mountain surface temperatures also requires understanding how each pixel is a mixture of different subpixel temperatures and how its view angle changes which portions of the land surface are seen. ABI brightness temperatures in this study area were found to more closely

match those of the satellite-facing sunlit slopes than slopes facing away from the sun and satellite (with RMS differences of 1.6 °C and 3.4 °C, respectively) in coincident ASTER imagery. In this study area, daytime ASTER observations were made when the direction of view of GOES-16 ABI and the direction of incoming sunlight were similar. We expect that there will be other unique relationships between ABI thermal infrared brightness temperatures and finer resolution surface brightness temperature observations for other mountain locations and at different times of day.

Because its off-nadir view angle precludes ABI from sensing the radiance from snow in forest gaps, ABI instead provides surface temperature observations more representative of forest canopy temperatures, unencumbered by significant mixed signals from soil or snow. In this work, we found that ABI brightness temperatures more closely match those of forest canopy temperatures than snow surface (with RMS differences of 1.2 °C and 3.0 °C respectively). We could expect that as snow cover decreases, this bias may disappear if forests and the snow-free land surface are at similar temperatures, or invert if land surfaces are warmer than forests. Since these tree temperatures closely match near-surface air temperatures, methods of using satellite observations to observe air temperature lapse rates over complex mountain terrain (Pepin et al., 2019; Shamir & Georgakakos, 2014; Williamson et al., 2017) could now be extended to ABI high temporal resolution observations.

With this improved understanding of the influences that mountain terrain and heterogeneous forest and snow-covered surfaces have on the thermal infrared brightness temperatures observed by GOES-16 ABI, we can better understand how to interpret and apply these observations. Future work downscaling ABI or sensor fusion between ABI and other satellite imagers (Desai et al., 2021; Weng & Fu, 2014; Wu et al., 2015) will need to consider and compensate for the

effects that terrain and forested land surfaces have on ABI brightness temperature observations for mountain terrain, such as through orthorectification demonstrated in this work, as well as through terrain-based downscaling (Cristea et al., 2017; Ding et al., 2018; Maeda, 2014; Walters, 2013). These future efforts can then leverage the full high temporal resolution and spatially contiguous GOES ABI imagery to help improve or correct biases in land surface models and provide new observational capabilities for temperature lapse rates and diurnal temperature ranges in mountains.

2.8 Acknowledgements

We would like to thank Nicoleta Cristea, Michelle Hu, Cassie Lumbrazo, Calista Moore, Justin Pflug, Kehan Yang, and the Mountain Hydrology Research group for their comments and feedback on the manuscript. Additionally, we would like to thank Jeff Dozier and our other two anonymous reviewers for their helpful suggestions to improve this manuscript. This work was supported by NASA FINESST grant 80NSSC20K1610 and NASA grant NNX17AL59G..

Chapter 3. goes_ortho: A Python package for orthorectifying GOES-R ABI image products

Steven Pestana [1]

[1] Civil and Environmental Engineering, University of Washington, Seattle, WA, USA

3.1 Summary

The goes_ortho Python package (Pestana et al., 2022) orthorectifies GOES-R Advanced Baseline Imager (ABI) image products for the purpose of accurate scientific analysis and comparison to other terrain-projected datasets. Image products from GOES-R ABI come projected in ABI Fixed Grid coordinates, with scan (x) and elevation angle (y) dimensions in units of radians (Kalluri et al., 2018). These describe the horizontal (x) and vertical (y) angles between a vector originating at the idealized optical center of the image to the sub-satellite point on the equator and the vector for the line of sight (LOS) to the center of a pixel (Figure 2.3). The standard method of reprojecting from the ABI Fixed Grid into geographic coordinates (i.e., latitude and longitude) is detailed in the GOES R Series Product Definition and User' Guide (NOAA, 2019). With the addition of a height above ellipsoid term to the Earth-centered distance calculation for a target ground point (Equation 2.2), goes_ortho performs this reprojection while correcting for the terrain parallax effect. For a detailed explanation of these methods, see Section 2.4.1 (Pestana & Lundquist, 2022).

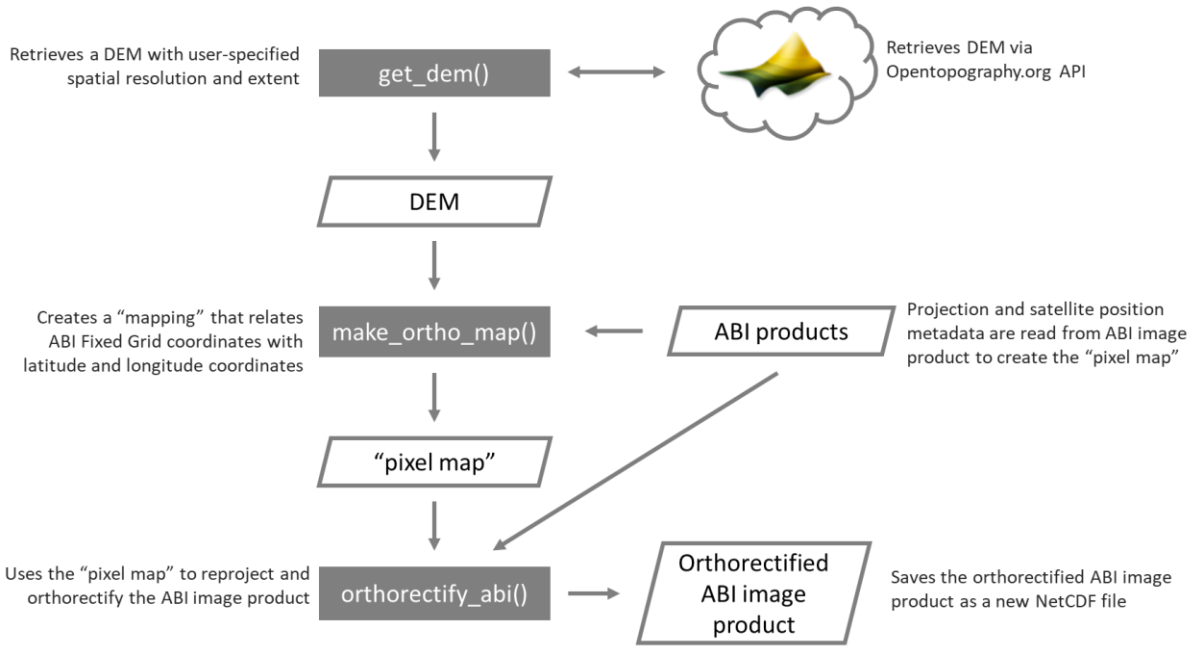

Figure 3.1. Flowchart illustrating the basic steps in orthorectifying GOES-R ABI images that are performed within the goes_ortho.ortho function. Subfunctions are illustrated with filled grey boxes, data are illustrated with outlined parallelograms.

3.2 Statement of need

The GOES-R series of geostationary-orbiting weather satellites provide a variety of image products derived from observations by the 16 spectral bands of the ABI. These image products have temporal resolutions of 5 minutes to 1 hour, and nominal spatial resolutions from 500 m to 2 km. However, the actual ground sample distance of individual ABI pixels increases from the sub-satellite point on the equator towards the edge of Earth's hemisphere visible to the satellite (e.g. from 2 km to > 6 km ground sample distance). These off-nadir view angles also mean that when image products are reprojected from image coordinates (e.g. ABI Fixed Grid) into geographic coordinates (e.g. WGS84 latitude and longitude), the apparent location of mountain terrain can be shifted from its true location. In extreme cases, some portions of the ground surface are completely obscured from view by surrounding steep terrain with poleward-facing aspects (north-facing aspects in the Northern Hemisphere, south-facing aspects in the

Southern Hemisphere). The standard ABI image products available are not corrected for terrain parallax. This precludes comparing ABI imagery to other terrain-corrected imagery and map products, as well as images from different GOES satellites (Figure 3.2). Therefore, to use ABI image products for land surface observations and analysis, especially in mountainous regions, the images must be corrected for this terrain parallax effect through orthorectification.

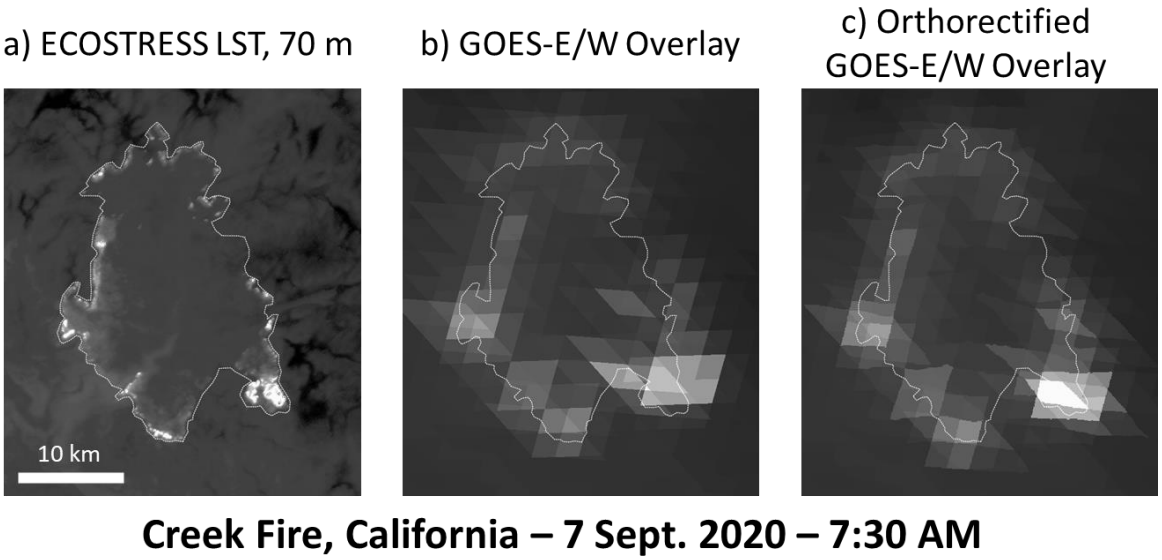

Figure 3.2. Orthorectifying GOES-East and GOES-West images to better define a fire perimeter. a) ECOSTRESS Land Surface Temperature image at 70 m spatial resolution from 7 September 2020 at 7:30 AM local time (UTC-8), with the perimeter of the Creek Fire manually delineated in white. Overlay of GOES-East and GOES-West ABI band 7 (3.9 μm) radiance images b) before orthorectifying, and c) after orthorectifying.

3.3 Other features of goes_ortho

In addition to computing terrain-corrected geographic coordinates for each pixel, goes_ortho has the flexibility to run at subpixel spatial resolutions. The spatial resolution is set by choosing a reference Digital Elevation Model (DEM) with the desired subpixel size. Each ABI pixel is then divided into subpixels of that size, and the terrain-corrected geographic coordinates are computed for those subpixels. This effectively drapes the coarser ABI pixels over

the terrain at the DEM's finer spatial resolution. The accuracy of the terrain correction will therefore depend on the true resolution of the reference DEM. The goes_ortho package retrieves DEMs via the OpenTopography.org API (Bhushan et al., 2022), but also allows for a user to provide their own DEM as a GeoTIFF.

Additional utility functions and scripts are included in the package, which aid in accessing, transforming, and analyzing GOES data. These include functions for converting between radiance, brightness temperature, and reflectance, or between radiance in wavenumber to radiance in wavelength, and creating timeseries for a single point within a stack of images. The download-goes.py script included is a wrapper around goespy (Mello & Pestana, 2022) to aid in downloading long timeseries of ABI images and is run in a command line.

3.4 Acknowledgements

I would like to thank the following individuals for their contributions to the development, and continued improvement, of goes_ortho: Shashank Bhushan, Jori Carter, Harry Dove-Robinson, Scott Henderson, Michelle Hu, Friedrich Knuth, Autumn Nguyen, Eli Schwat, and David Shean. This work uses data services provided by the OpenTopography Facility with support from the National Science Foundation under NSF Award Numbers 1948997, 1948994 & 1948857. Special thanks to Michelle Hu and Friedrich Knuth for their contributions to this chapter, and thank you to Mat Gunshor and Tim Schmit for providing the GOES-R ABI EQW data.

Chapter 4. Snow and forest temperature observations during the SnowEx 2020 Grand Mesa field campaign, and thermal infrared shadow-hiding in GOES-R ABI imagery

Steven Pestana[1], C. Chris Chickadel[1,2], Jessica D. Lundquist[1]

[1] Civil and Environmental Engineering, University of Washington, Seattle, WA, USA

[2] Applied Physics Laboratory, University of Washington, Seattle, WA, USA

4.1 Abstract

The high temporal resolution of thermal infrared imagery from the geostationary GOES-R satellites presents an opportunity to observe mountain snow and forest temperatures over the full diurnal cycle. However, the off-nadir views of these imagers may impact or bias surface temperature observations, especially when viewing a surface composed of both snow and forests. We used GOES-16 and -17 thermal infrared brightness temperature observations of a flat snow and forest-covered study site at Grand Mesa, Colorado, USA, to characterize how forest coverage and view angle impact these observations. Coincident ground-based and airborne IR observations collected as part of the NASA SnowEx field campaign in February 2020 provided a rich dataset for comparison. Observations over the course of two cloud-free days spanned the entire study site. The surface temperature observations from each dataset were compared to find their relative differences, and how those differences may have varied over time or as a function of varying forest cover across the study area. GOES-16 and -17 surface brightness temperatures were found to match the diurnal cycle and temperature range within ~1 hour and ± 3 °C of ground-based observations. GOES-16 and -17 were both biased warmer than nadir-looking airborne IR and ASTER observations. The warm biases were higher at times when the sun-satellite phase angle was near its daily minimum, and the warm biases seen in GOES-16 were greater for pixels that contained more forest coverage. The observations suggest that a "thermal infrared shadow-hiding" effect may be occurring, where the geostationary satellites are preferentially seeing the warmer sunlit sides of trees at different times of day. These biases are important to understand for applications using GOES-R ABI for surface temperatures over areas with surface roughness features, such as forests, that could exhibit a thermal infrared shadow-hiding effect.

4.2 Introduction

Mountain areas that receive seasonal snow are the headwaters of rivers that more than a billion people depend on globally (Immerzeel et al., 2020). Despite their importance, these are notoriously difficult places to gather hydrological or meteorological observations for predicting snow water equivalent (SWE) and the timing and magnitude of streamflow (Raleigh et al., 2013). Longwave radiation measurements, of which the upwards component is controlled by the diurnal cycle of snow surface temperature, has been identified as especially critical for modeling these snowmelt fed systems (Lapo et al., 2015; Raleigh et al., 2016). Distributed observations of surface temperatures at sub-daily temporal resolutions are needed for hydrologic and land surface models, and could aid real-time forecasting (Shamir & Georgakakos, 2014). Thermal infrared (TIR) imagery from geostationary satellites that constantly view the same portions of Earth's surface, such as GOES-R ABI, can make land surface temperature observations at very high temporal resolution (5 minutes or better), capturing the full diurnal cycle. These observations, however, have spatial resolutions of 2+ km, and view the land surface from off-nadir angles.

The 2020 NASA SnowEx field campaign was a collaborative effort between government agencies and academic researchers to intercompare and evaluate snow remote sensing methods with extensive ground-based observations. This was conducted in early 2020 at Grand Mesa, a large flat-topped mountain in the western part of the US state of Colorado. As part of this campaign, a multi-sensor experiment was designed to investigate how the off-nadir views of GOES-R satellites affect their surface temperature retrievals over snow and forests by making surface temperature observations and intercomparisons at a range of spatial and temporal scales (Figure 4.1). This unique study site, a flat expanse of snow and conifer forest, allowed us to

investigate how forests affect surface temperature observations, independent of the effects due to complex terrain. Ground-based snow surface temperature measurements provided a continuous point of comparison for GOES-R, while multiple overpasses from airborne IR imagery, gridded to 5 m spatial resolution, provided finer resolution distributed surface temperature details over the course of two mornings. To benchmark the ground point measurements and airborne IR, which itself has a wide range of view angles (Pestana et al., 2019), we compared these with a coincident nadir-looking ASTER TIR image at 90 m spatial resolution. Specifically, we set out to address the following questions regarding GOES-R ABI surface temperature observations during SnowEx:

1) What were the relative accuracies of each source of remotely sensed surface temperature?
2) How did fractional forest cover impact the relative accuracy of GOES-R ABI surface temperature across the study area?
3) How did the relative accuracy of GOES-R ABI surface temperature change over the course of each day of observations?

We hypothesized that among the surface temperature observations collected, the best agreements would be between the nadir-looking ASTER, nadir-looking Airborne IR, and ground-based snow surface temperatures. We further hypothesized that for GOES-R ABI pixels with greater forest canopy, the observed surface brightness temperatures would be greater than those from the nadir ASTER and Airborne IR imagery. Finally, we hypothesized that these warm biases would be greatest in the early morning observations by GOES-16 (East) and late afternoon observations by GOES-17 (West), when they are viewing the solar-illuminated side of trees.

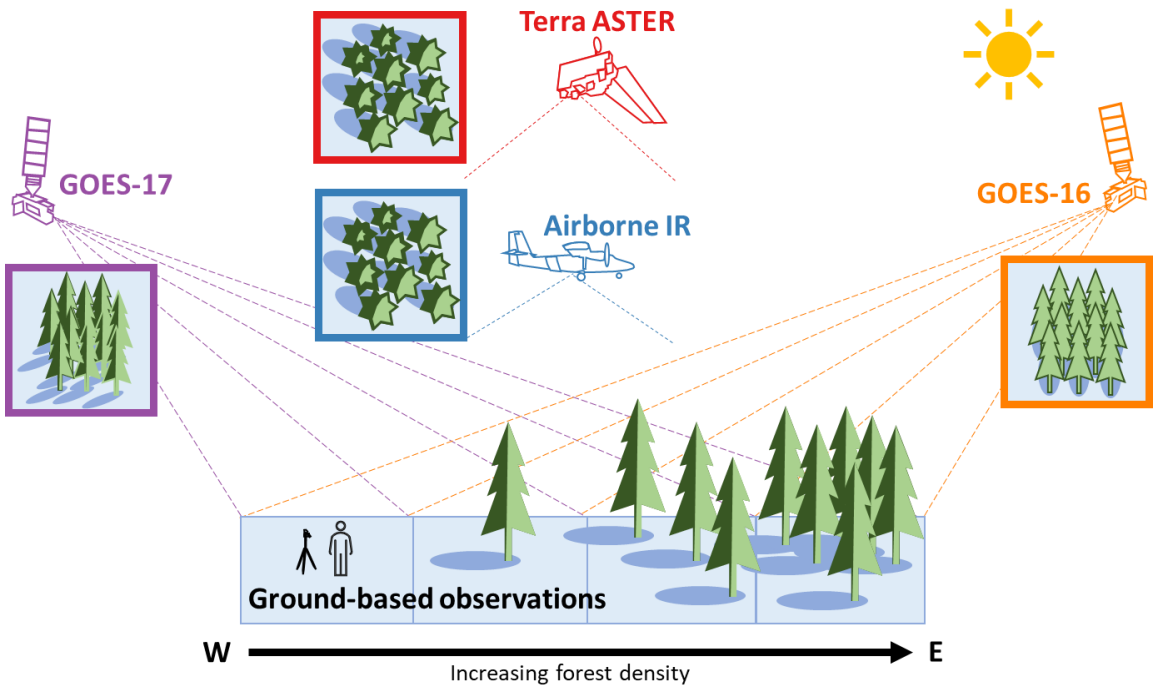

Figure 4.1. Conceptual illustration of how nadir and off-nadir looking remote sensing imagers see parts of a forest canopy and, depending on the direction of solar illumination, the shadows cast by trees.

4.2.1 High temporal resolution TIR imagery

Land surface models are highly sensitive to their temperature and longwave forcing input (Mizukami et al., 2014; Raleigh et al., 2015; Islam & Dery, 2016), in both accumulation and ablation periods (Gunther et al., 2019). This is especially important for sparsely instrumented mountain areas, where land surface models can have air temperature errors of ~3-4 °C (Tomasi et al., 2017). Differences in forcing inputs, or how surface energy fluxes are parameterized in land surface models, can result in hourly surface temperature errors as much as of 15 °C (Essery et al., 2013), and lead to snow disappearance date uncertainties spanning months (Hinkelman et al., 2015). Surface temperature observations at model-relevant time steps, such as hourly temporal resolutions, are needed especially to capture diurnal processes like snow melt-freeze cycles (Niu et al., 2011) and snow grain metamorphism, which in turn drive feedbacks in the surface energy

balance through changes in emissivity and albedo (Flanner & Zender, 2006; Warren, 1982, 2019).

Thermal infrared (TIR) satellite imagery can provide snow surface temperature observations for homogenous snow-covered landscapes (D. Hall et al., 2008; Z. Wan et al., 2002), estimates of near-surface air temperature (Pepin et al., 2016; Shamir & Georgakakos, 2014), and dewpoint temperature (Raleigh et al., 2013), all of which are needed for modeling hydrologic processes. However, satellite observations at <100 m spatial resolution are made too infrequently (4-16 day repeat) for looking at snow surface energy balance processes at model-relevant timesteps. Observations from imagers like VIIRS or MODIS (250 m to 1 km resolution) provide two observations per day each for mid-latitude locations. The observations from the sun-synchronous orbiting MODIS or VIIRS imagers do not necessarily see the coldest and warmest times of day to capture the full diurnal temperature range (DTR), nor do they provide land surface temperature (LST) more frequently than every several hours. Their twice daily observations can also be obscured by cloud cover, creating large data gaps relative to the diurnal cycle of snow surface temperatures.

Geostationary satellite imagery may help overcome these drawbacks, providing high temporal resolution surface temperature observations, potentially seeing between intermittent periods of cloud cover, though at coarser spatial resolutions (2+ km) and off-nadir view angles. In the complex terrain and forest vegetation of mountain watersheds, the individual image pixels from TIR observations will report a land surface temperature signature that is a mixture of the subpixel snow and forest surface temperatures (Dozier, 1981; Selkowitz et al., 2014). Snow and vegetation can have significant temperature differences, especially on clear days where incoming solar radiation warms forest canopies more than the high albedo snow surface and during the

snowmelt period, when daytime snow surface temperatures are capped at 0 °C (Pestana et al., 2019).

4.2.2 Off-nadir views and shadow-hiding

Imagery from geostationary satellites comes with the drawback of having off-nadir view angles, dependent on where the area of interest is located relative to the satellite's orbital position (Schmit et al., 2017). GOES-R views the mountains of North America from the south, and in the daytime, south-facing slopes receiving solar illumination heat up more than shaded north-facing slopes. Certain steep north-facing mountain slopes may be completely occluded from view. Prior work compared off-nadir GOES-16 TIR imagery to coincident nadir-looking ASTER and MODIS TIR imagery over the Sierra Nevada of California (Pestana & Lundquist, 2022). This work showed that GOES-16 imagery reported warmer brightness temperatures than ASTER and MODIS, which could see both the sunlit and shaded sides of mountain slopes.

At much smaller spatial scales, similar effects can occur with off-nadir daytime TIR observations of scenes containing forests. Solar illumination, especially at low sun angles, will warm up one side of individual trees or clusters of trees more than the other shaded side. These trees will also cast shadows onto the underlying snow surface, and the snow surface temperature in these shadows can be much colder than snow in sunlight (Figure 4.2). Therefore, depending on solar illumination and a satellite's view angle, the scene can either appear warmer (solar illuminated, shadows hidden) or colder (shaded areas in view) in comparison to nadir-looking imagery which sees both sides. Shadow-hiding occurs when the imager is viewing from the same direction that the sun is illuminating the scene, such that shadows cast by features such as trees are completely hidden from view (Bréon et al., 2002). This "hotspot" effect has been observed in visible and near-infrared (NIR) imagery over snow and forests (D. K. Hall et al., 1993), and over

snow with wind forms such as sastrugi (Warren et al., 1998). Analogous to the hotspot effect seen in reflected solar visible and NIR imagery, off-nadir thermal infrared imagery of snow and forests appears warmer than nadir-looking views. At off-nadir view angles, tree profiles come into view, obscuring the colder snow surface behind and beneath them (Balick et al., 2002; Pestana et al., 2019), and these patterns have been found to change as a function of the relative geometry between the sun and satellite in different seasons (Henderson et al., 2003). With remote sensing at very high temporal resolutions, we can expect to see this effect change over the course of the day as the sun traverses the sky, as different portions of the tree canopy are warmed in direct sunlight, and as tree shadows are cast onto the snow in different directions, creating cooler spots, sometimes hidden from the satellite's view.

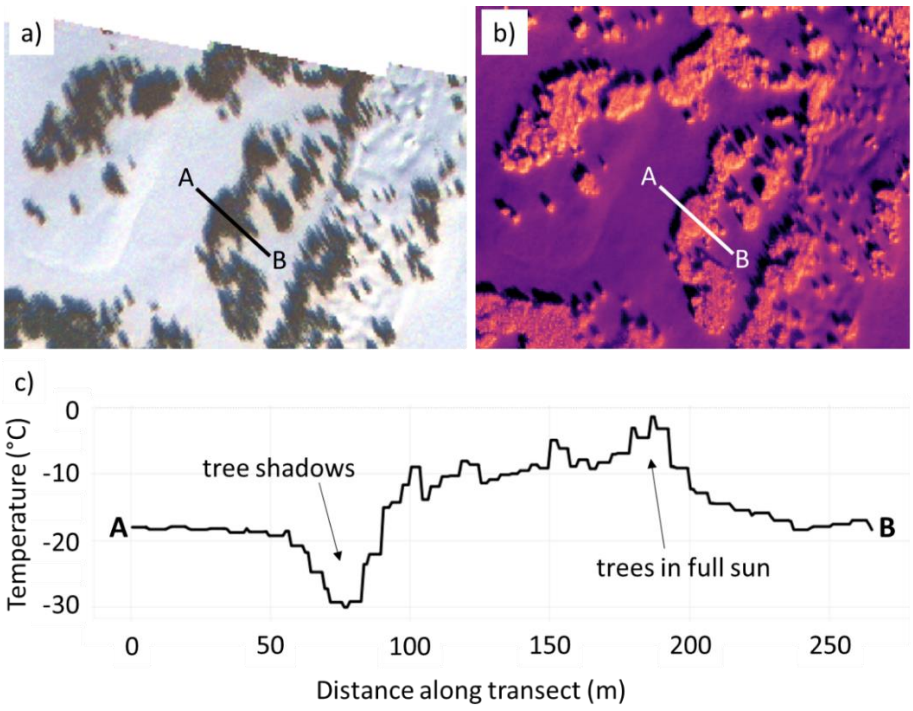

Figure 4.2. Approximately nadir airborne a) visible and b) IR images over Grand Mesa, Colorado from 2020-02-11 17:25:51 UTC, and c) a temperature profile across a forest stand, showing the presence of very cold tree shadows, and warm southeast forest edges in full sun. The temperature profile is parallel with the view direction of GOES-16, and nearly perpendicular to the view direction of GOES-17.

4.3 Study Site and Observations

4.3.1 SnowEx 2020 Field Campaign Study Site

The 2020 NASA SnowEx field campaign intensive observation period (IOP) took place at Grand Mesa in western Colorado (39.02°, -108.12°) from 26 January to 14 February 2020 (Figure 4.3). This period of the field campaign brought together snow remote sensing researchers to test new instruments and methods, and to collect extensive ground-based observations for validation. Grand Mesa, a large flat-topped mountain with elevations above 3000 m, is located within the watersheds of the upper Colorado river and its tributary, the Gunnison River. This region was chosen as a location to evaluate remote sensing observations of mountain snow because of its flat terrain, where the additional complications of view angles and complex terrain are minimized. The site is also beneficial for thermal infrared remote sensing because at its high elevation, the atmospheric path length, and therefore magnitude of absorption of thermal infrared radiation by water vapor in the atmosphere, is lower than that of sites at lower elevations. The high emissivities of both snow and conifer trees provide us with a scene where surface brightness temperatures are close to true surface temperatures (Kim et al., 2018; Warren, 2019).

During the IOP field campaign, the ground surface was entirely snow-covered, with no bare ground surfaces visible in remotely sensed imagery. The westernmost portion of Grand Mesa is sparsely forested, and forest cover increases across the mesa towards the east. Mixed conifer forests of Engelmann spruce (*Picea engelmannii*), subalpine fir (*Abies lasiocarpa*), and lodgepole pine *(Pinus contorta* var. *latifolia*) species dominates the vegetation that stood above the snow, with some stands of deciduous Aspen (*Populus tremuloides*) trees (Currier et al., 2019).

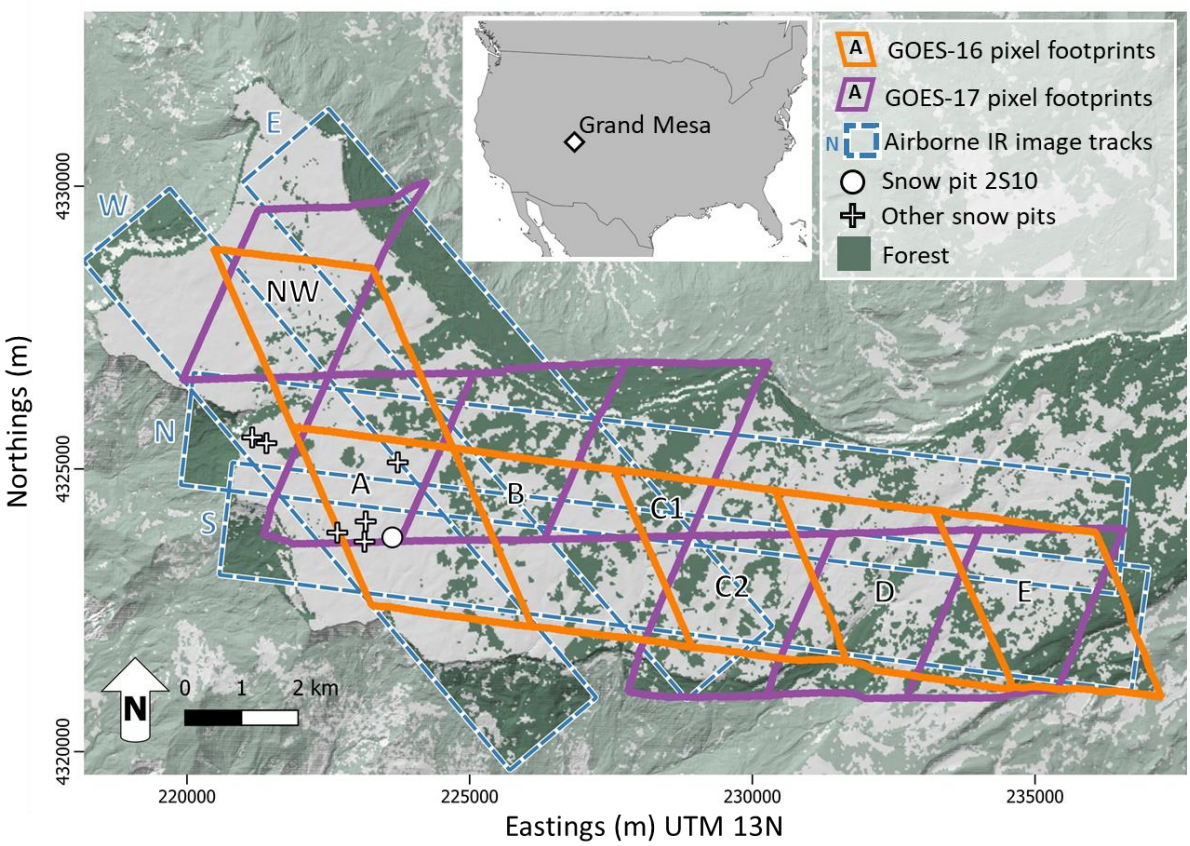

Figure 4.3. Map of the study area at Grand Mesa, Colorado, and inset map showing its location within the contiguous United States. Polygons outline GOES-16 (orange) and GOES-17 (purple) ABI pixel footprints, and airborne IR image mosaic swaths (blue dashed lines). Snow pit #2S10 where automated continuous snow surface temperatures were observed, is indicated by the white circle, and instantaneous snow surface temperature observations at other snow pits are indicated by white +'s. Dark green areas indicate forests within the area covered by the thermal infrared remote sensing imagery.

4.3.2 Ground-based Observations

Ground-based observations at Grand Mesa included continuous automated measurements of snow surface temperature, and instantaneous manual snow surface temperatures measurements taken as part of the data collection at individual snow pits. Snow surface temperatures were measured continuously by an Apogee SI-111 radiometer (8 – 14 μm) installed at snow pit #2S10 in the western portion of the mesa (39.0195, -108.19214). This radiometer viewed the snow surface at an angle of 45° from nadir and was mounted 2 m above the ground surface, which at

this time was 1.27 m above the snow surface. The radiometer had an instantaneous field of view of 44°, giving it an approximately elliptical footprint of 1.45 m x 2.45 m on the top of the snow surface. Snow surface temperatures measured by this radiometer were recorded at a 5-minute temporal resolution (Pestana & Lundquist, 2021). More than 150 snow pits were dug by the field teams over the course of the IOP (Vuyovich et al., 2021), and among the measurements recorded at each snow pit were snow surface temperature and the time of the surface temperature measurement. Snow surface temperatures were measured by a stem thermometer inserted into the top-most 1 cm of snow and shaded from direct sunlight. These snow pit data were accessed from the SnowEx database through the snowexsql Python library (Johnson et al., 2023). The USGS National Elevation Dataset 1 arc-second (~ 30 m) DEM (US Geologic Survey, 2017) and Tree Canopy Cover (TCC) product from the National Land Cover Database (NLCD) 2016 (Coulston et al., 2012) were used to compute zonal statistics of elevation and fractional vegetated area (f_{veg}), respectively, across the study site.

Table 4.1. Ground-based and remotely sensed surface temperature observations from the SnowEx 2020 field campaign used in this study.

	Dataset	Spatial resolution	Temporal resolution	Spectral range
Ground-based observations	Continuous snow surface temperature	1.5x2.5 m spot size	5 minute	8 – 14 μm
	Instantaneous snow surface temperature	n/a	n/a	n/a
Remote sensing observations.	Airborne IR image mosaics	5 m	~10 minute	8 – 14 μm
	ASTER IR image (AST L1T)	90 m	n/a (one image)	10.95 - 11.65 μm
	GOES-16 and -17 ABI band 13 (ABI-L1b-RadC)	~2km	5 minute	10.05 – 10.55 μm
	GOES-16 and -17 ABI band 14 (ABI-L1b-RadC)	~2 km	5 minute	10.8 – 11.6 μm
	GOES-16 and -17 ABI LST (ABI-L2-LSTC)	~2km	1 hour	n/a

4.3.3 Remote Sensing Observations

4.3.3.1 GOES-R ABI

Images from the Advanced Baseline Imager (ABI) onboard GOES-16 and GOES-17 were retrieved for the duration of the study period in February 2020. The 5-minute temporal resolution Level 1b Radiance CONUS product (L1b-RadC) for thermal infrared bands 13 (10.3 μm) and 14 (11.2 μm), and the 1-hour temporal resolution Level 2 Land Surface Temperature CONUS product (L2-LSTC), were downloaded as NetCDF files via the goespy library (Mello & Pestana, 2022). Both satellites viewed the Grand Mesa study site from similar view angles, though with GOES-16 in the southeastern sky (azimuth 134.1°, or 45.9° from due south) and GOES-17 in the southwestern sky (azimuth 221.2°, or 41.2° from due south), with elevation of angles of 33.5° and 35.9° respectively.

The specific ABI pixel footprints that overlapped the study area on top of Grand Mesa were identified by first orthorectifying (Pestana et al., 2022; Pestana & Lundquist, 2022) 2 km L1b-RadC imagery clipped to the region surrounding Grand Mesa from each of GOES-16 and GOES-17. Vector polygons outlining the ABI pixel footprints were created from these sample images, and the resulting polygons were then used to compute land surface elevation summary statistics from the 30 m resolution DEM (US Geologic Survey, 2017). We sampled ABI pixels with footprints on top of Grand Mesa that covered an area with a mean elevation greater than or equal to 3000 m and standard deviation of elevation less than or equal to 60 m. For GOES-16, this resulted in six pixels selected, and for GOES-17, seven pixels (Figure 4.3). The pairs of overlapping GOES-16 and -17 pixels were labeled “NW” for the pixels covering the northwestern most portion of Grand Mesa, and “A” – “E” for the pixels running roughly west to east across the study area. Two GOES-17 pixels are labeled “C1” and “C2” to indicate that they

both primarily overlapped with GOES-16 pixel "C." Timeseries of the thermal infrared radiance, brightness temperatures (both from L1b-RadC), and LST (from L2-LSTC) were compiled for each of these pixels from imagery covering 8 to 15 February 2020.

These pixel footprints were used to delineate areas of different fractional vegetation cover for comparison across the mesa. The NLCD TCC map was converted to a binary forest map with a vegetation threshold at 20% TCC. This threshold was chosen to visually match the forest above the snow surface in the ASTER visible image from the morning of 8 February (Figure 4.6a). For each GOES ABI pixel footprint, the fractional vegetation area (fveg) was calculated as the fraction of the pixel footprint classified as forest in the binary forest map.

Hourly LST observations were not available for most of the daytime periods. The ABI Cloud Mask algorithm is generally used to determine when and where the land surface is not obscured by clouds to determine if LST should be computed. However, identifying cloud cover over snow is notoriously difficult due to their similar appearance in remote sensed imagery across the visible through infrared spectrum (Rittger et al., 2019; Stillinger et al., 2019). Only four daytime LST observations on 8 February were available, and on 11 February there were three daytime and nine nighttime LST observations. Therefore, we focus primarily on radiance and brightness temperature in our analysis.

4.3.3.2 Airborne IR imagery

Airborne IR imagery was collected on four days with the UW Applied Physics Laboratory's Compact Airborne System for Imaging the Environment (CASIE), consisting of thermal infrared cameras and an infrared radiometer, mounted on the Twin Otter research aircraft from the Naval Postgraduate School (NPS) Center for Interdisciplinary Remotely Piloted Aircraft Studies (CIRPAS). CASIE was installed on the aircraft to be primarily nadir-looking, and had three DRS

UC640-17 TIR cameras (8 – 14 μm) pointing with bore-sight incidence angles of 19°, 0° (nadir-looking), and 21° from port to starboard on the aircraft. These three cameras have overlapping fields of view of 25° (left camera) and 40° (center and right cameras) perpendicular to the aircraft flight direction, with a total field of view of about 72.5° (Lundquist et al., 2018). The aircraft flew at about 1 km above the top of Grand Mesa, giving the three cameras a total swath width of about 2.5 km perpendicular to the direction of flight, and a raw ground resolution of 1 m. A nadir-looking Heitronics KT15.85D infrared radiometer with spectral range 9.6-11.5 um and narrow 1.9° field of view provides a precise brightness temperature measurement for a spot on the ground surface at the center of the center camera's field of view. This higher precision radiometer data was used to calibrate the TIR cameras (Pestana et al., 2019) prior to mosaicking images together using the aircraft INS-GPS navigation data from their original ~1.1 m spatial resolution to 5 m.

Flightlines over the study site were along two sets of parallel tracks that would overlap with ground observations at snow pits (Figure 4.3). One set of parallel tracks ran east-west, and the other tracks ran roughly northwest-southeast to capture the northwest portion of the mesa. The airborne IR imagery collection was in part planned to coincide with the collection of satellite imagery by ASTER on 8 February.

4.3.3.3 Terra ASTER

The NASA Terra satellite made an overpass of the Grand Mesa study site and imaged it with ASTER at 18:07 UTC (11:07 MST) on 8 February 2020. ASTER provides a reliable source of surface brightness temperature information at 90 m spatial resolution (Abrams, 2000), fine enough to capture the surface temperature variabilities across the Grand Mesa study area and resolve forest stands from open snow. We used the thermal infrared image of Grand Mesa AST

L1T product (Meyer et al., 2015) from band 14 (11.3 μm) converted from digital number to brightness temperature.

4.4 Methods

4.4.1 Evaluating airborne IR image mosaics against ASTER

To first assess the accuracy of the airborne IR imagery, two airborne IR mosaics from 8 February at 18:07 and 18:19 UTC (11:07 and 11:19 MST), running east-west across the mesa, were compared against the coincident ASTER image captured at 18:07 UTC (11:07 MST). The airborne IR mosaics were first resampled to the same spatial resolution of ASTER by taking the mean of the original 5 m spatial resolution images within each 90 m ASTER pixel. The differences between ASTER and each of the two resampled airborne IR mosaics were then computed, producing two difference maps, and the mean and standard deviation of differences were computed for each. Means and standard deviations of differences were also computed for the portions of the difference maps within each of the GOES-16 ABI pixel footprints. The difference maps were inspected qualitatively for patterns in the imagery across the study site to better characterize properties of the airborne IR imagery.

4.4.2 Comparison of airborne IR, ASTER and ground observations

To determine how representative the ground-based point temperature measurements were of their surrounding areas, airborne IR imagery and the single ASTER satellite image were compared with ground-based data at the times when each passed over the study site. From each Airborne IR mosaic, a 1 x 1 km square was extracted from around the automated snow surface temperature measurement site at snow pit #2S10 (Figure 4.4). Only airborne images that covered at least 30% of this 1 km^2 area were used. The mean, median, and standard deviation of surface

temperatures from this area in each airborne IR image were computed. This provided us with a timeseries of snow surface temperatures at each time that the aircraft flew over the ground site. The same 1 km^2 region around the snow surface temperature measurement site was sampled from the single ASTER image from the morning of 8 February to compute the surface temperature mean, median, and standard deviation as seen by ASTER. The correlation between the timeseries of Airborne IR snow temperature observations and ground-based snow surface temperatures were computed for each day, while the difference between the ground-based snow surface temperature measurements and ASTER observations were computed at the time of its overpass.

To compare the snow surface temperature observations taken at each snow pit against coincident airborne IR imagery, all of the snow pits sampled from 8 February and 11 February that were along the aircraft's flight path within +/- 30 minutes of the flight overpass were compared to the images from that flight. The mean and standard deviation of airborne IR observed surface temperatures within a 100 m^2 square centered on the snow pit were then compared with these ground-based observations to determine how the differences between the two varied over time and across the study area.

The sensitivity of the comparisons between airborne IR imagery, ASTER, and point ground-based surface temperature observations was tested by reducing the size of the square area from which temperatures were sampled from the airborne IR images (Figure 4.4), from a square with sides ranging from 1000 m to 100 m (a single ASTER pixel is 90 m), and then for the airborne imagery ranging from 1000 m to 5 m (the size of a single airborne IR pixel) (Table 4.). All airborne IR images were included in this analysis, rather than excluding images that covered less than 30% of the area, as was done in the prior analysis of airborne IR and ground data. The

mean, median, and standard deviation of surface temperatures were computed for the sampled region in each image. The mean difference, and root mean squared difference between all the airborne IR surface temperature observations of these areas and the coincident ground-based temperature measurements, were computed. The smallest area sampled was a single 5 m airborne IR pixel that should contain the ~2.5 m footprint of the ground-based radiometer that was measuring snow surface temperatures. However, the geolocation accuracy of the airborne IR mosaic imagery is only about +/- 10 m (Pestana et al., 2019). The single-pixel sampled therefore may not actually overlap completely with the ground-based radiometer footprint, but rather be directly adjacent to it.

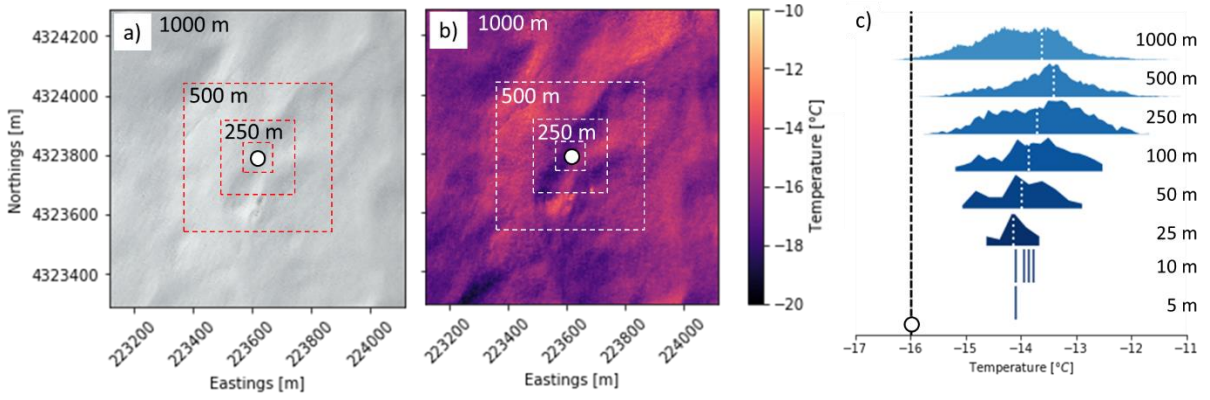

Figure 4.4. Airborne a) visible, and b) IR image of the area around the snow surface temperature observation site at snow pit #2S10. Boxes indicate regions from which the mean airborne IR surface temperature information was taken for comparison with the ground-based observations (only the boxes with sides of 1000, 500, 250, and 100 m are shown). Map coordinates are in UTM zone 13N. c) Histograms of the airborne IR surface temperatures from this example image plotted alongside the ground-based snow surface temperature at this time (vertical dashed line).

4.4.3 Comparison of high temporal resolution GOES-R ABI with continuous ground observations

GOES-16 and -17 brightness temperature observations were compared against the ground-based snow surface temperature observations at snow pit #2S10. A timeseries of brightness temperatures for bands 13 and 14 at 5-minute temporal resolution was created for 8 to 12

February 2020 for the GOES-16 and -17 ABI pixels, which contained snow pit #2S10 (both labeled pixel A). Two cloud-free periods, 8 February (1400 - 0100 UTC), and 11 February (0400 - 0100) were manually identified by inspecting the GOES imagery and brightness temperatures for cold cloud tops obscuring the study site. The ground-based snow surface temperature observations at snow pit #2S10 over these same time periods were resampled to match the 5-minute temporal resolution of GOES ABI brightness temperatures. All timeseries were then smoothed with a 30-minute running mean to remove the highest frequency variability (median < ± 0.02, $\sigma < 0.6$ °C) from the data and fill data gaps. The daily maximum and minimum temperatures and diurnal temperature range (DTR) were then found for both the ground-based snow surface temperature observations, and for the GOES ABI brightness temperatures. The mean and root mean squared difference between GOES ABI brightness temperatures and the ground-based snow and air temperatures were also computed. For 8 February, because there was cloud-cover at night obscuring the study area until 1400 UTC, we only compared the timing of maximum daytime temperature between GOES and the ground-based observations.

4.4.4 Comparison of GOES-R ABI, airborne IR, and ASTER imagery

The differences between GOES-16 and -17 ABI bands 14 and 13 brightness temperatures for 8 February (1400-0000 UTC) and 11 February (0400-0000 UTC) were computed for each pair of corresponding pixels (NW, A, B, C/C1, C/C2, D, and E) across the mesa. The mean difference, standard deviation of differences, and range of differences for each pixel were plotted against the corresponding pixel's f_{veg} value to inspect for any apparent correlation between these differences and the forest fraction within each pixel footprint. The comparison of GOES-16 to -17 is complicated because they view the scene from different perspectives. For example, the pair of pixels "A" from GOES-16 and -17 overlap each other, but they do not have the same footprint

on the ground, have slightly different values of f_{veg}, and may include different amounts of the edges of the mesa.

From each Airborne IR mosaic, if the airborne imagery covered at least 30% of each of the GOES-16 and -17 ABI pixel footprints on top of the mesa, the region was sampled from the mosaic (Figure 4.5). The mean, median and standard deviation of temperatures within each footprint were computed for comparison against the ABI band 14 brightness temperature and LST of that pixel for a 10-minute window around the aircraft overpass time. Similarly, the GOES-16 and -17 ABI pixel footprints were used to extract surface temperature mean and distributions from the single ASTER image for comparison against ABI band 14 brightness temperatures.

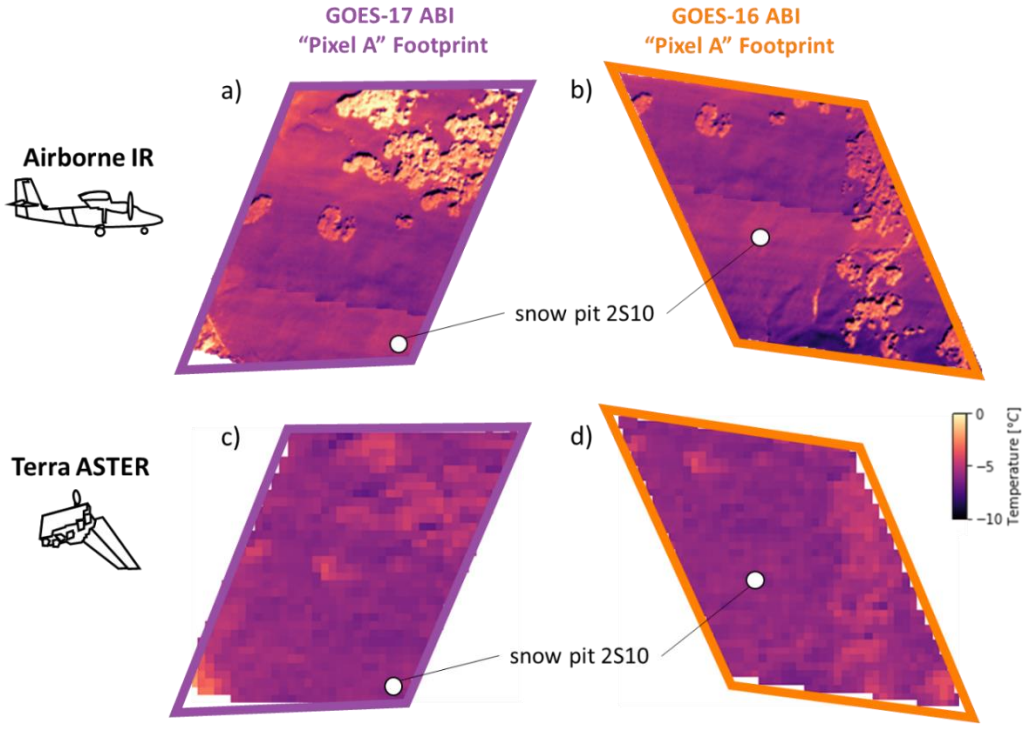

Figure 4.5. Example of sampling (a,b) 5 m spatial resolution airborne IR image mosaics and (c,d) 90 m spatial resolution ASTER image using the GOES-R ABI pixel footprints.

4.5 Results

4.5.1 Evaluating airborne IR image mosaics against ASTER

The airborne IR imagery was found to have a warm bias compared with ASTER brightness temperatures. The mean differences between the two resampled airborne IR image mosaics and the ASTER image from the morning of 8 February were 0.4 °C and 0.8 °C, and had standard deviations of 1.5 °C and 1.4 °C, respectively. Using the GOES-16 ABI pixel footprints labeled A-E, we found that the mean differences between the airborne IR and ASTER did not vary with vegetation cover.

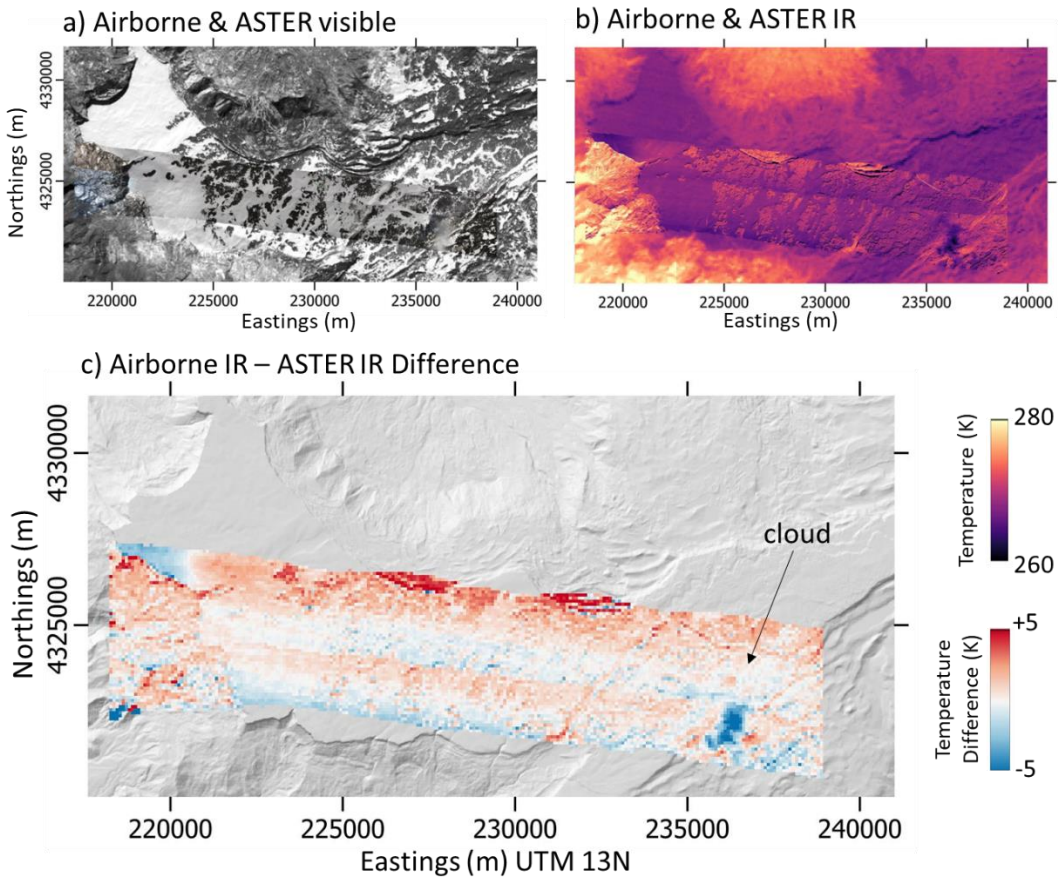

Figure 4.6. Comparison of airborne and ASTER a) visible and b) IR observations on the morning of 8 February 2020. c) The difference between airborne IR image mosaics (north flightline at 18:07 and south flightline at 18:19 UTC) and the ASTER image (at 18:07 UTC).

There were, however, systematic patterns in the difference between airborne IR and ASTER observed surface temperatures (Figure 4.6). These two airborne IR mosaics exhibited a temperature gradient across the field of view, with the southern edges of each image appearing approximately 1 °C colder than the northern edges, present only in imagery from flying the east-west flightlines. This gradient is most apparent across the relatively uniform open snow of the west side of the mesa. Though centered at nadir, the three airborne IR cameras together have view angles from 31.5° on the left to 41.0° on the right. At larger off-nadir view angles near the image edges more of the sides of trees will be visible (Pestana et al., 2019). On the aircraft's east-west flight across Grand Mesa, the north looking cameras are seeing the south-facing and sunlit side of trees and fewer tree shadows, while south looking cameras are seeing the north-facing side of trees and more snow surface shaded by the trees. This may explain some of the temperature gradient seen in the east-west flight images. Lastly, the easternmost portion of the airborne IR mosaic from 18:19:15 UTC shows a large cold feature, which, by inspecting the visible airborne imagery, we identified as a small cloud, not visible in the airborne or ASTER image from 12 minutes prior.

4.5.2 Comparison of airborne IR, ASTER and ground observations

Snow surface temperatures observed by the airborne IR and ASTER imagers were biased warm in comparison with the ground-based snow surface temperature observations at snow pit #2S10. Aircraft flights on two cloud-free days during the study period provided us with 15 overpasses over the ground sites on the western mesa. Two flights were made on 8 February (Figure 4.7a,b). On the first flight, three overpasses occurred about an hour after sunrise (1413 UTC, 0713 MST) between 1500 and 1630 UTC. The second flight of that day made six overpasses between 1730 and 2000 UTC. The second flight was coincident with the ASTER

image taken at about 1808 UTC. On 11 February, a single flight made another six overpasses of the ground site between 1630 and 2000 UTC (Figure 4.7c,d).

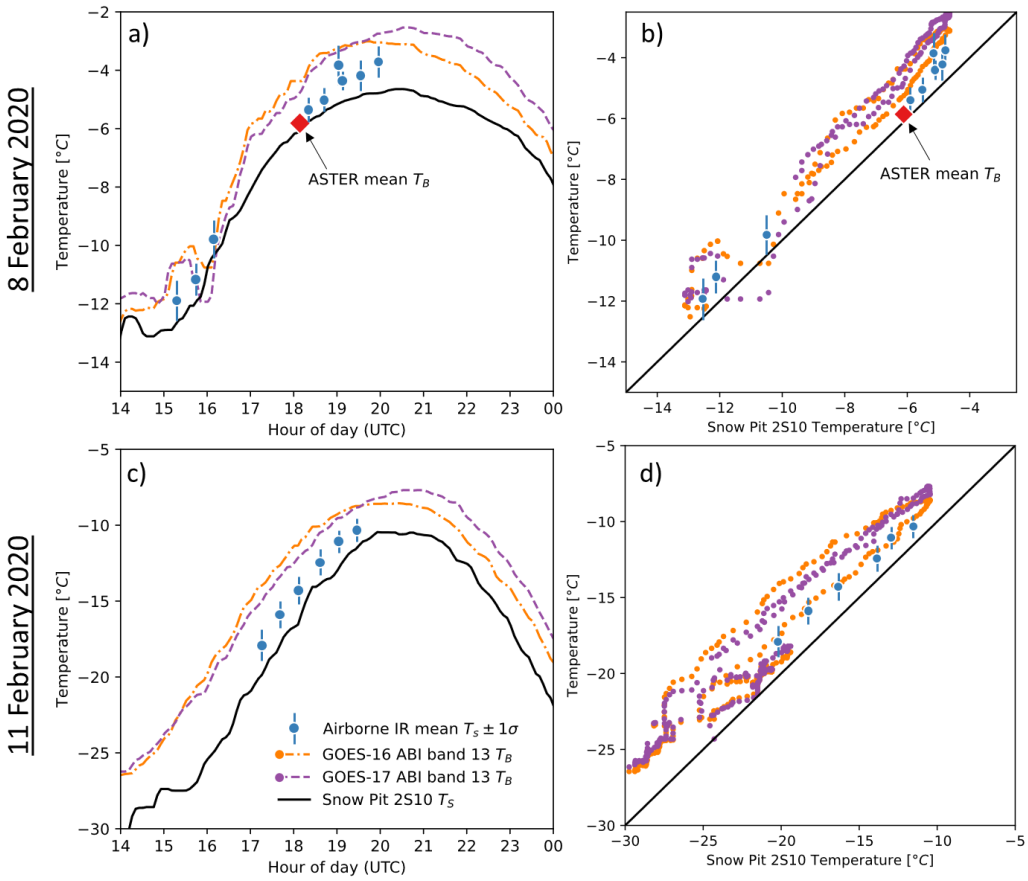

Figure 4.7. Timeseries for a) 8 Feb. and c) 11 Feb. of the ground-based snow surface temperatures from the Apogee radiometer at snow pit #2S10 (black line), along with GOES-16 (dashed orange) and GOES-17 (dashed purple) band 13 brightness temperatures, airborne IR (blue circles), and ASTER (red diamonds) mean brightness temperatures for the 1 km^2 area around the ground site. Plots of ground-based snow surface temperature against remote sensing brightness temperatures on b) 8 Feb. and d) 11 Feb.

On 8 Feb., snow surface temperatures as seen by the airborne IR and ASTER imagery appeared more uniform than on 11 Feb. around snow pit #2S10, and therefore less sensitive to the size of the area sampled from the imagery to compare with ground-based observations (Table 4.4). ASTER on 8 February matched most closely to the ground-based surface temperatures with its single pixel value, though this difference only increased by ~ 0.3 °C as the size of the sampled

region increased. Snow surface temperatures as seen in the airborne IR imagery were more uniform across the study area on 8 February (with standard deviations across the 1 km^2 area of 0.2 to 0.6 °C) than on 11 February (with standard deviations of 0.7 to 1.0 °C).

Table 4.2. Mean difference between ground-based snow surface temperatures and surface temperatures from both ASTER and airborne IR imagery, sampled from square areas with sides of 1000 to 5 m.

Box size of image area sampled (m)	**Mean Difference with Ground-based Ts at Snow Pit 2S10**		
	ASTER, 8 Feb.	**Airborne IR, 8 Feb.**	**Airborne IR, 11 Feb.**
1000	0.3	0.6	2.0
500	0.3	0.9	2.3
250	0.1	0.9	2.0
100	0.0	0.9	1.8
50	-	0.9	1.7
25	-	0.9	1.5
10	-	0.9	1.6
5	-	1.0	1.4

Only three snow pits on 8 February, and two snow pits on 11 February were captured in the airborne IR imagery within +/-30 minutes of their snow surface temperature measurements. On the 8th, two of the snow pit surface temperature measurements were within +/- 1 °C of the airborne IR image, one was ~2 °C warmer, and on the 11 February, both snow pit temperature observations were 3 – 4 °C warmer than the temperatures in the airborne IR images. Measuring the temperature of the top-most centimeter of snow is not trivial, as the stem thermometers used are in contact with snow grains and the air space between snow grains. Near the top of the snowpack, the air temperature can be close to that of the above-surface air (Colbeck, 1989), potentially biasing these snow surface temperature readings more towards that of warmer ambient air temperatures.

Table 4.3. Summary of mean differences between the various surface temperature data sources (aggregated across all ABI pixel footprints where applicable) for two days of coincident

observations during the SnowEx 2020 field campaign. Cells are colored by sign and magnitude of the difference, with positive differences in red and negative differences in blue.

	Ground Ts	Airborne IR Ts	ASTER Tb	GOES-17 b13 Tb	GOES-17 b14 Tb	GOES-16 b13 Tb	GOES-16 b14 Tb
Ground Ts		0.8	0.3	1.6	1.2	1.3	1
Airborne IR Ts	1.8		0.6	0.3	0	1.1	0.9
ASTER Tb	-	-		2.2	0.6	2.6	1.2
GOES-17 b13 Tb	2.9	1.7	-		-0.3	0.1	0.3
GOES-17 b14 Tb	2.7	1.6	-	-0.2		-0.2	0
GOES-16 b13 Tb	2.7	3.4	-	0.3	0.1		-0.2
GOES-16 b14 Tb	2.4	3.5	-	0.5	0.3	0	

11 February 2020
(difference = row – column)

8 February 2020
(difference = column – row)

4.5.3 Comparison of high temporal resolution GOES-R ABI with continuous ground observations

Both GOES-16 and -17 reported surface brightness temperatures warmer than the ground-based snow surface temperature observations (Figure 4.7), though this difference varied over the course of each day (Figure 4.8). Compared to the ground-based observations, the band 14 brightness temperatures had smaller mean and root-mean-squared differences than did the band 13 brightness temperatures. ABI brightness temperatures and ground-based temperature observations show a hysteresis patterns, with GOES ABI brightness temperatures more closely matching the ground-based observations in the nighttime (11 Feb.) and early morning (8 Feb.) than during the day. This pattern is more apparent on 11 Feb., with GOES brightness temperatures warming up in the morning, and cooling down in the evening, faster than the ground-based snow surface temperatures.

GOES-16 and -17, bands 13 and 14, all observed daily T_{min} and T_{max} within 1 hour or less of those measured on the ground, and the DTR matched within +/- 3 °C on both days. On 8 February, GOES-16 and -17, bands 13 and 14, all observed T_{max} within 30 minutes of ground-based T_{max}. Both GOES-16 and -17 observed a DTR ~3° C larger in this time period than the DTR measured on the ground. On 11 February, GOES-16 bands 13 and 14 observed the time of T_{max} 30 minutes later than the ground-based T_{max}, and T_{min} within 15 minutes. GOES-17 saw T_{max} almost 1 hour later than ground-based T_{max}, and a T_{min} within 20 minutes of ground-based T_{min}. On this day, the DTR observed by GOES ABI was ~3° C smaller than the DTR from the ground-based snow surface temperature observations.

4.5.4 Comparison of GOES-R ABI, airborne IR, and ASTER imagery

The surface brightness temperatures from both GOES-16 and -17 were warmer than those from airborne IR and ASTER imagery, and this warm bias was larger for GOES-16, especially for ABI pixels which contained larger forest fractions. The mean differences between GOES-16 and -17 and airborne IR observations across all pixels during the first flight on 8 February decreased over time from a positive to a negative biases (Figure 4.8a,b). During the second flight, the mean differences between GOES-16 and airborne IR generally decreased from about 2 °C to 0 °C, while the mean differences between GOES-17 and airborne IR increased over time from -1 °C to 1 °C. On 11 February, the mean differences between GOES-17 and airborne IR were relatively constant throughout the morning of observations, while GOES-16 mean differences decreased similarly to what was seen on 8 February, from 5 °C to 2 °C (Figure 4.8c,d). The mean differences between GOES-16 and airborne IR were found to be larger for ABI pixel footprints with higher f_{veg}, while the differences with GOES-17 did not correlate with

f_{veg} (Figure 4.9). Similarly, the mean differences between GOES-16, but not GOES-17, and ASTER were larger for ABI pixel footprints with larger f_{veg}.

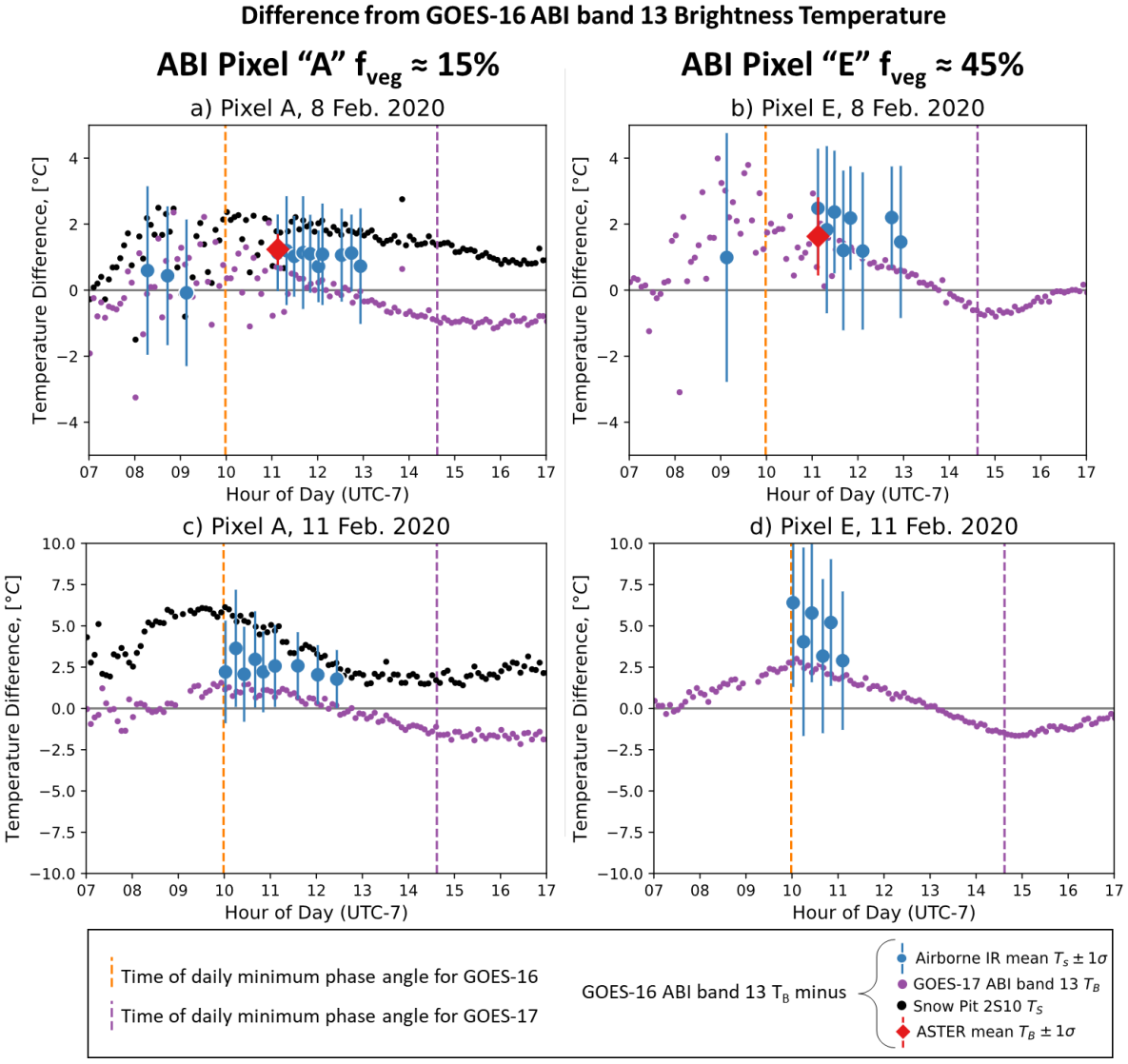

Figure 4.8. Difference between GOES-16 ABI band 13 brightness temperature, and surface temperature observations from GOES-17 ABI band 13, airborne IR imagery, ASTER imagery, and ground-based observations. Plots for (a,b) 8 February 2020 and (c,d) 11 Februrary 2020 for pixels (a,c) A (fveg~15%) and (b,d) E (fveg~45%). The times that GOES-16 and GOES-17 have their daily minimum phase angle are marked with vertical dashed orange and purple lines, respectively.

The difference between GOES-16 and -17 brightness temperatures showed a prominent pattern over the course of each day, with GOES-16 reporting warmer brightness temperatures by

as much as 3 °C in the morning, peaking at about 1700 UTC, and GOES-17 reporting warmer brightness temperatures by nearly 3 °C in the afternoons, peaking at about 2200 UTC. The maximum and minimum differences between GOES-16 and -17 were larger for the more forested pixel E than the mostly open snow pixel A. However, there was no correlation found between these differences and the f_{veg} value of each pixel.

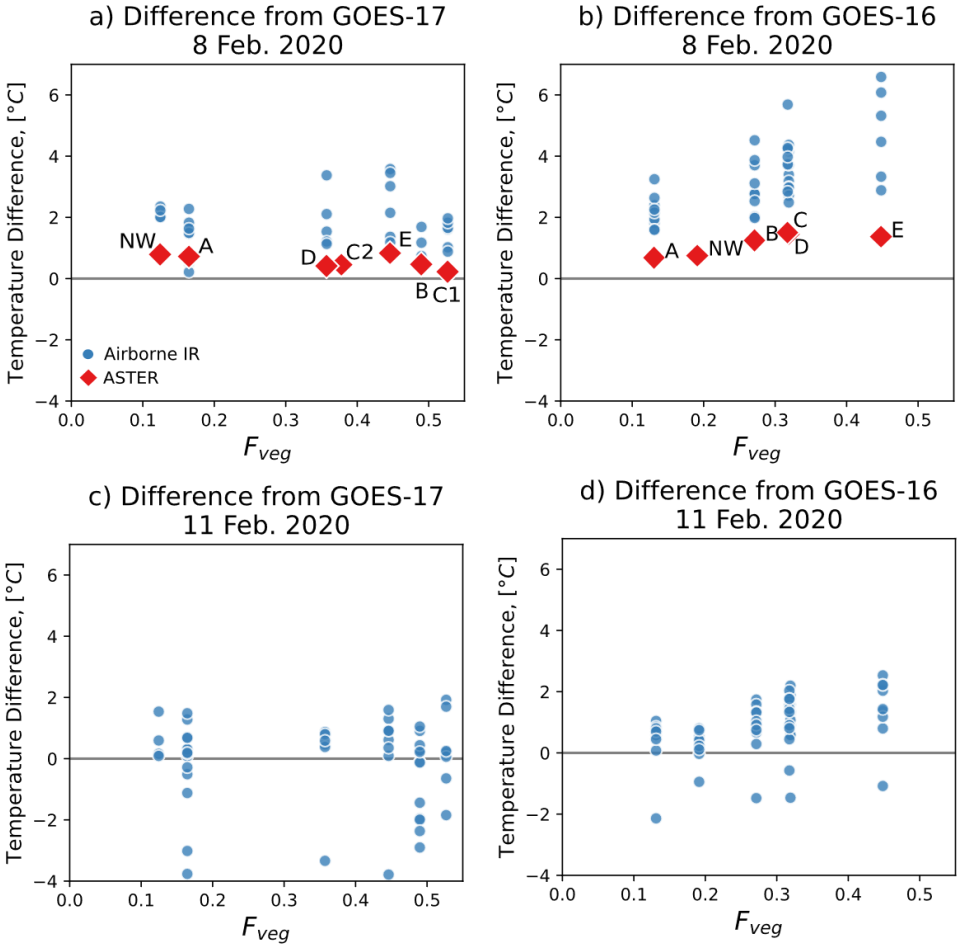

Figure 4.9. Mean differences between GOES-16 and -17 ABI brightness temperatures, airborne IR (blue dots) and ASTER (red diamonds), plotted against the fractional vegetated area (f_{veg}) value of each ABI pixel footprint.

4.6 Discussion

4.6.1 Intercomparison of remote sensing data

The mean differences between surface temperatures observed by all remote sensing sources and ground-based observations ranged from about 0 to 5 °C, with remote sensing sources (airborne IR, ASTER, GOES ABI) typically reporting warmer surface temperatures than those measured on the ground. The airborne IR and ASTER images best matched the ground-based snow surface temperature observations because they could resolve separate snow and forest temperatures, whereas the coarser 2+ km spatial resolution GOES-R ABI pixels reported a mixture of forest and snow temperatures (Table 4.). This was apparent even for the mostly forest-free westernmost portion of Grand Mesa (pixels A) with f_{veg}≈15%. Additionally, there were some thin high-altitude clouds on the morning of 8 February, visible in the GOES-R ABI near-infrared "cirrus band" (band 4, 1.37 μm). The timeseries of band 13 and 14 brightness temperatures during this time show rapid changes, and possibly colder temperatures than would be reported if those thin clouds had not been present.

Over the course of each morning, the airborne IR imagery tracked the morning warm-up of the snow surface closely, with a constant warm bias relative to the ground-based observations (Figure 4.7). GOES-16 and -17 ABI also tracked the ground-based snow surface temperature observations over the course of the day, though their biases relative to those observations changed over time (Figure 4.8). Snow surface temperatures were more uniform across the western mesa on 8 February than on 11 February, as seen in airborne imagery (Table 4.). This was also reflected in ABI brightness temperatures more closely matching the ground-based observations on 8 February. Both GOES-16 and -17 captured the timing of daily T_{min} and T_{max} on these two days within ~1 hour, and the diurnal temperature range within +/- 3 °C. This

uncertainty in the DTR is similar to the range seen in the mean differences over each day and across the mesa between GOES-R ABI and the ground-based observations (1-3 °C), ABI and ASTER (2 – 3 °C), and ABI and the airborne IR imagery (0 – 5 °C).

Our use of a ground-based infrared radiometer, and thermal infrared imagers all within the 8-14 μm window allowed us to directly compare their observed brightness temperatures rather than derived LST products. The thermal infrared brightness temperatures observed by ABI are likely to be colder than the actual surface brightness temperature due to atmospheric absorption of infrared radiation. At our high elevation study site, the atmospheric path is shorter, and atmospheric water vapor concentrations are less than those at lower elevations. However, we could still expect brightness temperatures to appear nearly 4 °C colder than true surface brightness temperatures for these GOES-R ABI observations (Berk et al., 2014). The GOES-R ABI LST product, which is designed to account for these atmospheric effects, reported surface temperatures about 3-4 °C warmer than the ground-based observations of brightness temperatures. Absorption by water vapor along the atmospheric path between the snow surface and the radiometer mounted < 2 m above the snow surface is negligible; however for the airborne IR observations with a path length of ~1 km, this could result in brightness temperatures nearly 2 °C colder than true surface brightness temperatures. Due to the difference in atmospheric path length alone we would expect satellite observations of top of atmosphere brightness temperature to be biased colder than airborne observations from ~1 km. However, our results instead show GOES-R ABI brightness temperatures biased warmer than airborne observations, suggesting that the magnitude of the atmospheric effect is surpassed by view angle related effects.

The mean differences between ground-based snow surface temperature observations and ABI band 14 brightness temperatures were smaller than those for band 13 by about 0.2-0.4 °C. This, however, doesn't necessarily mean that band 14 was providing a more accurate snow surface temperature reading. Band 14 covers wavelengths where we can expect some absorption of infrared radiance by atmospheric water vapor, whereas band 13 sits within the "clean IR" window with minimal to no IR absorption by water vapor (Schmit et al., 2018). With no atmospheric water vapor absorption, the difference between band 13 and 14 brightness temperatures would be negligible. Any atmospheric water vapor present can result in band 14 brightness temperatures being colder than band 13, as was the case seen here. Though we chose cloud-free time periods of observations, any trace amounts of water vapor could be causing band 14 to appear colder, and which coincidentally more closely matched snow surface temperatures on Grand Mesa.

4.6.2 Sun-satellite phase angle and thermal infrared shadow-hiding

Even with the flat terrain of Grand Mesa controlling for effects of viewing mountain terrain from off-nadir angles (Pestana & Lundquist, 2022), we observed a morning warm bias between GOES-16 and the coincident nadir-looking ASTER, airborne IR imagery, and GOES-17 (Figure 4.8). The GOES-16 brightness temperatures were potentially exhibiting a hotspot effect when the angle between the sun and the view angle of GOES-16 (phase angle) reached a daily minimum. The hotspot effect seen in remote sensing imagery of forests is understood to be explained by shadow-hiding in imagery of reflected sunlight in the visible and NIR wavelengths (Deering et al., 1999; Hapke et al., 1996).

When the airborne IR and ASTER images were taken (1400-2000 UTC), the sun was rising in the southeastern sky, in the same direction from which GOES-16 was viewing Grand Mesa.

At about 1700 UTC on 11 February, when we see the largest warm biases between GOES-16 and all other datasets, the sun had reached 26.9 degrees elevation at an azimuth of 139.1 degrees (26.1 and 139.6 on the 8th). The angle between GOES-16's view and the sun's position (phase angle) was at its minimum of ~ 8 degrees on 11 February at 1659 UTC (~9 degrees at the same time on 8 February). At this time, the sun was illuminating and warming the southeastern facing sides of trees that GOES-16 is viewing, which in the airborne IR imagery were as much as 5 °C warmer than the shaded side of trees (Figure 4.2). In addition to viewing the sunlit side of trees, snow in tree shadows was considerably colder than snow in the sunlight (by ~10 °C) and would also be hidden from the view of GOES-16.

The airborne IR and ASTER images viewed the study area from nadir, and the difference between these two image sources did not vary with f_{veg}. GOES-17 surface brightness temperatures had smaller mean differences compared to airborne and ASTER than GOES-16, and these differences did not correlate with f_{veg}. GOES-17, viewing Grand Mesa from the southwest, would similarly be viewing the southwest facing sides of trees, though during the morning these would be partially in sun and partially in shade. In the afternoon we see that GOES-17 is warmer than GOES-16, peaking at about 2200 UTC. The minimum phase angle between the sun and GOES 17 is ~8 degrees at 2137 UTC on 11 February (~9 degrees on 8 Feb.).

Though we see that the warm bias in GOES-16 imagery correlates with f_{veg}, the presence of these same warm biases and their patterns over time (e.g. warm biases peaking at the time of minimum phase angle) in the mostly open snow pixels (Figure 4.8, A) suggests that other sources of surface roughness may also be contributing to this effect, such as greater than meter-scale dunes, or sub-meter-scale ripples and sastrugi (Kochanski et al., 2019; Warren et al., 1998).

4.6.3 Applications for downscaling GOES-R ABI thermal infrared imagery

Downscaling methods for coarse spatial resolution thermal infrared imagery rely on finer spatial resolution maps of land cover properties and statistical relationships to model and therefore correct for the expected biases in the coarse imagery. Prior methods have used vegetation (Inamdar & French, 2009; Kustas et al., 2003) and terrain maps (Walters, 2013), and biases in GOES-16 ABI imagery have been related to their off-nadir views of complex terrain (Pestana & Lundquist, 2022). Our results demonstrate that for high temporal resolution GOES-R ABI thermal infrared imagery, not only does the fractional forest coverage of each ABI pixel have some control on surface temperature biases, but so does the solar illumination angle, and the phase angle between the satellite and sun. Thus, any downscaling of GOES-R data must explicitly consider time of day and time of year. These solar and satellite view angle controls on surface temperature observation biases were observed at both the forested and open snow regions of Grand Mesa, suggesting that surface roughness features as large as trees but perhaps as small as sastrugi contributed to the hotspot effect seen. This information will be needed to determine if, when, and what magnitude a hotspot or thermal infrared shadow-hiding effect will have on the surface temperature bias of the coarser resolution GOES-R ABI.

4.7 Conclusions

During the NASA SnowEx field campaign in February 2020, we conducted an intercomparison of thermal infrared remote sensors for retrieving surface brightness temperatures of snow and forests. The flat study site at Grand Mesa in western Colorado, USA, allowed us to investigate the impact that forest cover has on thermal infrared remote sensing from GOES-16 and GOES-17 at off-nadir view angles and high temporal resolution. Snow surface temperatures observed by the airborne IR and ASTER imagers were biased warm in comparison with the

ground-based snow surface temperature observations, and the airborne IR imagery itself was found to have a warm bias compared with ASTER, all with mean differences within < 1 °C of each other. GOES-16 and GOES-17 observed daily maximum and minimum brightness temperatures within ~1 hour of those measured in situ, and the diurnal temperature range within +/- 3 °C. GOES-16 and GOES-17 reported warmer surface brightness temperatures than the ground-based, airborne IR, and ASTER observations. This warm bias was larger for GOES-16 in the mornings when the aircraft and ASTER passed over the study site. The maximum warm biases in GOES-16 and GOES-17 occurred when the sun-satellite phase angle was at its daily minimum, suggesting that a thermal infrared shadow-hiding effect may cause these off-nadir imagers to sense warmer temperatures than nadir-looking imagers.

The thermal infrared imagery and ground-based snow surface temperature observations collected as part of SnowEx 2020 provide a unique dataset for characterizing the high temporal resolution observations from geostationary satellites. It could be used further for testing methods for spatially downscaling coarse GOES-R ABI imagery of snow and forests to finer spatial resolutions with statistical models, sensor fusion methods (Quan et al., 2018; Weng & Fu, 2014), or using spectral mixture models to separate snow and forest temperatures (Lundquist et al., 2018). Though this work focuses on a single site in a short time period, other geostationary satellites comparable to GOES-R ABI, such as Fengyun-4 and Himawari-8, provide similar views of High Mountain Asia and other mountains in the Eastern hemisphere where these observations are needed. We expect the processes described here to be important for interpreting geostationary thermal IR observations all around the globe.

4.8 Acknowledgements

We would like to thank the SnowEx 2020 organizing team, participants, snowmobile guides, National Snow and Ice Data Center staff, and the Naval Postgraduate School pilots for facilitating the data collection, and the SWESARR team for accommodating our work and providing IMU/GPS navigation data. We would also like to thank fellow project team members from SnowEx Hackweek 2021 for their work developing workflows and tools to analyze the SnowEx snow temperature observations: Aji John, Jeremy Johnston, Friedrich Knuth, Jewell Lund, Giulia Mazzotti, Zachary Miller, Wenge Ni-Meister, Dillon Ragar. Thank you to the University of Washington Mountain Hydrology group for feedback and input throughout this project. This work was funded by NASA FINESST grant 80NSSC20K1610 and NASA grant 80NSSC20K0374.

Chapter 5. Observations of diurnal midwave infrared anisotropy over snow and forests with GOES-R ABI

Steven Pestana1, Edward H. Bair2, Jeff Dozier3, Jessica D. Lundquist1

[1]Civil and Environmental Engineering, University of Washington, Seattle, WA, USA

[2]Earth Research Institute, University of California, Santa Barbara, CA USA

[3]Bren School of Environmental Science and Management, University of California, Santa Barbara, CA USA

5.1 Abstract

A primary challenge of remote sensing surface temperatures with infrared imagery is the coarse spatial resolution of imagery relative to the size of features of interest. This results in pixels reporting a mixture of temperatures from subpixel-sized surface features. Infrared spectral separation methods can help resolve subpixel surface temperatures with the use of simultaneous observations in the thermal infrared (TIR), wavelengths within the infrared window around 10 μm, and midwave infrared (MWIR) wavelengths around 4 μm. However, MWIR has both significant reflected and emitted components, and there is an unaddressed question of how to treat this reflected component in infrared spectral separation methods. Current methods must either estimate or attempt to solve for reflected MWIR. Adding another unknown further complicates infrared spectral separation problems, and the MWIR reflectivity of natural surfaces land surfaces has not been fully investigated. Accurate representation of reflected MWIR is especially important for high temporal resolution, off-nadir-looking GOES-R ABI imagery, where the solar illumination angle changes over the course of the day. We investigated the effects of view angle, solar illumination angle, and forest cover to better understand the anisotropic MWIR signals observed at high temporal resolution for snow and forest scenes. We used wintertime observations from Grand Mesa, Colorado, USA to investigate how MWIR radiance varied with the sun-satellite phase angle and forest coverage, and propose next steps for incorporating MWIR anisotropy into spectral separation methods.

5.2 Introduction

Applications of remote sensing of Earth's surface in the midwave infrared (MWIR) wavelengths (~4 μm) include observations of land surface temperatures and high temperature features such as wildfires (Cawse-Nicholson et al., 2021; Weaver et al., 2004), and volcanos

(Francis & Rothery, 2000). MWIR has also found use in infrared spectral separation techniques that retrieve subpixel surface temperatures from mixed pixels to detect features such as small fires (Dozier, 1981; Giglio & Kendall, 2001) or for separating snow and forest temperatures (Lundquist et al., 2018).The outgoing radiance from a mixed pixel containing two or more subpixel-sized surfaces at different temperatures can be modeled as a weighted linear combination of the radiance from each endmember. Emissions from a warmer subpixel surface will be shifted towards shorter wavelengths more than those from a colder surface. Infrared spectral separation techniques use observations in the midwave (~4 μm) and thermal infrared (~10 μm) wavelengths to solve for these separate subpixel temperatures.

Complicating these applications in the daytime, a portion of MWIR radiance detected by satellite remote sensing will be solar radiation reflected by the surface. For GOES-R Advanced Baseline Imager (ABI) band 7, centered at 3.9 μm, as much as 10-20% of the detected radiance in the daytime can be from reflected solar, with the remainder being emitted from the surface. Reflected solar MWIR is the product of the incoming solar radiation times the surface reflectance at these wavelengths, whereas the emitted MWIR radiance is a function of the surface temperature and emissivity. By Kirchhoff's Law, at a given wavelength and angle, emissivity and reflectance must sum to one for opaque surfaces such as snowpack or vegetation (Dozier & Warren, 1982).

Reflected MWIR can be estimated with computations of clear-sky radiance, though this requires assumptions about the reflectance characteristics of the surface. For improving the MODIS fire detection algorithm, He and Li (2011) considered land surfaces to be Lambertian reflectors. Lundquist et al. (Lundquist et al., 2018), in separating forest and snow temperature using MODIS, estimated the reflected component of MWIR from snow with the Dozier-Warren

model of Mie scattering (Dozier & Warren, 1982), and assumed vegetation to be a Lambertian reflector.

Apart from the reflectance of individual surface materials, rough surfaces can exhibit other reflectance properties, such as shadow hiding (Figure 5.1a). This occurs when the illumination source (the sun) is nearly directly behind the remote sensing imager. In this orientation, the phase angle, defined as the angle between the imager's view and the solar illumination angle, is near zero. At these small phase angles surface roughness features (e.g., trees) block their own shadows from view, and therefore the scene appears brighter to the remote sensing imager than it would in a view from nadir in which shadows are visible (Hapke et al., 1996). This shadow hiding effect has also been described in the literature as contributing to observed "hotspots" (García-Haro & Sommer, 2002), the "opposition effect" (Ambeau, 2017), or "backscatter" (Deering et al., 1999). These terms are sometimes used to describe the combined effects of shadow hiding and coherent backscatter, though in this paper, our use of the terms "backscatter," and "hotspot" are meant to only refer to the observed increase in scene brightness due to the shadow hiding effect unless otherwise noted.

We used high temporal resolution GOES-16 (East) and -17 (West) ABI brightness temperature observations of Grand Mesa, Colorado (Figure 5.1b) to observe a flat snow and forest scene at a range of phase angles. To investigate reflectance anisotropy and the shadow hiding effect of both rough snow and forests, we used ABI band 7 (3.9 μm) in the MWIR and band 13 (10.3 μm) in the TIR. Our goals for understanding MWIR reflectance over forest and snow surfaces were to determine:

1) Can the timing of MWIR hotspots be predicted using the timing of the daily minimum phase angle?

2) How does the magnitude of MWIR hotspots vary with phase angle and with different amounts of forest versus open snow coverage in a pixel?

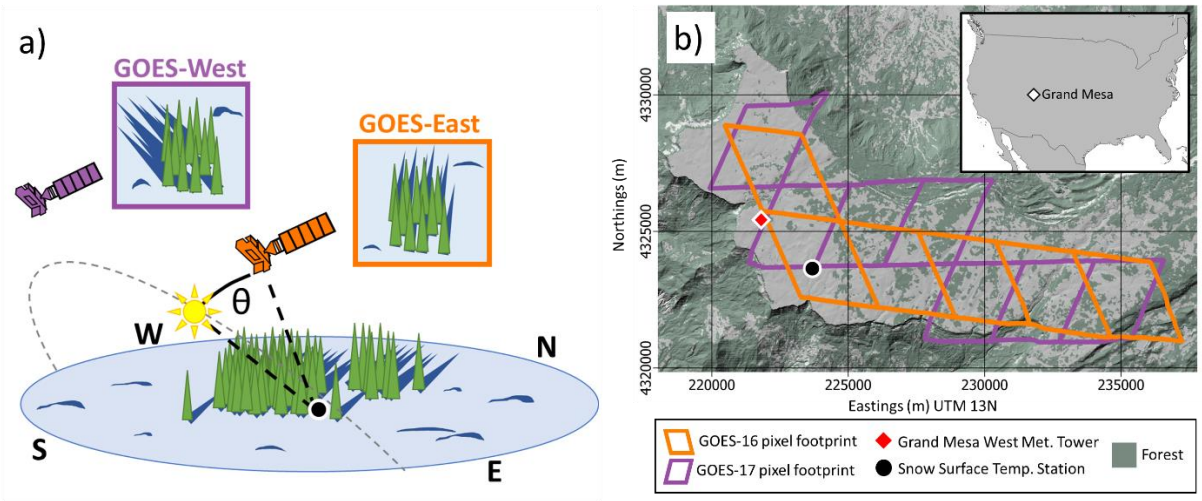

Figure 5.1. a) Illustration of the shadow hiding effect, solar illumination, and view geometry over a snow and forest scene. In this illustration, the small phase angle, θ, between GOES-East and the sun means that shadows cast by trees and sastrugi are nearly completely hidden from view. Therefore, the reflected MWIR radiance observed by GOES-East will be greater than that observed by GOES-West. b) Map of the study area over Grand Mesa in western Colorado, USA.

5.3 Background

In the daytime, the upward MWIR radiance coming from a land surface that is detected by a satellite imager will be a combination of surface-emitted MWIR and reflected solar MWIR (Figure 5.2). The amount of reflected solar MWIR depends on the total incoming solar radiation and the surface reflectance at these wavelengths, whereas the amount of emitted MWIR radiance is a function of the surface temperature and emissivity. For example, in the MWIR, snow has slightly higher emissivity (~0.995) and lower reflectivity (~0.005) than conifer vegetation (~0.985 and ~0.015 respectively), and therefore for snow and vegetation at the same temperature, snow will emit more but reflect less MWIR radiance. Cold snow surfaces will both emit and reflect less MWIR than warmer forest canopies. For the MWIR radiance detected by GOES-R

ABI band 7 (3.9 μm) from a snow-forest scene, 10-20% can come from reflected solar MWIR (Figure 5.2c). For MODIS MWIR bands 20-23 (3.6 to 4.1 μm), Lundquist et al. (2018) similarly found that as much as 10% of the detected MWIR can come from reflected solar radiation.

Snow and forests, however, are anisotropic reflectors, and therefore the reflected component of MWIR radiance detected will depend not just on the surface reflectance properties, but also on the solar illumination angle, the satellite view angle, and the phase angle between the two. In the visible to shortwave infrared wavelengths (~2 um), smooth snow surfaces are primarily foreword scattering, and increasingly so at lower sun angles or with larger snow grains (Aoki et al., 2000; D. K. Hall et al., 1993; Vikhamar & Solberg, 2003). Snow grain size and view angle are important controls on visible and near-infrared (NIR) reflectance, but in longer infrared wavelengths, reflectance depends primarily on view angle and is less sensitive to grain sizes (Warren, 2019). At spatial scales much larger than the wavelengths of incoming light, snow with rough wind-formed features such as sastrugi, ripples, or dunes large enough to cast shadows will cause the snow surface to appear backscattering at small phase angles due to the shadow hiding effect (Warren et al., 1998). Forests are also strongly back scattering due to the shadow hiding effect (Deering et al., 1999; D. K. Hall et al., 1993; Vikhamar & Solberg, 2003). The shadow hiding effect of vegetation was found to be more important than any other backscatter processes, such as coherent backscatter, at wavelengths with lower reflectance.

We hypothesized that MWIR backscatter observed on Grand Mesa would be dominated by the shadow hiding effect of the conifer trees, and therefore the magnitude of the MWIR hotspot should be stronger at phase angles closer to zero, and for GOES-R ABI pixels with larger fractional vegetated areas. For mixed pixels containing both snow and forests, the contribution of

each to the total backscatter observed will depend on the number, size, and distribution of surface roughness features casting shadows (e.g., trees and sastrugi).

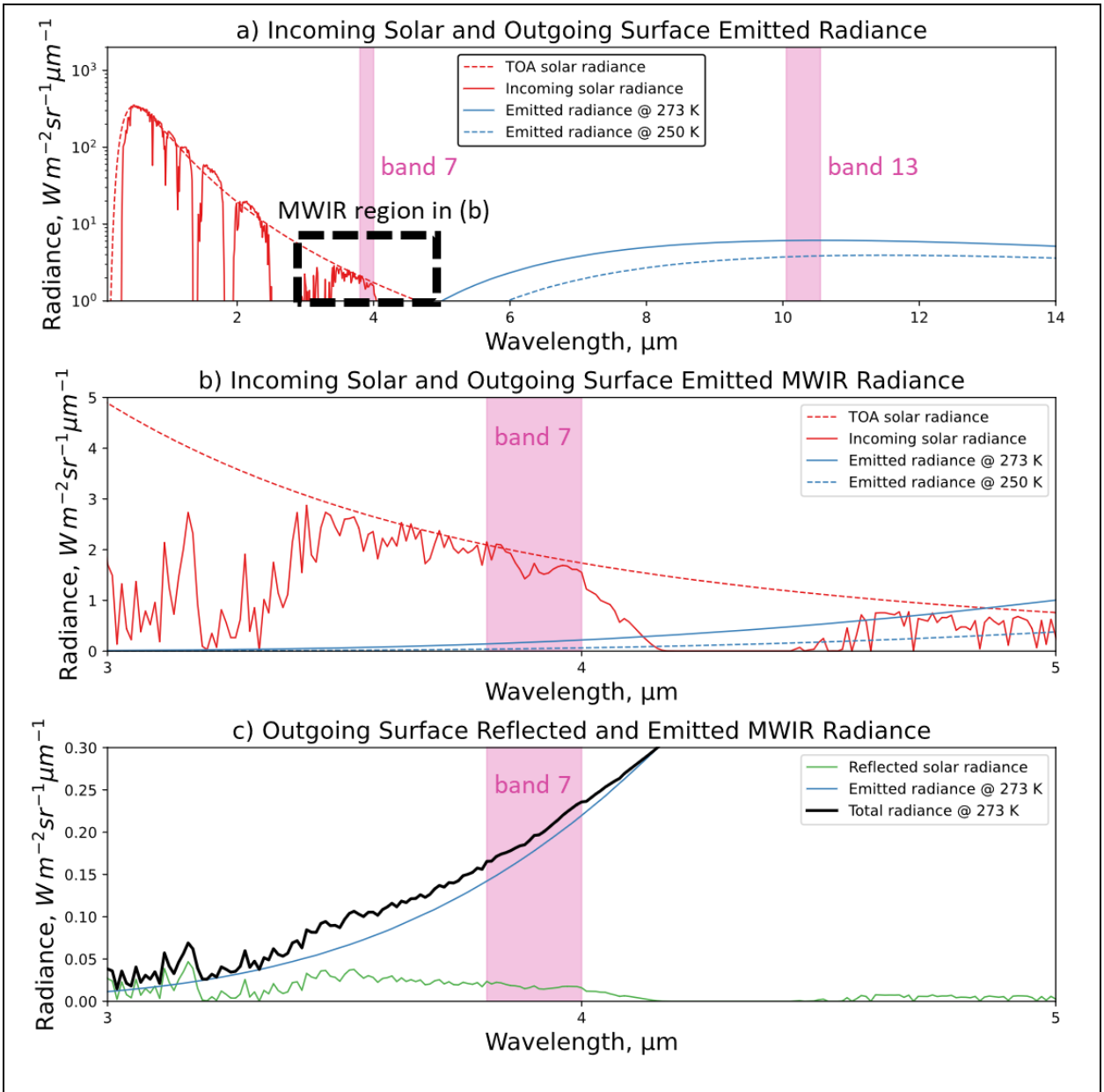

Figure 5.2. a) Plot of incoming solar radiance at the top of atmosphere and land surface (Gueymard, 2004; Lord, 1992) (red dashed and solid lines respectively) and outgoing emitted radiance from a mixed snow and forest surface at 250 and 273 K (blue dashed and solid lines respectively) (adapted from Figure 2 in Flynn (Flynn, 1996, p. 199)). The wavelengths covered by GOES-R ABI MWIR band 7 (3.9 µm) and TIR band 13 (10.3 µm) are indicated with shaded pink bars. b) Same as (a) but zoomed in to MWIR wavelengths between 3 and 5

μm. c) Plot of reflected solar radiance (green), emitted radiance (blue), and the sum total outgoing radiance (black) for a mixed forest (50% forest cover) and snow surface at 273 K.

5.4 Data

GOES-16 and -17 ABI 5-minute ABI-L1b-RadC radiance imagery for MWIR band 7 (3.9 μm), and TIR band 13 (10.3 μm) were downloaded for three days where imagery of the study site was cloud-free: 1 January 2021, 11 February 2020, and 3 March 2020. Timeseries were created for five GOES-16 and six GOES-17 pixels (Figure 5.1b) which covered the study site at Grand Mesa in western Colorado (39.02°, -108.12°). This high elevation, large, and flat snow-covered study area was partially forested with stands of conifer trees roughly increasing in density across the mesa from the tree-free western mesa to the more heavily forested eastern mesa (Figure 5.1b). Ground-based observations of snow surface temperature (Pestana & Lundquist, 2021) and, as a proxy for vegetation, air temperature (Houser & Mason, 2022), were used to simulate GOES-R band 7 and 13 observations with modeled MWIR reflectance.

5.5 Methods

5.5.1 Computing MWIR brightness temperature due to reflectance

To derive a MWIR reflectance signal from the timeseries of GOES-R ABI observations, we took the difference between the MWIR band 7 (3.9 μm) and TIR band 13 (10.3 μm) brightness temperatures ($\Delta T_B = T_{B,3.9} - T_{B,10.3}$). Without reflected solar radiation at night we expect ΔT_B for cloud-free observations of the Grand Mesa study site to be < 1 K, and this difference to vary little over the course of each night. We only expect to see a diurnal variation in ΔT_B due to reflected MWIR radiance in the daytime. Therefore, by computing the brightness temperature difference between these two bands (ΔT_B), we can focus on the reflected component of MWIR, its timing, and magnitude.

5.5.2 MWIR hotspot timing and magnitude

The azimuth and elevation angles for both GOES-16 and -17, which are fixed due to their geostationary orbits, were computed for the Grand Mesa study site. The solar azimuth, solar elevation, and phase angle between the sun and the satellite were computed at the same 5-minute temporal resolution as the GOES ABI imagery. Phase angles when the sun was rising towards each satellite were assigned positive values, while phase angles after the sun has passed its daily minimum phase angle (θ_{min}) were assigned negative values. The timing of the θ_{min} was then compared against that of the maximum daily MWIR-TIR brightness temperature difference ($\Delta T_{B,max}$).

For each GOES-R ABI pixel and each day of observation, the MWIR-TIR brightness temperature difference (ΔT_B) was plotted against the sun-satellite phase angle (θ). A "hotspot" curve (Equation 4.1) from Breon et al. (2002) was fit to the observations from each day. This function was chosen for its relative simplicity and ability to capture the asymmetry observed in the plots of ΔT_B against θ. The hotspot curve for each GOES-16 and -17 pixel across the study area were fit for daytime phase angles within $-50° < \theta < 50°$. The non-linear least squares method of the scipy Python package (Virtanen et al., 2020) was used to fit the hotspot curve to observations with four parameters (A, B, C, and a "half-width half-maximum term", θ_0). Prior work has used this hotspot factor to model hotspots due to the shadow hiding effect of forest canopies in visible and near infrared imagery (Duffour et al., 2016; Jiao et al., 2016). However, our use of this hotspot curve to model ΔT_B (units of K) as a function of θ means that the parameter values of our solutions do not necessarily have the same physical meanings as they have had in prior work with reflectance (unitless ratio) of visible and NIR imagery.

$$\Delta T_B(\theta) = \frac{A}{1 + \frac{|\theta|}{\theta_0}} + B + C\theta \quad (5.1)$$

We then looked for correlations between the fractional vegetated area (f_{veg}) of each ABI pixel across the study site, and metrics describing the phase angle dependent ΔT_B. From each fitted "hotspot factor" curve we interpolated a peak value of $\Delta T_B(\theta=0°)$ and the range between $\Delta T_B(\theta=50°)$ and $\Delta T_B(\theta= 0°)$ to describe the magnitude of observed ΔT_B. We computed the full-width at half-maximum (FWHM) as a metric of the decay of the "hotspot factor" with increasing phase angles. The fractional vegetated area (f_{veg}) of each GOES-R ABI pixel footprint was computed using a binary forest cover map created from the National Land Cover Database (NLCD) 2016 Tree Canopy Cover (TCC) product (Coulston et al., 2012), with the binary threshold set at 20% TCC.

5.5.3 Simulating GOES-R ABI observations

To compare the GOES-R ABI observations with our prior assumptions of snow and vegetation reflectance, we used the ground-based temperature measurements to simulate ABI observations at bands 7 and 13 for 11 February 2020. For the center wavelength (λ) of each ABI band, snow (T_{snow}) and vegetation temperatures (T_{veg}) were converted to radiances with the Planck equation ($\beta(\lambda, T)$), and scaled by their emissivities. Conifer emissivities (ε_{veg}) from the MODIS UCSB Emissivity Library (Z. M. Wan & Zhang, 1999) were used for vegetation, and snow emissivity (ε_{snow}) was computed as a function of the satellite's view angle (ϕ) with the Dozier-Warren Mie scattering model (Dozier & Warren, 1982). Vegetation reflectance ($r_{veg,\lambda}$), assumed to be an isotropic reflector, was computed as $r_{veg,\lambda} = 1 - \varepsilon_{veg,\lambda}$, whereas snow reflectance ($r_{snow,\lambda}$) was computed as a function of the solar illumination angle (where μ is the cosine of that angle), again with the Dozier-Warren Mie scattering model. Incoming clear-sky solar radiation

($R_{\downarrow,\lambda}$) was estimated as a function of the solar illumination angle (μ). The sum of the subpixel radiances (L) due to emission and reflection, weighted by their fractional areas of the ABI pixel (f_{veg}=13% and 16% for pixel A of GOES-16 and -17, respectively), was computed and converted to brightness temperature with the inverse Planck equation ($T^*_{B,\lambda} = \beta^{-1}(\lambda, L)$) to create the final mixed pixel signal (Equation 4.2). Finally, we computed our modeled (where the * indicates a modeled value rather than observed) MWIR – TIR difference as $\Delta T^*_B = T^*_{B,\lambda=3.9} - T^*_{B,\lambda=10.3}$.

$$T^*_{B,\lambda} = \beta^{-1}\big(\lambda, \big(1 - f_{veg}\big) \cdot \varepsilon_{snow,\lambda}(\phi) \cdot \beta(\lambda, T_{snow}) + f_{veg} \cdot \varepsilon_{veg,\lambda} \cdot \beta\big(\lambda, T_{veg}\big) + \big(1 - f_{veg}\big) \cdot r_{snow,\lambda}(\mu) \cdot R_{\downarrow,\lambda}(\mu) + f_{veg} \cdot r_{veg,\lambda} \cdot R_{\downarrow,\lambda}(\mu)\big) \quad (5.2)$$

5.6 Results and discussion

5.6.1 MWIR hotspot timing and magnitude

On all three days, observed ΔT_B values were near 0 K at night, and peaked between 3 - 7 K in the daytime. Daily maximum ΔT_B for both GOES-16 and -17, for all pixels across the study area, occurred within < 30 minutes of the time of the predicted daily minimum phase angle. This helped confirm that since the ΔT_B signal is strongly controlled by the phase angle, the signal is likely due to MWIR reflectance and the shadow hiding effect, appearing much like hotspots observed in visible and NIR imagery (Hapke et al., 1996; Jiao et al., 2016).

However, there was no correlation between the ABI pixels' f_{veg} and the magnitude or width of the hotspot signals. Snow surface roughness features, such as wind-formed sastrugi or ripples, in the mostly open-snow areas must therefore be exhibiting shadow hiding effects comparable to that of trees. The hotspot curves best fit with observations from 3 March 2020, with an RMSE < 0.3 K, when both GOES-16 and -17 reached θ_{min} < 0.5°. These hotspot curves predicted $\Delta T_B(\theta=0°)$ of ~5.8 K for GOES-16 and ~6.3 K for GOES-17 (Figure 5.3e,f). The hotspot curves for 1 January 2021 (Figure 5.3a,b), and 11 February, 2020 (Figure 5.3c,d), fit with RMSE < 1.0

K, and most predicted ΔTB(θ=0°) of 5 – 13 K. These days lacked observations at very small phase angles (θmin of ~15° and ~8° respectively), leading some curve fits to predict unrealistic ΔTB(θ=0°) >> 100 K (e.g. Figure 5.3a).

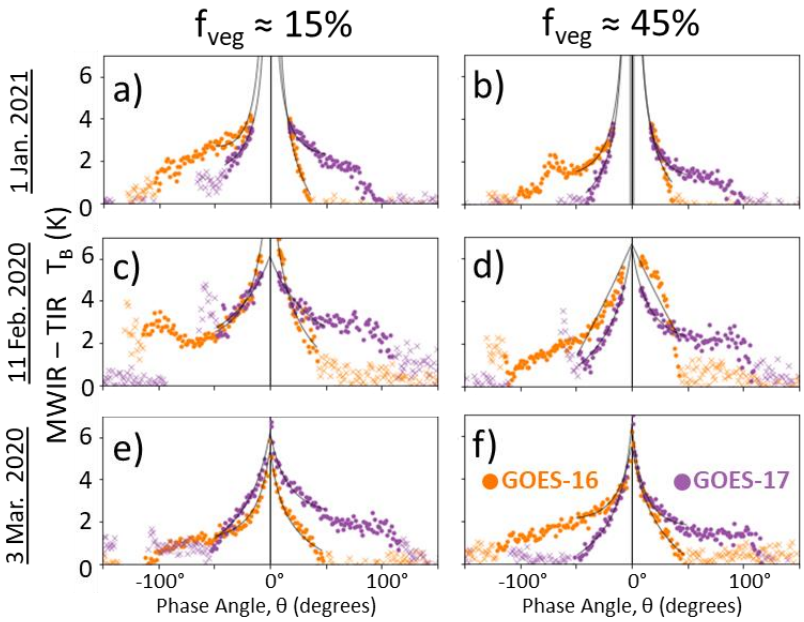

Figure 5.3. Plots of ΔT_B versus phase angle (θ) for two pixels on three days of observations, with GOES-16 in orange and GOES-17 in purple. The pixels had fractional vegetated areas of (a, c, e) 15%, and (b, d, f) 45%. Grey lines are hotspot curves fit to daytime observations with phase angles within ±50° (note: Figure 4.3c is the same as Figure 4.4f).

5.6.2 Asymmetry in the MWIR hotspot

The relationship between ΔT_B and θ was found to be asymmetrical for both GOES-16 and -17, for all pixels, and on each day of observations. GOES-16 ΔT_B showed a quick increase with phase angle in the mornings, and a longer tailed decrease after it passed θ_{min}. GOES-17 ΔT_B showed the opposite pattern over time. These long tails both occurred at times when the sun was highest in the sky near solar noon, and therefore more incoming solar radiation is available to be reflected. The near mirror-image patterns of ΔT_B were especially apparent in pairs of pixels that had similar f_{veg} (Figure 5.3). This is not entirely surprising, given that GOES-16 and -17 have

very similar view zenith angles of the Grand Mesa study site (56.5° and 54.1° respectively), and the pairs of GOES-16/17 pixel footprints were chosen to overlap as much as possible.

In addition to the overall asymmetry of ΔT_B versus θ, there were some secondary increases in ΔT_B at larger phase angles between ±75° and ±100° (e.g., Figure 5.3b,c). These were observed for GOES-16 just before sunset and for GOES-17 just after sunrise. These secondary ΔT_B increases cannot be explained by specular reflection since the satellites are viewing this study area from the same general direction as incident solar illumination. Mie scattering theory does predict snow reflectivity to be highest at low illumination angles (Warren, 1982), which may account for the secondary increases in ΔT_B observed.

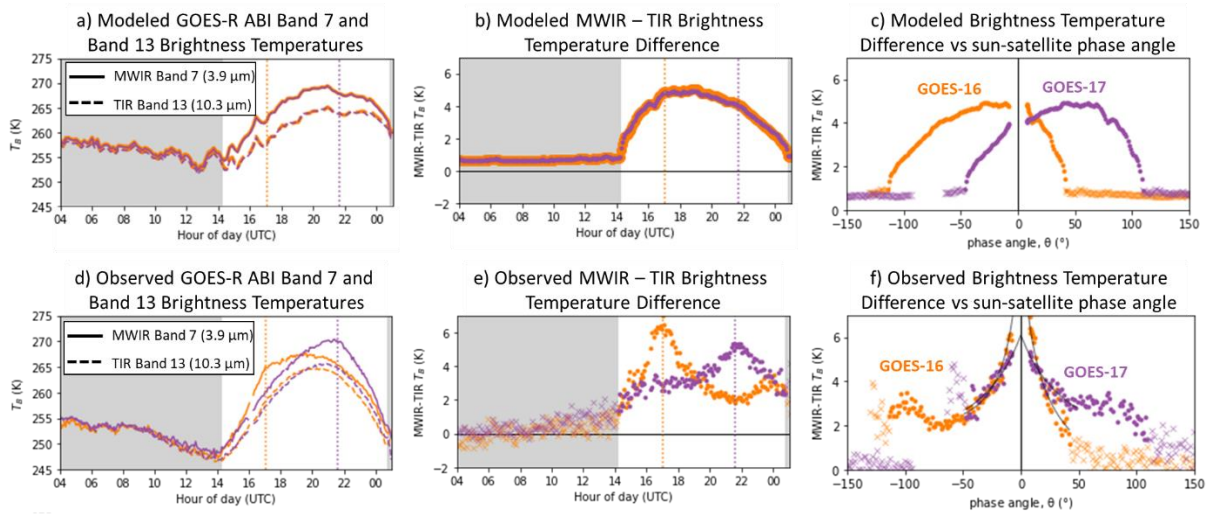

Figure 5.4. Top row is modeled, bottom row is observed: a,d) Timeseries of GOES-R ABI MWIR band 7 (3.9 µm) and TIR band 13 (10.3 µm) brightness temperatures for GOES-16 (orange) and GOES-17 (purple) on 11 February 2020 over western Grand Mesa, Colorado. The difference between MWIR band 7 and TIR band 13 b,e) over time, and c,f) by sun-satellite phase angle (θ) with fitted curves and nighttime phase angles marked as colored x's, daytime phase angles as dots. Shaded areas on timeseries plots (a, b, d, e) indicate nighttime, and vertical dotted lines indicate the time of the daily minimum phase angle.

5.6.3 Comparison with simulated MWIR reflectance

The modeled ΔT_B^* (Equation 4.2; Figure 5.4b,c) reached a similar magnitude as the observed ΔT_B (Figure 5.4e,f), but did not capture the observed diurnal pattern. The daily peak in ΔT_B

observed at θ_{min} was a very brief event, whereas our modeled ΔT_B^* followed the smooth diurnal pattern of incoming solar illumination and solar zenith angle. This illustrated the model's incorrect assumption that reflected MWIR from a mostly snow-covered pixel was dependent only on the amount of incoming solar radiation and the solar illumination angle. Rather than accounting for the more complex reflectance properties of a rough surface casting shadows, this model treated vegetation and snow reflectance completely independently.

5.7 Conclusions

For infrared spectral separation methods, the reflected component of MWIR must either be estimated or solved for directly. Observations from GOES-R ABI of MWIR hotspots over snow and forests demonstrate that it is not sufficient to estimate MWIR reflectance of these surfaces independently. Rather, the combined effects of snow and vegetation surface roughness, the distribution and orientation of surface roughness features, and sun-satellite phase angle must be considered.

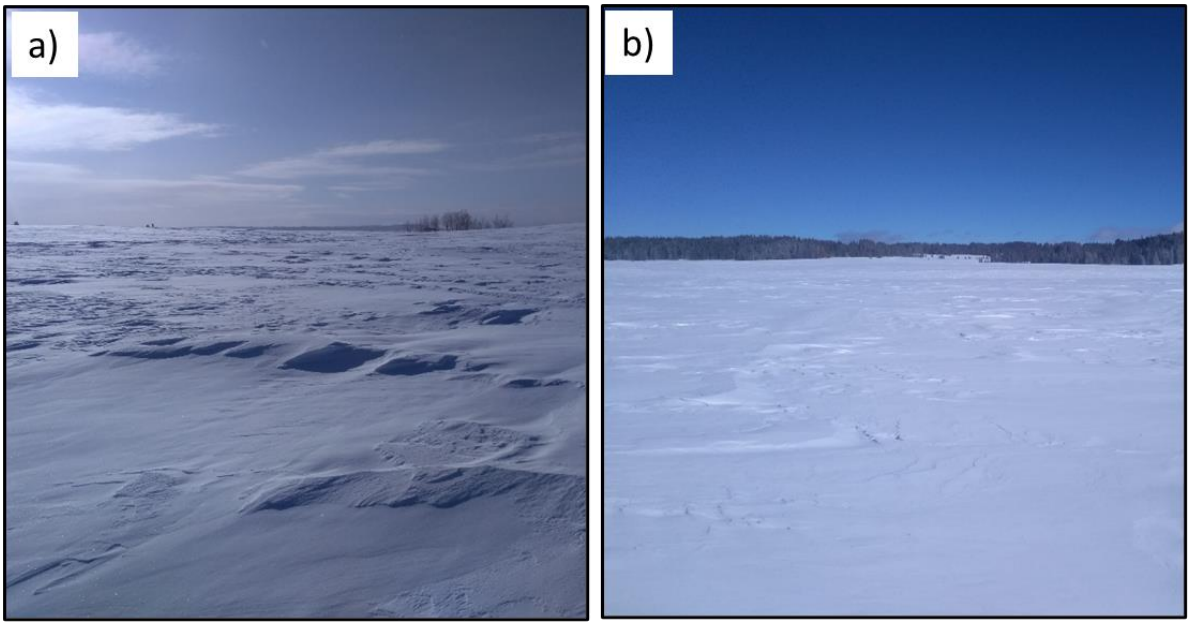

Figure 5.5. Photos of the rough windblown snow surface of western Grand Mesa, Colorado on 5 February 2020, a) with shadows visible looking south at 09:30 local time (UTC-07:00) (solar zenith angle (SZA) = 68°), and b) with shadows hidden looking northeast at 14:30 (SZA = 62°).

The peak of observed MWIR hotspots were coincident with the daily minimum sun-satellite phase angle, but neither their magnitude nor shape correlated with the fractional vegetated area of the ABI pixel. This supported the shadow hiding hypothesis, but not the hypothesis that this would primarily be an effect due to trees casting shadows. Snow roughness features such as sastrugi or ripples must also be prevalent enough to exhibit shadow hiding (Figure 5.5). Asymmetry in the hotspot signal with phase angle showed increased MWIR reflectance mid-day, when solar illumination was greatest, and some secondary increases in reflectance at larger phase angles (between ~75-100 degrees), suggesting other reflectance effects besides shadow hiding.

To solve the infrared spectral separation problem for high-temporal resolution, off-nadir GOES-R ABI observations, our model of MWIR reflectance needs to be updated to include shadow hiding effects. Modeling the MWIR reflectance of a mixed snow-forest pixel will either require information about specific surface roughness features to determine shadow hiding at different illumination angles from the satellite point of view, or building empirical models from observations unique to each pixel.

5.8 Acknowledgements

This research was funded by NASA FINESST grant 80NSSC20K1610. We would like to thank Karl Lapo for providing the solar geometry code used in this study.

Chapter 6. Conclusions

Distributed observations of snow surface temperatures in mountain watersheds at model-relevant spatial and temporal resolutions are needed to better constrain uncertainties in the surface energy balance of seasonal snow (Dozier & Marks, 1992; Hinkelman et al., 2012; Lapo et al., 2015; Raleigh et al., 2016). Geostationary satellites, such as the NOAA GOES-R series, can provide imagery at high temporal resolutions due to their fixed views of Earth's surface. The utility of these observations, however, is challenged by their 2+ km spatial resolution and off-nadir view angles (Schmit et al., 2017). In this dissertation we have worked towards building an understanding of how these factors impact GOES-R surface temperature observations. We particularly focused on snow in forested mountain regions of the western United States, where extensive ground-based and remote sensing observation provided coincident datasets for comparison.

In Chapter 2, we demonstrated the necessity of correcting for the parallax effect of mountain terrain to properly align GOES-R observations of mountain regions with other remote sensing and map data (Pestana & Lundquist, 2022). We found that GOES-16, viewing the California Sierra Nevada study area in the Northern Hemisphere from the south, reported surface brightness temperatures biased towards those of the south-facing mountain slopes. In daytime imagery, these south-facing slopes received more sunlight and were therefore warmer than north-facing slopes, leading to a warm bias in the GOES-16 imagery. Chapter 3 summarized the Python software developed to perform orthorectification of GOES-R imagery.

In Chapter 4, we conducted an intercomparison of remotely sensed and ground-based snow surface temperature observations across the flat expanse of Grand Mesa in western Colorado, USA, as part of the NASA SnowEx 2020 field campaign. This unique study site allowed us to

investigate how forest cover impacted surface temperature observations by the off-nadir viewing GOES-16 (GOES-East), and GOES-17 (GOES-West) geostationary satellites. We found that analogous to the "shadow hiding" or "hotspot" effects seen in visible and NIR imagery, there was a "thermal infrared shadow hiding" occurring where the difference between nadir-looking and off-nadir-looking thermal infrared imagery changed over the course of the day as the sun traversed the sky, heated different portions of the forest canopy, and cast shadows in different directions.

In Chapter 5, the investigation of shadow hiding at Grand Mesa was extended into the mid-wave infrared (MWIR) wavelengths. MWIR observations are especially important for infrared spectral unmixing methods that rely on the small differences in brightness temperatures between the MWIR and TIR wavelengths dependent on subpixel temperatures (Dozier, 1981; Lundquist et al., 2018). Daytime observations in the MWIR are further complicated given that the MWIR radiance observed will be a mixture of both emitted MWIR and reflected solar MWIR. Our investigation at Grand Mesa found that MWIR reflectance was strongly controlled by the sun-satellite phase angle, exhibiting a "shadow hiding" or "hotspot"-like appearance. This however was not correlated with forest cover as was the thermal infrared shadow hiding in Chapter 3. Rather, the effect was present in both forested areas and open snow surfaces, suggesting that snow surface roughness features such as sastrugi, ripples, or dunes are also contributing to the MWIR hotspot observed. Future work to use high temporal resolution, geostationary MWIR, and TIR imagery for infrared spectral separation will therefore need to incorporate models of MWIR reflectance that account for solar illumination and surface roughness features of snow and vegetation.

This work has demonstrated that knowledge of land surface properties, such as surface roughness at different spatial scales, are needed for mountain surface temperature applications of geostationary satellite imagery. Surface roughness features, from multi-kilometer-scale mountain terrain, kilometer-scale forests, meter-scale trees, to centimeter-scale snow ripples, will influence surface temperature observations by geostationary satellites. The impact of these surface roughness features will vary over the course of the day as solar illumination changes. A priori information about terrain and forest coverage, together with empirical relationships from prior observations, could provide the context needed for interpreting mountain snow surface temperature observations from geostationary satellites.

References

Abrams, M. (2000). The Advanced Spaceborne Thermal Emission and Reflection Radiometer (ASTER): Data products for the high spatial resolution imager on NASA's Terra platform. *International Journal of Remote Sensing*, *21*(5), 847–859. https://doi.org/10.1080/014311600210326

Ambeau, B. (2017). *Using the Opposition Effect in Remotely Sensed Data to Assist in the Retrieval of Bulk Density*. 100.

Anderson, M. C., Kustas, W. P., Norman, J. M., Hain, C. R., Mecikalski, J. R., Schultz, L., González-Dugo, M. P., Cammalleri, C., d'Urso, G., Pimstein, A., & Gao, F. (2011). Mapping daily evapotranspiration at field to continental scales using geostationary and polar orbiting satellite imagery. *Hydrology and Earth System Sciences*, *15*(1), 223–239. https://doi.org/10.5194/hess-15-223-2011

Aoki, T., Fukabori, M., Hachikubo, A., Tachibana, Y., & Nishio, F. (2000). Effects of snow physical parameters on spectral albedo and bidirectional reflectance of snow surface. *Journal of Geophysical Research: Atmospheres*, *105*(D8), 10219–10236. https://doi.org/10.1029/1999JD901122

Balick, L. K., Jerrell R., B., Smith, J. A., & Goltz, S. M. (2002). Directional satellite thermal IR measurements and modeling of a forest in winter and their relationship to air temperature. *Remote Sensing for Agriculture, Ecosystems, and Hydrology III*, *4542*, 162–169. https://doi.org/10.1117/12.454212

Barnes, W. L., Pagano, T. S., & Salomonson, V. V. (1998). Prelaunch characteristics of the Moderate Resolution Imaging Spectroradiometer (MODIS) on EOS-AM1. *IEEE Transactions on Geoscience and Remote Sensing*, *36*(4), 1088–1100. https://doi.org/10.1109/36.700993

Barnett, T. P., Adam, J. C., & Lettenmaier, D. P. (2005). Potential impacts of a warming climate on water availability in snow-dominated regions. *Nature*, *438*(7066), 303–309. https://doi.org/10.1038/nature04141

Berk, A., Conforti, P., Kennett, R., Perkins, T., Hawes, F., & van den Bosch, J. (2014). MODTRAN6: A major upgrade of the MODTRAN radiative transfer code. In Miguel Velez-Reyes & Fred A. Kruse (Eds.), *Algorithms and Technologies for Multispectral, Hyperspectral, and Ultraspectral Imagery XX* (Vol. 9088, pp. 90880H-90880H – 7). Proceedings of SPIE.

Bhushan, S., Henderson, S., & Shean, D. (2022). Asp-binder-demo. In *GitHub repository*. GitHub. https://github.com/uw-cryo/asp-binder-demo

Bian, J., Li, A., Zhao, W., & Yin, G. (2017). An automatic orthorectification approach for the time series GF-4 geostationary satellite images in Mountainous area. *2017 IEEE International Geoscience and Remote Sensing Symposium (IGARSS)*, 546–549. https://doi.org/10.1109/IGARSS.2017.8127011

Böhner, J., & Antonić, O. (2009). Chapter 8 Land-Surface Parameters Specific to Topo-Climatology. In T. Hengl & H. I. Reuter (Eds.), *Geomorphometry* (Vol. 33, pp. 195–226). Elsevier. https://doi.org/10.1016/S0166-2481(08)00008-1

Bréon, F.-M., Maignan, F., Leroy, M., & Grant, I. (2002). Analysis of hot spot directional signatures measured from space. *Journal of Geophysical Research: Atmospheres*, *107*(D16), AAC 1-1-AAC 1-15. https://doi.org/10.1029/2001JD001094

Cawse-Nicholson, K., Townsend, P. A., Schimel, D., Assiri, A. M., Blake, P. L., Buongiorno, M. F., Campbell, P., Carmon, N., Casey, K. A., Correa-Pabón, R. E., Dahlin, K. M., Dashti,

H., Dennison, P. E., Dierssen, H., Erickson, A., Fisher, J. B., Frouin, R., Gatebe, C. K., Gholizadeh, H., … Zhang, Q. (2021). NASA's surface biology and geology designated observable: A perspective on surface imaging algorithms. *Remote Sensing of Environment*, *257*, 112349. https://doi.org/10.1016/j.rse.2021.112349

Chen, W., Pinker, R. T., Ma, Y., Hulley, G., Borbas, E., Islam, T., Cawse-Nicholson, K.-A., Hook, S., Hain, C., & Basara, J. (2021). Land Surface Temperature from GOES-East and GOES-West. *Journal of Atmospheric and Oceanic Technology*, *38*(4), 843–858. https://doi.org/10.1175/JTECH-D-20-0086.1

Colbeck, S. C. (1989). Air Movement in Snow Due to Windpumping. *Journal of Glaciology*, *35*(120), 209–213. https://doi.org/10.3189/S0022143000004524

Coulston, J. W., Moisen, G. G., Wilson, B. T., Finco, M. V., Cohen, W. B., & Brewer, C. K. (2012). Modeling Percent Tree Canopy Cover: A Pilot Study. *Photogrammetric Engineering & Remote Sensing*, *78*(7), 715–727.

Cracknell, A. P. (1998). Review article Synergy in remote sensing-what's in a pixel? *International Journal of Remote Sensing*, *19*(11), 2025–2047. https://doi.org/10.1080/014311698214848

Cristea, N. C., Breckheimer, I., Raleigh, M. S., HilleRisLambers, J., & Lundquist, J. D. (2017). An evaluation of terrain-based downscaling of fractional snow covered area data sets based on LiDAR-derived snow data and orthoimagery: DOWNSCALING OF FRACTIONAL SNOW COVERED AREA. *Water Resources Research*, *53*(8), 6802–6820. https://doi.org/10.1002/2017WR020799

Currier, W. R., Pflug, J., Mazzotti, G., Jonas, T., Deems, J. S., Bormann, K. J., Painter, T. H., Hiemstra, C. A., Gelvin, A., Uhlmann, Z., Spaete, L., Glenn, N. F., & Lundquist, J. D. (2019). Comparing Aerial Lidar Observations With Terrestrial Lidar and Snow-Probe Transects From NASA's 2017 SnowEx Campaign. *Water Resources Research*, *55*(7), 6285–6294. https://doi.org/10.1029/2018WR024533

Deering, D. W., Eck, T. F., & Banerjee, B. (1999). Characterization of the Reflectance Anisotropy of Three Boreal Forest Canopies in Spring–Summer. *Remote Sensing of Environment*, *67*(2), 205–229. https://doi.org/10.1016/S0034-4257(98)00087-X

Desai, A. R., Khan, A. M., Zheng, T., Paleri, S., Butterworth, B., Lee, T. R., Fisher, J. B., Hulley, G., Kleynhans, T., Gerace, A., Townsend, P. A., Stoy, P., & Metzger, S. (2021). Multi-Sensor Approach for High Space and Time Resolution Land Surface Temperature. *Earth and Space Science*, *8*(10). https://doi.org/10.1029/2021EA001842

Ding, L., Zhou, J., Zhang, X., Liu, S., & Cao, R. (2018). Downscaling of surface air temperature over the Tibetan Plateau based on DEM. *International Journal of Applied Earth Observation and Geoinformation*, *73*, 136–147. https://doi.org/10.1016/j.jag.2018.05.017

Dozier, J. (1981). A method for satellite identification of surface temperature fields of subpixel resolution. *Remote Sensing of Environment*, *11*, 221–229. https://doi.org/10.1016/0034-4257(81)90021-3

Dozier, J., & Marks, D. (1992). Climate and Energy Exchange at the Snow Surface in the Alpine Region of the Sierra Nevada 2. Snow Cover Energy Balance. *Water Resources Research*, *28*(11), 3043–3054.

Dozier, J., Painter, T. H., Rittger, K., & Frew, J. E. (2008). Time–space continuity of daily maps of fractional snow cover and albedo from MODIS. *Advances in Water Resources*, *31*(11), 1515–1526. https://doi.org/10.1016/j.advwatres.2008.08.011

Dozier, J., & Warren, S. G. (1982). Effect of viewing angle on the infrared brightness temperature of snow. *Water Resources Research*, *18*(5), 1424–1434. https://doi.org/10.1029/WR018i005p01424

Duffour, C., Lagouarde, J.-P., & Roujean, J.-L. (2016). A two parameter model to simulate thermal infrared directional effects for remote sensing applications. *Remote Sensing of Environment*, *186*, 250–261. https://doi.org/10.1016/j.rse.2016.08.012

Essery, R., Bunting, P., Rowlands, A., Rutter, N., Hardy, J., Melloh, R., Link, T., Marks, D., & Pomeroy, J. (2008). Radiative Transfer Modeling of a Coniferous Canopy Characterized by Airborne Remote Sensing. *Journal of Hydrometeorology*, *9*(2), 228–241. https://doi.org/10.1175/2007JHM870.1

Essery, R., Morin, S., Lejeune, Y., & B Ménard, C. (2013). A comparison of 1701 snow models using observations from an alpine site. *Advances in Water Resources*, *55*, 131–148. https://doi.org/10.1016/j.advwatres.2012.07.013

Flanner, M. G., & Zender, C. S. (2006). Linking snowpack microphysics and albedo evolution. *Journal of Geophysical Research Atmospheres*, *111*(12), 1–12. https://doi.org/10.1029/2005JD006834

Flynn, L. (1996). Thermal anomaly low spatial resolution. *EOS Volcanology Team Data Product Document MOU*, 81–3292.

Francis, P., & Rothery, D. (2000). Remote Sensing of Active Volcanoes. *Annual Review of Earth and Planetary Sciences*, *28*(1), 81–106. https://doi.org/10.1146/annurev.earth.28.1.81

García-Haro, F. J., & Sommer, S. (2002). A fast canopy reflectance model to simulate realistic remote sensing scenarios. *Remote Sensing of Environment*, *81*(2–3), 205–227. https://doi.org/10.1016/S0034-4257(01)00344-3

Giglio, L., & Kendall, J. D. (2001). Application of the Dozier retrieval to wildfire characterization: A sensitivity analysis. *Remote Sensing of Environment*, *77*(1), 34–49. https://doi.org/10.1016/S0034-4257(01)00192-4

Gillespie, A., Rokugawa, S., Matsunaga, T., Steven Cothern, J., Hook, S., & Kahle, A. B. (1998). A temperature and emissivity separation algorithm for advanced spaceborne thermal emission and reflection radiometer (ASTER) images. *IEEE Transactions on Geoscience and Remote Sensing*. https://doi.org/10.1109/36.700995

GOES-R Calibration Working Group, & GOES-R Program Office. (2017). *NOAA GOES-R Series Advanced Baseline Imager (ABI) Level 1b Radiances*.

GOES-R. Calibration Working Group, & GOES-R Program Office. (2018). *NOAA GOES-R Series Advanced Baseline Imager (ABI) Level 2 Land Surface Temperature (LST)*.

Gueymard, C. A. (2004). The sun's total and spectral irradiance for solar energy applications and solar radiation models. *Solar Energy*, *76*(4), 423–453. https://doi.org/10.1016/j.solener.2003.08.039

Guillevic, P. C., Privette, J. L., Coudert, B., Palecki, M. A., Demarty, J., Ottlé, C., & Augustine, J. A. (2012). Land Surface Temperature product validation using NOAA's surface climate observation networks—Scaling methodology for the Visible Infrared Imager Radiometer Suite (VIIRS). *Remote Sensing of Environment*, *124*, 282–298. https://doi.org/10.1016/j.rse.2012.05.004

Hall, D., Box, J., Casey, K., Hook, S., Shuman, C., & Steffen, K. (2008). Comparison of satellite-derived and in-situ observations of ice and snow surface temperatures over Greenland. *Remote Sensing of Environment*, *112*(10), 3739–3749. https://doi.org/10.1016/j.rse.2008.05.007

Hall, D. K., Foster, J. L., Irons, J. R., & Dabney, P. W. (1993). Airborne bidirectional radiances of snow-covered surfaces in Montana, U.S.A. *Annals of Glaciology*, *17*, 35–40. https://doi.org/10.3189/S0260305500012581

Hall, D. K., & Riggs, G. A. (2007). Accuracy assessment of the MODIS snow products. *Hydrological Processes: An International Journal*, *21*(12), 1534–1547.

Hapke, B., DiMucci, D., Nelson, R., & Smythe, W. (1996). The cause of the hot spot in vegetation canopies and soils: Shadow-hiding versus coherent backscatter. *Remote Sensing of Environment*, *58*(1), 63–68. https://doi.org/10.1016/0034-4257(95)00257-X

Harris, A. J. L., Pilger, E., Flynn, L. P., Garbeil, H., Mouginis-Mark, P. J., Kauahikaua, J., & Thornber, C. (2001). Automated, high temporal resolution, thermal analysis of Kilauea volcano, Hawai'i, using GOES satellite data. *International Journal of Remote Sensing*, *22*(6), 945–967. https://doi.org/10.1080/014311601300074487

Henderson, B. G., Balick, L. K., Rodger, A. P., & Pope, P. A. (2003). *Concurrent measurements of directional reflectance and temperature of a wintertime coniferous forest from space*. 21. https://doi.org/10.1117/12.506296

Hinkelman, L., Zhang, T., & Stackhouse, P. (2012). Comparisons of Satellite-Estimated Radiative Fluxes Reaching the Surface to Ground Observations. *GEWEX Radiative Flux Assessment (RFA) Volume 1: Assessment*, *1992*(July 1983), 159–187.

Hori, M., Aoki, T., Tanikawa, T., Hachikubo, A., Sugiura, K., Kuchiki, K., & Niwano, M. (2013). Modeling angular-dependent spectral emissivity of snow and ice in the thermal infrared atmospheric window. *Applied Optics*, *52*(30), 7243. https://doi.org/10.1364/AO.52.007243

Hori, M., Aoki, T., Tanikawa, T., Motoyoshi, H., Hachikubo, A., Sugiura, K., Yasunari, T. J., Eide, H., Storvold, R., Nakajima, Y., & Takahashi, F. (2006). In-situ measured spectral directional emissivity of snow and ice in the 8–14 μm atmospheric window. *Remote Sensing of Environment*, *100*(4), 486–502. https://doi.org/10.1016/j.rse.2005.11.001

Houser, P. ,. W. Rudisill, J. Johnston, K. Elder, H. Marshall, C. M. Vuyovich, E. J. Kim, & Mason, M. (2022). *SnowEx Meteorological Station Measurements from Grand Mesa, CO, Version 1*. NASA National Snow and Ice Data Center Distributed Active Archive Center. https://doi.org/10.5067/497NQVJ0CBEX

Howard, R., & Stull, R. (2013). IR Radiation from Trees to a Ski Run: A Case Study. *Journal of Applied Meteorology and Climatology*, *52*(7), 1525–1539. https://doi.org/10.1175/JAMC-D-12-0222.1

Hulley, G. C., Hook, S. J., & Hughes, C. (2012). *MODIS MOD21 land surface temperature and emissivity algorithm theoretical basis document*. Pasadena, CA: Jet Propulsion Laboratory, National Aeronautics and Space ….

Immerzeel, W. W., Lutz, A. F., Andrade, M., Bahl, A., Biemans, H., Bolch, T., Hyde, S., Brumby, S., Davies, B. J., Elmore, A. C., Emmer, A., Feng, M., Fernández, A., Haritashya, U., Kargel, J. S., Koppes, M., Kraaijenbrink, P. D. A., Kulkarni, A. V., Mayewski, P. A., … Baillie, J. E. M. (2020). Importance and vulnerability of the world's water towers. *Nature*, *577*(7790), 364–369. https://doi.org/10.1038/s41586-019-1822-y

Inamdar, A. K., & French, A. (2009). Disaggregation of GOES land surface temperatures using surface emissivity: DISAGGREGATION OF GOES LST. *Geophysical Research Letters*, *36*(2), n/a-n/a. https://doi.org/10.1029/2008GL036544

Jiao, Z., Schaaf, C. B., Dong, Y., Román, M., Hill, M. J., Chen, J. M., Wang, Z., Zhang, H., Saenz, E., Poudyal, R., Gatebe, C., Bréon, F.-M., Li, X., & Strahler, A. (2016). A method

for improving hotspot directional signatures in BRDF models used for MODIS. *Remote Sensing of Environment*, *186*, 135–151. https://doi.org/10.1016/j.rse.2016.08.007

Jin, M., & Dickinson, R. E. (2010). Land surface skin temperature climatology: Benefitting from the strengths of satellite observations. *Environmental Research Letters*, *5*(4), 044004. https://doi.org/10.1088/1748-9326/5/4/044004

Johnson, M., Sandusky, M., & Marshall, H. (2023). *SnowEx/snowexsql: SnowEx Hackweek 2022 release | Zenodo* [Computer software]. https://zenodo.org/record/7618102

Joyce, R., Janowiak, J., & Huffman, G. (2001). Latitudinally and Seasonally Dependent Zenith-Angle Corrections for Geostationary Satellite IR Brightness Temperatures. *Journal of Applied Meteorology*, *40*(4), 689–703. https://doi.org/10.1175/1520-0450(2001)040<0689:LASDZA>2.0.CO;2

Kalluri, S., Alcala, C., Carr, J., Griffith, P., Lebair, W., Lindsey, D., Race, R., Wu, X., & Zierk, S. (2018). From Photons to Pixels: Processing Data from the Advanced Baseline Imager. *Remote Sensing*, *10*(2), 177. https://doi.org/10.3390/rs10020177

Kim, Y., Still, C. J., Roberts, D. A., & Goulden, M. L. (2018). Thermal infrared imaging of conifer leaf temperatures: Comparison to thermocouple measurements and assessment of environmental influences. *Agricultural and Forest Meteorology*, *248*, 361–371. https://doi.org/10.1016/j.agrformet.2017.10.010

Kochanski, K., Anderson, R. S., & Tucker, G. E. (2019). The evolution of snow bedforms in the Colorado Front Range and the processes that shape them. *The Cryosphere*, *13*(4), 1267–1281. https://doi.org/10.5194/tc-13-1267-2019

Koltunov, A., Ustin, S. L., Quayle, B., Schwind, B., Ambrosia, V. G., & Li, W. (2016). The development and first validation of the GOES Early Fire Detection (GOES-EFD) algorithm. *Remote Sensing of Environment*, *184*, 436–453. https://doi.org/10.1016/j.rse.2016.07.021

Kustas, W. P., Norman, J. M., Anderson, M. C., & French, A. N. (2003). Estimating subpixel surface temperatures and energy fluxes from the vegetation index–radiometric temperature relationship. *Remote Sensing of Environment*, *85*(4), 429–440. https://doi.org/10.1016/S0034-4257(03)00036-1

Lapo, K. E., Hinkelman, L. M., Raleigh, M. S., & Lundquist, J. D. (2015). Impact of errors in the downwelling irradiances on simulations of snow water equivalent, snow surface temperature, and the snow energy balance. *Water Resources Research*, *51*(3), 1649–1670. https://doi.org/10.1002/2014WR016259

Li, X., & Wang, J. (1999). The definition of effective emissivity of land surface at the scale of remote sensing pixels. *Chinese Science Bulletin*, *44*(23), 2154–2158. https://doi.org/10.1007/BF03182699

Liu, H., & Weng, Q. (2008). Seasonal variations in the relationship between landscape pattern and land surface temperature in Indianapolis, USA. *Environmental Monitoring and Assessment*, *144*(1–3), 199–219. https://doi.org/10.1007/s10661-007-9979-5

Liu, Y., Hiyama, T., & Yamaguchi, Y. (2006). Scaling of land surface temperature using satellite data: A case examination on ASTER and MODIS products over a heterogeneous terrain area. *Remote Sensing of Environment*, *105*(2), 115–128. https://doi.org/10.1016/j.rse.2006.06.012

Lord, S. (1992). *Earth atmosphere transmittance measurements*. Technical report, NASA Technical Memorandum 103957,, www. gemini. edu ….

Lundquist, J. D., & Cayan, D. R. (2007). Surface temperature patterns in complex terrain: Daily variations and long-term change in the central Sierra Nevada, California. *Journal of Geophysical Research*, *112*(D11), D11124. https://doi.org/10.1029/2006JD007561

Lundquist, J. D., Chickadel, C., Cristea, N., Currier, W. R., Henn, B., Keenan, E., & Dozier, J. (2018). Separating snow and forest temperatures with thermal infrared remote sensing. *Remote Sensing of Environment*, *209*, 764–779. https://doi.org/10.1016/j.rse.2018.03.001

Maeda, E. E. (2014). Downscaling MODIS LST in the East African mountains using elevation gradient and land-cover information. *International Journal of Remote Sensing*, *35*(9), 3094–3108. https://doi.org/10.1080/01431161.2014.903442

Marsetič, A., Oštir, K., & Fras, M. K. (2015). Automatic Orthorectification of High-Resolution Optical Satellite Images Using Vector Roads. *IEEE Transactions on Geoscience and Remote Sensing*, *53*(11), 6035–6047. https://doi.org/10.1109/TGRS.2015.2431434

Martin, T. A., Hinckley, T. M., Meinzer, F. C., & Sprugel, D. G. (1999). Boundary layer conductance, leaf temperature and transpiration of Abies amabilis branches. *Tree Physiology*, *19*(7), 435–443. https://doi.org/10.1093/treephys/19.7.435

Massey, J. D., Steenburgh, W. J., Knievel, J. C., & Cheng, W. Y. Y. (2016). Regional Soil Moisture Biases and Their Influence on WRF Model Temperature Forecasts over the Intermountain West. *Weather and Forecasting*, *31*(1), 197–216. https://doi.org/10.1175/WAF-D-15-0073.1

McMillin, L. M. (1975). Estimation of sea surface temperatures from two infrared window measurements with different absorption. *Journal of Geophysical Research*, *80*(36), 5113–5117.

Mello, P. A., & Pestana, S. (2022). *spestana/goes-py: V0.2.2* [Computer software]. Zenodo. https://doi.org/10.5281/zenodo.6455060

Meyer, D., Siemonsma, D., Brooks, B., & Johnson, L. (2015). Advanced Spaceborne Thermal Emission and Reflection Radiometer Level 1 Precision Terrain Corrected Registered At-Sensor Radiance (AST_L1T) Product, algorithm theoretical basis document. In *Advanced Spaceborne Thermal Emission and Reflection Radiometer Level 1 Precision Terrain Corrected Registered At-Sensor Radiance (AST_L1T) Product, algorithm theoretical basis document* (USGS Numbered Series 2015–1171; Open-File Report, Vols. 2015–1171, p. 50). U.S. Geological Survey. https://doi.org/10.3133/ofr20151171

Minder, J. R., Mote, P. W., & Lundquist, J. D. (2010). Surface temperature lapse rates over complex terrain: Lessons from the Cascade Mountains. *Journal of Geophysical Research*, *115*(D14), D14122. https://doi.org/10.1029/2009JD013493

Mizukami, N., P. Clark, M., G. Slater, A., D. Brekke, L., M. Elsner, M., R. Arnold, J., & Gangopadhyay, S. (2014). Hydrologic Implications of Different Large-Scale Meteorological Model Forcing Datasets in Mountainous Regions. *Journal of Hydrometeorology*, *15*(1), 474–488. https://doi.org/10.1175/JHM-D-13-036.1

MODIS MCST. (2018). *MODIS 1 km Calibrated Radiances Product*. NASA MODIS Adaptive Processing System, Goddard Space Flight Center Greenbelt ….

NASA SRTM. (2013). *Shuttle Radar Topography Mission (SRTM) Global. Distributed by OpenTopography*. https://portal.opentopography.org/datasetMetadata?otCollectionID=OT.042013.4326.1

Niu, G.-Y., Yang, Z.-L., Mitchell, K. E., Chen, F., Ek, M. B., Barlage, M., Kumar, A., Manning, K., Niyogi, D., Rosero, E., Tewari, M., & Xia, Y. (2011). The community Noah land surface model with multiparameterization options (Noah-MP): 1. Model description and

evaluation with local-scale measurements. *Journal of Geophysical Research*, *116*(D12), D12109. https://doi.org/10.1029/2010JD015139

NOAA. (2019). *GOES-R Product Definition and Users' Guide (PUG) Volume 3: Level 1b Products*. U.S. Department of Commerce (DOC), National Oceanic and Atmospheric Administration (NOAA), NOAA Satellite and Information Service (NESDIS), & National Aeronautics and Space Administration (NASA). https://www.goes-r.gov/users/docs/PUG-L1b-vol3.pdf

NOAA-NASA. (2019). GOES-R Series Data Book. *GOES-R Series Program, May*, 240.

Nolin, A. W. (2010). Recent advances in remote sensing of seasonal snow. *Journal of Glaciology*, *56*(200), 1141–1150. https://doi.org/10.3189/002214311796406077

Otterman, J., Brakke, T. W., Fuchs, M., Lakshmi, V., & Cadeddu, M. (1999). Longwave emission from a plant/soil surface as a function of the view direction: Dependence on the canopy architecture. *International Journal of Remote Sensing*, *20*(11), 2195–2201. https://doi.org/10.1080/014311699212191

Painter, T. H., Rittger, K., McKenzie, C., Slaughter, P., Davis, R. E., & Dozier, J. (2009). Retrieval of subpixel snow covered area, grain size, and albedo from MODIS. *Remote Sensing of Environment*, *113*(4), 868–879. https://doi.org/10.1016/j.rse.2009.01.001

Pavelsky, T. M., Kapnick, S., & Hall, A. (2011). Accumulation and melt dynamics of snowpack from a multiresolution regional climate model in the central Sierra Nevada, California. *Journal of Geophysical Research*, *116*(D16), D16115. https://doi.org/10.1029/2010JD015479

Pepin, N. C., Maeda, E. E., & Williams, R. (2016). Use of remotely sensed land surface temperature as a proxy for air temperatures at high elevations: Findings from a 5000 m elevational transect across Kilimanjaro. *Journal of Geophysical Research: Atmospheres*, *121*(17), 9998. https://doi.org/10.1002/2016JD025497

Pepin, N. C., Pike, G., Read, S., & Williams, R. (2019). The ability of moderate resolution imaging spectroradiometer land surface temperatures to simulate cold air drainage and microclimates in complex Arctic terrain. *International Journal of Climatology*, *39*(2), 953–973. https://doi.org/10.1002/joc.5854

Pestana, S., Bhushan, S., & Carter, J. (2022). *spestana/goes-ortho: Initial release | Zenodo* [Computer software]. https://zenodo.org/record/6455138

Pestana, S., Chickadel, C. C., Harpold, A., Kostadinov, T. S., Pai, H., Tyler, S., Webster, C., & Lundquist, J. D. (2019). Bias Correction of Airborne Thermal Infrared Observations Over Forests Using Melting Snow. *Water Resources Research*, *55*(12), 11331–11343. https://doi.org/10.1029/2019WR025699

Pestana, S., & Lundquist, J. D. (2021). *SnowEx20 Raw Near Surface Snow Temperature Profile Time Series, Version 1*. NASA National Snow and Ice Data Center Distributed Active Archive Center. https://doi.org/10.5067/9HYQMFZP4ALB

Pestana, S., & Lundquist, J. D. (2022). Evaluating GOES-16 ABI surface brightness temperature observation biases over the central Sierra Nevada of California. *Remote Sensing of Environment*, *281*, 113221. https://doi.org/10.1016/j.rse.2022.113221

Quan, J., Zhan, W., Ma, T., Du, Y., Guo, Z., & Qin, B. (2018). An integrated model for generating hourly Landsat-like land surface temperatures over heterogeneous landscapes. *Remote Sensing of Environment*, *206*, 403–423. https://doi.org/10.1016/j.rse.2017.12.003

Raleigh, M. S., Landry, C. C., Hayashi, M., Quinton, W. L., & Lundquist, J. D. (2013). Approximating snow surface temperature from standard temperature and humidity data:

New possibilities for snow model and remote sensing evaluation: Snow Surface Temperature Approximation. *Water Resources Research*, *49*(12), 8053–8069. https://doi.org/10.1002/2013WR013958

Raleigh, M. S., Livneh, B., Lapo, K., & Lundquist, J. D. (2016). How Does Availability of Meteorological Forcing Data Impact Physically Based Snowpack Simulations?*. *Journal of Hydrometeorology*, *17*(1), 99–120. https://doi.org/10.1175/JHM-D-14-0235.1

Rittger, K., Raleigh, M. S., Dozier, J., Hill, A. F., Lutz, J. A., & Painter, T. H. (2019). Canopy Adjustment and Improved Cloud Detection for Remotely Sensed Snow Cover Mapping. In *Water Resources Research*. https://doi.org/10.1029/2019wr024914

Salisbury, J. W., & D´Aria, D. M. (1992). Emissivity of Terrestrial Materials in the 8-14 micron Atmospheric Window. *Remote Sensing of Environment*, *42*, 83–106.

Schmit, T. J., Griffith, P., Gunshor, M. M., Daniels, J. M., Goodman, S. J., & Lebair, W. J. (2017). A Closer Look at the ABI on the GOES-R Series. *Bulletin of the American Meteorological Society*, *98*(4), 681–698. https://doi.org/10.1175/BAMS-D-15-00230.1

Schmit, T. J., Lindstrom, S. S., Gerth, J. J., & Gunshor, M. M. (2018). Applications of the 16 spectral bands on the Advanced Baseline Imager (ABI). *Journal of Operational Meteorology*, *06*(04), 33–46. https://doi.org/10.15191/nwajom.2018.0604

Selkowitz, D., Forster, R., & Caldwell, M. (2014). Prevalence of Pure Versus Mixed Snow Cover Pixels across Spatial Resolutions in Alpine Environments. *Remote Sensing*, *6*(12), 12478–12508. https://doi.org/10.3390/rs61212478

Shamir, E., & Georgakakos, K. P. (2014). MODIS Land Surface Temperature as an index of surface air temperature for operational snowpack estimation. *Remote Sensing of Environment*, *152*, 83–98. https://doi.org/10.1016/j.rse.2014.06.001

Siirila-Woodburn, E. R., Rhoades, A. M., Hatchett, B. J., Huning, L. S., Szinai, J., Tague, C., Nico, P. S., Feldman, D. R., Jones, A. D., Collins, W. D., & Kaatz, L. (2021). A low-to-no snow future and its impacts on water resources in the western United States. *Nature Reviews Earth & Environment*, *2*(11), Article 11. https://doi.org/10.1038/s43017-021-00219-y

Stafford, B. (2021). *Pysolar* (0.10) [Computer software]. https://pysolar.org/

Stillinger, T., Roberts, D. A., Collar, N. M., & Dozier, J. (2019). Cloud Masking for Landsat 8 and MODIS Terra Over Snow-Covered Terrain: Error Analysis and Spectral Similarity Between Snow and Cloud. *Water Resources Research*, *55*(7), 6169–6184. https://doi.org/10.1029/2019WR024932

Sun, D., & Pinker, R. T. (2003). Estimation of land surface temperature from a Geostationary Operational Environmental Satellite (GOES-8). *Journal of Geophysical Research*, *108*(D11), 4326. https://doi.org/10.1029/2002JD002422

Takeuchi, W. (2016). Assessment of geometric errors of Advanced Himawari-8 Imager (AHI) over one year operation. *IOP Conference Series: Earth and Environmental Science*, *37*, 012004. https://doi.org/10.1088/1755-1315/37/1/012004

Takeuchi, W., & Yasuoka, Y. (2007). Precise geometric correction of MTSAT imagery. *Proceedings of the ACRS*.

Tan, B., Dellomo, J., Wolfe, R. E., & Reth, A. D. (2018). GOES-16 ABI navigation assessment. In J. J. Butler, X. (Jack) Xiong, & X. Gu (Eds.), *Earth Observing Systems XXIII* (p. 15). SPIE. https://doi.org/10.1117/12.2321170

Thome, K. J. (1999). *MODIS Level 1 At-Sensor Radiance*.

Tomasi, E., Giovannini, L., Zardi, D., & de Franceschi, M. (2017). Optimization of Noah and Noah_MP WRF Land Surface Schemes in Snow-Melting Conditions over Complex Terrain. *Monthly Weather Review*, *145*(12), 4727–4745. https://doi.org/10.1175/MWR-D-16-0408.1

US Geologic Survey. (2017). *1 Arc-second Digital Elevation Models (DEMs)–USGS National Map 3DEP Downloadable Data Collection.* United States Geologic Survey, United States Department of the Interior ….

USDA Forest Service. (2019). *National Land Cover Database (NLCD) 2016 Tree Canopy Cover (CONUS)*. Multi-Resolution Land Characteristics (MRLC) Consortium. https://www.mrlc.gov/data/nlcd-2016-usfs-tree-canopy-cover-conus

Vikhamar, D., & Solberg, R. (2003). Subpixel mapping of snow cover in forests by optical remote sensing. *Remote Sensing of Environment*, *84*(1), 69–82. https://doi.org/10.1016/S0034-4257(02)00098-6

Virtanen, P., Gommers, R., Oliphant, T. E., Haberland, M., Reddy, T., Cournapeau, D., Burovski, E., Peterson, P., Weckesser, W., Bright, J., van der Walt, S. J., Brett, M., Wilson, J., Millman, K. J., Mayorov, N., Nelson, A. R. J., Jones, E., Kern, R., Larson, E., … SciPy 1.0 Contributors. (2020). SciPy 1.0: Fundamental Algorithms for Scientific Computing in Python. *Nature Methods*, *17*, 261–272. https://doi.org/10.1038/s41592-019-0686-2

Walters, R. D. (2013). *Transfer of Snow Information across the Macro-to-Hillslope-Scale Gap Using a Physiographic Downscaling Approach: Implications for Hydrologic Modeling in Semiarid, Seasonally Snow-Dominated Watersheds*. *May*.

Wan, Z. (1999). MODIS land-surface temperature algorithm theoretical basis document (LST ATBD). *Institute for Computational Earth System Science, Santa Barbara*, *75*, 18.

Wan, Z. M., & Zhang, Y. (1999). *MODIS UCSB Emissivity Library* [dataset]. https://icess.eri.ucsb.edu/modis/EMIS/html/em.html

Wan, Z., Zhang, Y., Zhang, Q., & Li, Z. (2002). Validation of the land-surface temperature products retrieved from Terra Moderate Resolution Imaging Spectroradiometer data. *Remote Sensing of Environment*, *83*(1), 163–180. https://doi.org/10.1016/S0034-4257(02)00093-7

Wang, W., Li, S., Hashimoto, H., Takenaka, H., Higuchi, A., Kalluri, S., & Nemani, R. (2020). An Introduction to the Geostationary-NASA Earth Exchange (GeoNEX) Products: 1. Top-of-Atmosphere Reflectance and Brightness Temperature. *Remote Sensing*, *12*(8), 1267. https://doi.org/10.3390/rs12081267

Warren, S. G. (1982). Optical properties of snow. *Reviews of Geophysics*, *20*(1), 67–89. https://doi.org/10.1029/RG020i001p00067

Warren, S. G. (2019). Optical properties of ice and snow. *Philosophical Transactions of the Royal Society A: Mathematical, Physical and Engineering Sciences*, *377*(2146), 20180161. https://doi.org/10.1098/rsta.2018.0161

Warren, S. G., Brandt, R. E., & O'Rawe Hinton, P. (1998). Effect of surface roughness on bidirectional reflectance of Antarctic snow. *Journal of Geophysical Research: Planets*, *103*(E11), 25789–25807. https://doi.org/10.1029/98JE01898

Weaver, J. F., Lindsey, D., Bikos, D., Schmidt, C. C., & Prins, E. (2004). Fire Detection Using GOES Rapid Scan Imagery. *Weather and Forecasting*, *19*(3), 496–510. https://doi.org/10.1175/1520-0434(2004)019<0496:FDUGRS>2.0.CO;2

Webster, C., Rutter, N., & Jonas, T. (2017). Improving representation of canopy temperatures for modeling subcanopy incoming longwave radiation to the snow surface. *Journal of Geophysical Research: Atmospheres*, *122*(17), 9154–9172. https://doi.org/10.1002/2017JD026581

Weng, Q., & Fu, P. (2014). Modeling diurnal land temperature cycles over Los Angeles using downscaled GOES imagery. *ISPRS Journal of Photogrammetry and Remote Sensing*, *97*, 78–88. https://doi.org/10.1016/j.isprsjprs.2014.08.009

Williamson, S. N., Hik, D. S., Gamon, J. A., Jarosch, A. H., Anslow, F. S., Clarke, G. K. C., & Scott Rupp, T. (2017). Spring and summer monthly MODIS LST is inherently biased compared to air temperature in snow covered sub-Arctic mountains. *Remote Sensing of Environment*, *189*, 14–24. https://doi.org/10.1016/j.rse.2016.11.009

Williamson, S. N., Hik, D. S., Gamon, J. A., Kavanaugh, J. L., & Koh, S. (2013). Evaluating Cloud Contamination in Clear-Sky MODIS Terra Daytime Land Surface Temperatures Using Ground-Based Meteorology Station Observations. *Journal of Climate*, *26*(5), 1551–1560. https://doi.org/10.1175/JCLI-D-12-00250.1

Wu, P., Shen, H., Zhang, L., & Göttsche, F.-M. (2015). Integrated fusion of multi-scale polar-orbiting and geostationary satellite observations for the mapping of high spatial and temporal resolution land surface temperature. *Remote Sensing of Environment*, *156*, 169–181. https://doi.org/10.1016/j.rse.2014.09.013

Wylie, D. P., Santek, D., & Starr, D. O. (1998). Cloud-Top Heights from GOES-8 and GOES-9 Stereoscopic Imagery. *Journal of Applied Meteorology*, *37*(4), 405–413. https://doi.org/10.1175/1520-0450(1998)037<0405:CTHFGA>2.0.CO;2

Xiang, T., Vivoni, E. R., Gochis, D. J., & Mascaro, G. (2017). On the diurnal cycle of surface energy fluxes in the North American monsoon region using the WRF-Hydro modeling system. *Journal of Geophysical Research: Atmospheres*, *122*(17), 9024–9049. https://doi.org/10.1002/2017JD026472

Xin, Q., Woodcock, C. E., Liu, J., Tan, B., Melloh, R. A., & Davis, R. E. (2012). View angle effects on MODIS snow mapping in forests. *Remote Sensing of Environment*, *118*, 50–59. https://doi.org/10.1016/j.rse.2011.10.029

Young, T. (2021). *GOES-R Stereoscopic Cloud Top Retrieval Algorithm Using Normalized Cross-Correlation for 1-min Overshoot Analysis.* 6.

Yu, Y., Tarpley, D., Hui, X., & Chen, M. (2010). *GOES-R Advanced Baseline Imager (ABI) Algorithm Theoretical Basis Document For Land Surface Temperature*. *September*, 1–60.

Yu, Y., Tarpley, D., Privette, J. L., Goldberg, M. D., Raja, M. R. V., Vinnikov, K. Y., & Xu, H. (2008). Developing algorithm for operational GOES-R land surface temperature product. *IEEE Transactions on Geoscience and Remote Sensing*, *47*(3), 936–951.

Zink, M., Mai, J., Cuntz, M., & Samaniego, L. (2018). Conditioning a Hydrologic Model Using Patterns of Remotely Sensed Land Surface Temperature. *Water Resources Research*, *54*(4), 2976–2998. https://doi.org/10.1002/2017WR021346